POROSITY AND MOISTURE EFFECTS ON DYNAMIC STRENGTH OF TWO SANDSTONES FROM UTAH

by

Hossein Changani

A thesis submitted to the faculty of
The University of Utah
in partial fulfillment of the requirements for the degree of

Master of Science

Department of Mining Engineering

The University of Utah

August 2015

The University of Utah Graduate School

STATEMENT OF THESIS APPROVAL

The following faculty members served as the supervisory committee chair and members for the thesis of Hossein Changani.

Dates at right indicate the members' approval of the thesis.

Eunhye Kim, Chair	May,1st, 2015 Date Approved
Michael K. McCarter, Member	May,1st, 2015 Date Approved
Brian McPherson, Member	May,1st, 2015 Date Approved

The thesis has also been approved by Michael G Nelson Chair of the Department/School/College of Mining Engineering and by David B. Kieda, Dean of The Graduate School.

ABSTRACT

The dynamic strength properties of rock have a critical application in blasting, fragmentation, designing underground structures, and perforating oil and gas wells. This research focused on two types of sandstone from Utah with two different ranges of porosity and the effect of porosity and water content on dynamic compressive and tensile strength under dynamic loading conditions. The Split Hopkinson Pressure Bar (SHPB) apparatus was used for measuring the compressive and tensile strength of these rocks.

The dynamic compressive strength, measured under a strain rate of about 350/s, was found to be 1.4 to 2.0 times the compressive strength measured under static conditions for samples of similar dimensions in both dry and saturated conditions for "red" and "buff" sandstones. Based on these results, this research found that rock specimens with higher porosity had a higher dynamic increase factor (DIF). In addition, water reduced the cohesion of saturated rock by approximately 20%, and saturation reduced the dynamic compressive and tensile strength by approximately 20%. However, fragment sizes of saturated samples are finer than those of dry samples. The saturated samples also absorbed approximately 15% less energy.

For my Loves

Saeideh & Samin

TABLE OF CONTENTS

LIST OF FIGURES

LIST OF TABLES

CHAPTER 1

INTRODUCTION AND OBJECTIVE

1.1 General overview

Dynamic characterization of rocks assumes great importance in different applications. In mine to mill operations (including drilling, blasting, crushing, and grinding) or in overall fragmentation processes, the rate of loading has a significant effect on the process of rock breakage in both dry and fully saturated conditions (Atchison and Pugliese 1964). Therefore, information about loading rate and dynamic behavior of rock under varied conditions may significantly affect managing energy cost in mine to mill operations. In the oil and gas industry, the main task of reservoir engineers is to increase the productivity of wells. For this issue, induced hydraulic fracturing, or hydrofracturing, is a technique that is typically used to generate fractures in the rock reservoir. In the beginning of this process, a device known as a perforating gun is lowered into the well to a designated location in the reservoir rock, and a charge is fired to perforate the steel casing, cement, and the rock formation. This perforation stage creates small cracks or fractures in the rock, and then a mixture of water, sand, and chemicals is injected into the wellbore under high pressure to keep the fractures open. In all steps of this process, having knowledge about the effect of porosity and water content on dynamic behavior of

reservoir rock may be useful in predicting the rock behavior.

The Split Hopkinson Pressure Bar (SHPB) technique is extensively used to characterize material behavior at high strain rates near those achieved in blasting. In this research, dynamic laboratory measurements using compressive and tensional Hopkinson bar techniques were used to identify the effect of strain rate on rock breakage.

1.2 Research objective

A number of parameters influence the static and dynamic behavior of rocks. The fracture behavior of rock, especially with different porosity and water content under dynamic loading conditions, is a key parameter in understanding the rock characteristics in mining and fracking processes (Atchison and Pugliese 1964). Parker (1969) worked on the effect of environmental factors (such as moisture) on the strength of sandstone pillars, and concluded that water absorption by rocks reduces pillar strength. McCarter (1972) studied numerous clastic sedimentary rocks, and concluded that water content results in a significant reduction in compressive and tensile strength of some clastic sedimentary rocks. While much work on the effect of porosity on dynamic fracture mechanics has been done for metals, composites, and ceramics (Igbal et al. 2011), only a very limited amount of work has been done on man-made rocks with different porosities under dynamic loading conditions (Yong et al. 2011; Hua et al. 2013). The present research aims to fill in some of these gaps in knowledge about porosity and water content effects on the dynamic strength of rocks. The common rock properties applicable to these research processes were measured in the laboratory, and the results compare dry and saturated conditions for two types of sandstone. Specifically, the present study aimed to:

a) Measure physical and mechanical properties such as density, porosity, compressive and tensile strengths, and seismic wave velocity (P and S waves);
b) Measure dynamic compressive and tensile strength at strain rates up to 350/s using the SHPB apparatus;
c) Calculate the energy absorption by samples during dynamic tests;
d) Measure rock fragment size distribution of dry and saturated rock specimens;
e) Analyze the strain rate (loading rate) effects on rock specimen strength.

To achieve the research objectives mentioned above, 179 samples of two types of Utah sandstone were tested in static, intermediate loading (fast loading), and dynamic conditions. Results reported here include 40 NX cylindrical samples on which the unconfined compressive strengths were measured, 77 AX cylindrical samples on which dynamic, static and fast loading compressive strengths were determined, and 62 disc samples used for static and dynamic tension tests. Details are listed in tables in the relevant sections of this thesis.

1.3 Thesis organization

This thesis gives an overview of dynamic characterization of rocks under high strain rate loading. The overview begins in Chapter 2 where a comprehensive literature review of the SHPB test subjects is presented. This chapter explains various aspects of the Hopkinson apparatus including development, theoretical concept, experimental setup, and sample size selection. Chapter 3 discusses the physical properties of the selected rock types. These properties include density, porosity, ultrasonic velocity, uniaxial compressive strength, tensile strength, and triaxial tests. All of these tests were done

under dry and saturated conditions. The various aspects of dynamic tests with SHPB are discussed in Chapter 4, and this chapter also presents the results and the analysis of compressive and tensile strengths of the two types of sandstone with respect to water content and porosity. The parametric variation includes the effects of porosity and water content on dynamic strength and loading rate. The conclusions of the experimental investigations are presented in Chapter 5.

CHAPTER 2

LITERATURE REVIEW

2.1 Split Hopkinson Pressure Bar machine (SHPB)

This literature review will first explain the historical development of the Hopkinson apparatus, its theoretical background, the experimental setup, and the sample size selection.

The dynamic properties of rock are of great importance in the design of both surface and underground structure to ensure they can resist loads under dynamic conditions (Bulson 2002). The dynamic strength of rock also plays an important role in overall mine to mill cost optimization (Atchison and Pugliese 1964). For measuring the dynamic behavior of materials based on loading rate, various techniques exist. Field et al. (2004) reviewed experimental techniques for the characterization of dynamic properties of materials and presented a schematic diagram for the range of strain rates. Table 2.1 presents conventional static testing methods, which covers the low range of strain rates up to 10 s^{-1}. Field et al. (2004) used instruments such as drop-weight, SHPBs, and plate impact in the high strain rate range of 10-10^7 s^{-1} for measuring dynamic properties of materials.

The SHPB method was not widely used until the 1970s when it quickly became the standard method of measuring dynamic properties of materials. This technique has

mostly been used to study the dynamic response of solid materials undergoing large strain rates between 10 s^{-1} and 10^4 s^{-1} in compression, tension, and torsion tests. The SHPB apparatus was originally introduced by Bertram Hopkinson in 1913 and later developed by Kolsky (1949). The technique that was introduced by Hopkinson (1914) was used to determine the stress–time relation of an impact produced by a bullet. Many researchers have used the SHPB apparatus for measuring the dynamic properties of different materials. This machine (Figure 2.1) consists of (A) a means to develop impact-like pressures, (B) a long steel rod, (C) a short steel sample, and (D) a ballistic pendulum. Hopkinson's idea was to impact one end of the rod, and let the compressive wave propagate through the bar and the greased joint, and into the sample. The wave would then be reflected at the end as a tension pulse. Because of the reflected tensile wave, the sample flies off with a definite momentum that is measured with a momentum trap. The time over which this momentum acts is the round trip time of the longitudinal wave in the sample. This wave is generated by stress, and a stress-time curve can describe the impact event (Hopkinson 1914).

In 1941, Dennison Bancroft solved the frequency equation for the velocity of longitudinal waves in cylindrical bars in terms of Poisson's ratio, the ratio of bar diameter to the wavelength, and a wave of infinite wavelength. The use of high-speed computers for data processing has allowed researchers to apply this equation with Hopkinson bar testing (Bancroft 1941).

In 1948, Davies developed a technique using condensers to measure strains in the pressure bar. This technique greatly improved the accuracy of Hopkinson's original apparatus, which relied on measuring the momentum of a steel sample flying off the end

of the pressure bar (Davies 1948).

In 1949, Kolsky added a second pressure bar to Hopkinson's original apparatus, called a transmitted bar. He sandwiched a specimen between the two bars and presented expressions for calculating specimen properties based on strain histories in the bars. The strains were measured using similar condensers as those used by Davies. This two bar technique, the SHPB, has become the most widely used testing procedure today. In some literature it is referred to as the Kolsky bar (Kolsky 1949).

Over the next several years, many improvements were made on the SHPB. Harding et al. (1960) designed the SHPB machine for measuring the tensile strength of materials at high strain rates. This technique has the advantage of reducing the effect of friction between the bars and the sample, which improves the accuracy of test results (Harding 1960). Years later, Hauser et al. (1961) used strain gauges on the Split Hopkinson Bar to measure surface displacements (Hauser et al. 1961). Duffy et al. (1971) developed the torsion version of SHPB that nearly always loaded statically instead of dynamically (Duffy 1971). Table 2.2 summarizes development of this technique after the 1970s.

Goldsmith et al. (1976) studied the compressive and tensile dynamic behavior of Barre Granite by using the SHPB and showed that compressive and tensile strengths of this rock are related to loading rate. Based on his study, he found the compressive strength of this rock at strain rate levels of 10^3/s increased, and it was two times larger than the static strength (Goldsmith 1976). Gomez et al. 2001 also studied the behavior of Barre Granite and concrete using a 55mm diameter SHPB at a strain rate of 400/s. The dynamic strengths of concrete and granite were reported to be about twice that of the

static strengths, and it was concluded that the energy of impact stores faster than the connection and propagation of cracks that cause specimen failure (Gomez et al. 2001).

Zhao et al. (1999) evaluated the effects of underground blasting on two adjacent caverns developed for ammunition storage. They conducted compressive SHPB tests on Bukit Timah Granite in the strain rate range of 46-874/s. They concluded that the Young's modulus and strength of this granite increases with a higher strain rate, but for strain rates greater than 335/s, the modulus decreases (Zhao et al. 1999). Kim and McCarter (1998) measured the dynamic response of rock during the comminution process under a blasting shock load and carried out many experiments on quartz monzonite, diopside, wollastonite, and subarkosic siltstone by using the SHPB. In their research, the effect of shock-induced damage was analyzed by measuring the ultrasonic wave velocity in pre- and postshock samples. Confocal image analysis was used to obtain crack density (Kim and McCarter 1998). Mohanty and Prasad (2001) measured the fragment size distribution and the dynamic increase factor (DIF) of rock by experimenting on 12 rock types in the strain rate range of 600–1000/s. They concluded that the dynamic increase factor (DIF) in compressive strength of the samples tested was between 2.5 and 4.6 times the static value. Dynamic tensile and compression tests by SHPB were also carried out by Cai et al. (2007) on Haute-Marne Argillite samples that were prepared parallel and perpendicular to the bedding. The experimental results showed the dynamic strength of this rock was strain-rate dependent, and the average dynamic increase factors for tensile and compressive strength measurements were approximately 2.4 and 3.3, respectively (Cai et al. 2007).

Recently the application of lightweight structures and their capacity for absorbing

shock waves has become popular in automotive and aerospace industries. In this area, experiments have been conducted on metallic foam and composite materials. The results show that increasing the porosity in these materials causes a decrease in dynamic strength (Igbal et al. 2011). For rock materials, choosing different porosities for the same rock type is very difficult. For this reason, Dong et al. 2011 used fabricated rock to evaluate the effect of porosity on the dynamic response of rock using the SHPB. In their experiment, the artificial rock was made of white corundum and aluminum phosphate, consolidated at high temperature. The results of three different fabricated rocks with 18%, 25%, and 35% porosity show that increasing the porosity in this type of material decreases the rock strength (Dong et al. 2011). Lu et al. (2013) also conducted experiments using the SHPB on China's red sandstone with porosities of 5.8%, 6.5%, 7.1% and 10.6%. They concluded that increasing porosity reduced the dynamic strength of these rocks.

As mentioned before, this research evaluated the effect of porosity and water content on the dynamic behavior of two Utah sandstones. The results are intended to inform further research on rock fragmentation during the blasting and perforating processes in oil and gas well. For this purpose, the porosity and water content of the buff and red sandstones were measured, and the dynamic response in compression and tension were evaluated by SHPB.

2.2 Theoretical background

The theory behind the SHPB is based on one-dimensional stress wave propagation in a bar. In this theory, Kolsky maintains that when an elastic bar is loaded

axially, stress (σ) along the length of the bar is increased by $\partial\sigma/\partial x$, and by looking at a very small slice of this bar, *dx*, the equilibrium equation based on Newton's second law can be written as shown in Equations 2.1 and 2.2 (Kolsky 1949):

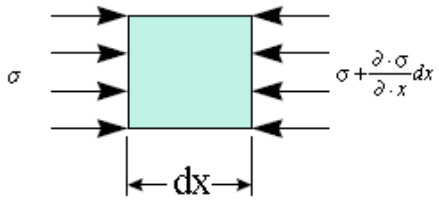

$$-\sigma + \sigma + \frac{\partial \sigma}{\partial x} dx = \rho . dx \frac{\partial^2 u}{\partial t^2} \tag{2.1}$$

$$\frac{\partial \sigma}{\partial x} = \rho \frac{\partial^2 u}{\partial t^2} \tag{2.2}$$

where *u* is displacement in the x-direction, *t* is time, and ρ is the bar density. Based on the linear relation between stress (σ) and strain in elastic material (the bar), the Young's modulus (E) simplifies to Equation 2.3.

$$E = \frac{\sigma}{\varepsilon} \tag{2.3}$$

$$\varepsilon = \frac{\partial u}{\partial x} \tag{2.4}$$

By substituting Equation 2.4 into Equation 2.3:

$$\sigma = E \frac{\partial u}{\partial x} \tag{2.5}$$

Differentiating this equation with respect to *x*:

$$\frac{\partial \sigma}{\partial x} = E \frac{\partial^2 u}{\partial x^2} \tag{2.6}$$

Substituting this equation into Equation 2.2 yields,

$$\frac{\partial^2 u}{\partial t^2} = \frac{E}{\rho} \frac{\partial \sigma}{\partial x} \tag{2.7}$$

This equation is the one-dimensional wave equation that can be used to analyze one-dimensional motions of elastic materials. The velocity of the longitudinal stress wave

in the bar, $= \sqrt{E/\rho}$, can be substituted into Equation 2.7 and rewritten again.

$$\frac{\partial^2 u}{\partial t^2} = C^2 \frac{\partial \sigma}{\partial x} \tag{2.8}$$

Based on one-dimensional wave theory, the SHPB analysis for calculating the dynamic stress-strain behavior of the sample is valid if the following assumptions are satisfied:

a) Bar deformation remains elastic during the tests, and both interfaces between the bars and the sample remain flat and parallel during the sample deformation.
b) The sample reaches a uniform uniaxial state of stress before failure.
c) The stress waves, as they travel along the length of the bars, should have minimal dispersion.
d) Frictional and radial inertial effects on the sample can be neglected.
e) The sample receives only one incident stress wave that causes an observed deformation (Kolsky 1949).

According to this theory and the recorded strain history in the incident bar (ε_I, ε_R) and the transmitted bar (ε_T), stress on the sample's interfaces are:

$$\sigma_1(t) = \frac{EA}{A_S}[\varepsilon_I(t) + \varepsilon_R(t)] \tag{2.9}$$

$$\sigma_2(t) = \frac{EA}{A_S}\varepsilon_T(t) \tag{2.10}$$

The strain rate $\dot{\varepsilon}(t)$, strain $\varepsilon(t)$, and average sample stress $\sigma(t)$ can be calculated by equations 2.11, 2.12, and 2.13, respectively.

$$\dot{\varepsilon}_S(t) = \frac{C}{L_S}[\varepsilon_I(t) - \varepsilon_R(t) - \varepsilon_T(t)] \tag{2.11}$$

$$\varepsilon_s(t) = \frac{C}{L_s}\int_0^t [\varepsilon_I(t) - \varepsilon_R(t) - \varepsilon_T(t)]dt \tag{2.12}$$

$$\sigma_s(t) = \frac{EA}{2A_S}[\varepsilon_I(t) + \varepsilon_R(t) + \varepsilon_T(t)] \tag{2.13}$$

where A is the cross sectional area of the bars, A_s and L_s are the cross sectional areas and length of the sample, C is the longitudinal wave velocity in the bars, $\sigma_1(t)$ and $\sigma_2(t)$ are stresses in incident bar-sample and sample-transmitted bar interfaces (Kolsky 1949). Assuming the stress equilibrium condition happens when $\varepsilon_I(t) + \varepsilon_R(t) = \varepsilon_T(t)$, then Equations 2.14, 2.15, and 2.16 for calculation of strain rate, strain, and stress of sample are obtained:

$$\dot{\varepsilon}_S(t) = \frac{-2C}{L_S}\varepsilon_R(t) \tag{2.14}$$

$$\varepsilon_s(t) = \frac{-2C}{L_s}\int_0^t \varepsilon_R(t)dt \tag{2.15}$$

$$\sigma_s(t) = \frac{EA}{A_S}\varepsilon_T(t) \tag{2.16}$$

2.3 Experimental setup

A schematic diagram of the SHPB (Figure 2.2) shows how the sample is sandwiched and deformed between two bars. This machine consists of an air gas gun, a striker, an incident bar, a transmitted bar, an energy absorber (stopper), an oscilloscope, a laser gate for recording striker velocity, strain gauges, amplifiers, a data acquisition system, and an AC power supply. The gas gun propels the 10 cm long, 456 g striker bar using a given gas pressure.

The oscilloscope (Nicolet 3091) records the generated striker velocity. By hitting

the incident bar, this striker creates a sinusoid, triangular, or trapezoidal compressive stress pulse (incident pulse, ε_I) in the incident bar. This dynamic load propagates into the incident bar and reaches the incident bar-specimen interface. Because of different impedances between sample and bar, part of this pulse reflects into the incident bar as a reflected wave (ε_R), and part of the wave transmits into the transmitted bar as a transmitted pulse (ε_T). These pulses are recorded by a pair of strain gauges (EA-06-250TK-10C) mounted at the middle of each bar. After amplification, the data acquisition system (Nicolet Odyssey XE) records the strain pulse at a rate of 10 million samples per second. The data acquisition system can record very low sampling rates (200–200k samples per second) in a slow acquisition rate. At a fast acquisition rate, the recording rate can be up to 10 million samples per second (Figure 2.3).

When the data acquisition machine is triggered by internal or external trigger sources, the slow sampling mode changes to a fast sampling mode automatically (10 million samples per second). A trigger level can be selected to initiate this change (Figure 2.4). One pair of strain gauges triggers the data acquisition system (Figure 2.5). These strain gauges are installed ahead of incident strain gauges (5 cm from the end of the incident strain gauges), and when the incident wave reaches these gauges, the trigger option of the machine is activated. To reduce the magnetic field effects on the stress wave recordings, the strain gauges in the machine connect to amplifiers with two conductive twisted cables that are covered with an aluminum foil shield. The ground conductor wire connects to earth ground. The amplifiers for the stress waves incorporate a Wheatstone half-bridge (Johnson 2010). The half-bridge amplifier is used to compensate for bending strain and to increase the output signal. These amplifiers operated from a 22 VDC supply

and are designed for a gain of about 5. This gain must be balanced before each test. The precision shunt resistor (75.2939 k Ω of tolerance ± 0.025%) is used for balancing and calibrating the amplifier. Each amplifier has two small screws that are used for adjusting the gain. First, the voltmeter should show zero voltage for each amplifier output. If the voltmeter does not show zero, the left screw is used and the output voltage should be adjusted to zero and recorded as V_{before} (Figure 2.6). The shunt resistor should then be connected to one pair of strain gauges, and the change in output voltage recorded as V_{after}. Equation 2.17 is used for calculating the gain of each amplifier:

$$G = \frac{V_{after} - V_{before}}{71.9} \tag{2.17}$$

where, G, V_{after}, V_{before} are gain, voltage after and before shunting, respectively.

The amplifiers are connected to the data acquisition system by a BNC (Bayonet Neill–Concelman) cable. The output of the three amplifiers includes incident, reflected, and transmitted waves. The data acquisition system uses Odyssey software.

In this SHPB apparatus, the ends of the samples are coated with a thin layer of grease and placed between two steel bars with a 3.175 cm diameter and a 1.295 m length to minimize friction effects at interfaces. The material of these bars is designed to remain elastic during the tests. The measured static Young's modulus (E), bulk density (ρ) and wave velocity of the bars (C) are 189.3 GPa, 7.813 g/cm^3,and 4992 m/s, respectively (Kim 1993).

2.4 Sample size effects

The choice of a proper sample size is a challenging issue among researchers who are involved with SHPB experiments. The L/D ratio of samples (length/diameter) has

major influences on axial and lateral inertial effects. In small L/D ratios, the radial inertia affects the experimental results. In higher L/D ratios, the axial inertia affects the results. Because of these problems, there have been many studies in this field to determine the best sample size. Davies and Hunter (1963) tested metal specimens including copper, aluminum, zinc, magnesium, and brass with a 1.27 cm diameter SHPB. To neglect radial friction effects at specimen-bar interfaces in these experiments, the specimen L/D ratio was selected to be at least one. Comparing the dynamic stress-strain curves with corresponding static curves showed there were strain rate effects on the behavior of these metals, which raised the stress level from 1.0 to 3.0 (Davies and Hunter 1963). Maiden and Green (1966) investigated the compressive strain rate on six different materials by using a 0.9525 cm SHPB apparatus (Maiden and Green, 1966). Their results showed that four of these materials were strain rate sensitive, and increasing the strain rate caused an increase in the stress (6AL-4V titanium, pyrolytic graphite, lucite, and micarta). Two alloys (Al 6061-T6 and Al 7075-T6) showed nonsensitive strain-rate behavior, which is different from the findings of Hauser et al. (1960). In this case, the specimen dimensions, 0.9525 cm diameter and 1.27 cm length, were larger than the Davies and Hunter's ideal (Gorham et al. 1984).

In very short samples, the specimen-bar interface friction affects the lateral strain flow of samples and results in an apparent increase in the uniaxial compressive. Gorham (1984) performed research for maximizing and measuring the friction effects on stress flow. He prepared very thin specimens with a L/D ratio of 0.1, and by testing these samples, showed the relation between friction, mean applied pressure, p, and intrinsic material yield strength, σ_y, as described by Equation 2.18:

$$p = \left(1 + \frac{\mu a}{3\sqrt{3l_s}}\right)\sigma_y \tag{2.18}$$

where a is sample radius, l_s is specimen length, and μ is a coefficient of friction that is assumed constant over the interfaces. In long samples, the stress-strain along the specimen is not uniform because of axial inertia effects due to finite specimen length. Based on the investigations of Davies and Hunter (1962), this stress variation is about $^1/_2\,\rho_s l^2 \ddot{\varepsilon}$ where ρ_s and l are the sample's density and length and $\ddot{\varepsilon}$ is the strain acceleration. Therefore, this variation depends on specimen material and length, and the delay between the stress-time curves for both sides of the sample should be less than 2% (Davies and Hunter 1962).

Radial inertia effect another parameter that Kolsky indicated causes the actual stress for deforming the specimen to be less than what is measured (Kolsky 1949). Davies and Hunter (1962), however, showed that radial and axial inertia effects can be eliminated during tests if the specimen length (l_s) is equal to $\sqrt{3}\vartheta_s d$ or if the strain rate $\varepsilon(t)$ is held constant during the tests (see Equation 2.19).

$$\sigma(t) = \sigma_m(t) + \rho_s\left(\frac{l_s^2}{6} - \vartheta_s\frac{d^2}{8}\right)\frac{\delta^2\varepsilon(t)}{\delta t^2} \tag{2.19}$$

where, ϑ_s , ρ_s, and d, are Poisson's ratio, specimen density and radius of sample, respectively (Davies and Hunter 1962).

In 2000, Gray believed, in addition to the sample L/D ratio, that the radial and lateral inertia and friction effects could be reduced by minimizing the area mismatch between the sample and bar areas. The specimen diameter, as a rule of thumb, should be at least ten times bigger than the microstructural unit size of metal or coarse-scaled material such as rock or concrete. Therefore, as a compromise between his

recommendation and ASTM E9, Gray suggested $0.5 \leq L/D \leq 1.0$ to minimize frictional and inertial factor effects, and for a given bar diameter, the sample diameter should be about 80% of the bar diameter (Gray 2000, ASTM E9-09, Albertini et al. 1996).

Based on their investigation of aluminum 7075-T6 (the composition and the mechanical properties are shown in Table 2.3), Maiden and Green found that the properties of 7075-T6 are insensitive to different strain rates (Maiden and Green, 1966).

As mentioned in Table 2.4, the effects of L/D ratio and the mismatch areas on sample behavior were observed and evaluated in order to find the best sample size for this research. Different L/D ratios (2.0, 1.5, 1.0, 0.5, and 0.25) and various diameters (3.175, 2.54, 1.59, and 0.95 cm) were selected (Figure 2.7). The dynamic compressive behavior of this alloy was investigated by using SHPB, and the importance of sample size and L/D ratio were compared. As mentioned before, the bar diameters were 3.175 cm. For evaluating the mismatch condition on compressive strength results samples with the same diameter, 80%, 50%, and 30% bars diameters were tested and mismatch area effects on dynamic behavior of these samples were investigated.

As shown in Figure 2.8, samples with diameters of 3.175, 2.54 (Figure 2.8b) and 1.59-cm (Figure 2.8c) follow Maiden and Green's graph (Figure 2.8a), while samples with a higher percent of mismatch (0.95 cm diameter) show completely different behavior (Figure 2.8c). Based on these results, and some restrictions in lab equipment for coring and grinding samples with small diameters and L/D ratios, a diameter of 3.175 cm and L/D ratio of 2.0 were selected for sample size in sample preparation steps.

Table 2.1 Different techniques for obtaining static and dynamic properties of materials

Inertial forces Negligible		Inertial forces important	
Strain rate,s-¹	Common testing methods	Strain rate,s-¹	Common testing methods
10^{0}	**Quasi-static**	10^{7}	**High velocity Impact**
10^{-1}	Hydrualic, servo-hydrualic		-Explosive
10^{-2}	or screw-driven testing machines	10^{6}	-Normal plate Impact
10^{-3}			-Pulsed laser
10^{-4}		10^{5}	-Exploding foil
			-Incline plat Impact
10^{-5}	**Creep and stress relaxation**		**Dynamic-High**
		10^{4}	-Taylor anvil test
10^{-7}	-conventional testing machine		-SHPB
10^{-8}	-Creep tester	10^{3}	-Expanding ring
10^{-9}		10^{2}	**Dynamic-Low**
		10^{1}	-Drop-weight
			-High velocity hydraulic or pneumatic machine
			-Plastometer

Modified from Meyers 1999

Table 2.2 Recent major developments in SHPB testing

Date	Developments
1980	Gorham and Field develop the miniaturized direct impact Hopkinson bar
1985	Albertini develops large SHPB for testing structures and concrete
1991	Nemat-Nasser develops one pulse loading SHPBs (compression, tension and torsion) and soft recovery techniques
1991–1993	Use of torsional SHPB for measurement of dynamic sliding friction and shearing properties of lubricants
1992–2003	Development of polymer SHPB for testing foams
1997–2002	Use of wave separation techniques to extend the effective length of a Hopkinson bar system
1998	Development of magnesium SHPB for soft materials
1998	Development of radiant methods for heating metallic SHPB specimens quickly
1998–2002	Analysis of wave propagation in non-uniform viscoelastic rods performed
1999	Development of one pulse torsion SHPB
2003	Extension of Hopkinson bar capability to intermediate strain rates
2003	Application of speckle metrology to specimen deformation

Modified from Field et al. 2004

Table 2.3 Properties of AL 7075-T6

Component elements properties						
Aluminum, Al		87.1 - 91.4 %	Manganese, Mn		<= 0.30 %	
Chromium, Cr		0.18 - 0.28 %	Silicon, Si		<= 0.40 %	
Copper, Cu		1.2 - 2.0 %	Titanium, Ti		<= 0.20 %	
Iron, Fe		<= 0.50 %	Zinc, Zn		5.1 - 6.1 %	
Magnesium, Mg		2.1 - 2.9 %	Others		<= 0.15 %	
Mechanical properties						
Density (g/cc)	Ultimate Tensile Strength (MPa)	Tensile Yield Strength (MPa)	Modulus of Elasticity (GPa)	Poisson's Ratio	Shear Modulus (GPa)	Shear Strength (MPa)
2.81	572	503	71.7	0.33	26.9	31

Modified from Davies (1948)

Table 2.4 L/D ratio suggestion in literature review

Researchers	Objectives	Sample dimensions	L/D ratio
Davies and Hunter 1963	Removing the inertial effect	thickness = 5.5 mm, radius= 6.2 mm	thickness/radius = $\sqrt{3}\vartheta_s$, L/D ratio = ~ 1
Maiden and Green 1966	Evaluating the strain rate effect	L = 12.7 mm, D = 9.525 mm	L/D ratio = 1.33
Gorham 1984	Measuring the frictional effect	L = 0.5–1 mm, D = 1–2 mm	L/D ratio = 0.5
Gorham 1991	Measuring the inertial stress	L = 0.6 mm, D = 1 mm	L/D ratio = 0.6
ASTM E9-09	Reducing the frictional effects on high-strength material	N/A	L/D ratio = 1.5–2.0
Gray 2000	Minimizing the frictional and inertial effects	L = 3.2, 5.0, 6.35 mm D = 6.35 mm	L/D ratio between 0.5 and 1.0 and mismatched area between bar and sample should be more than 80 %

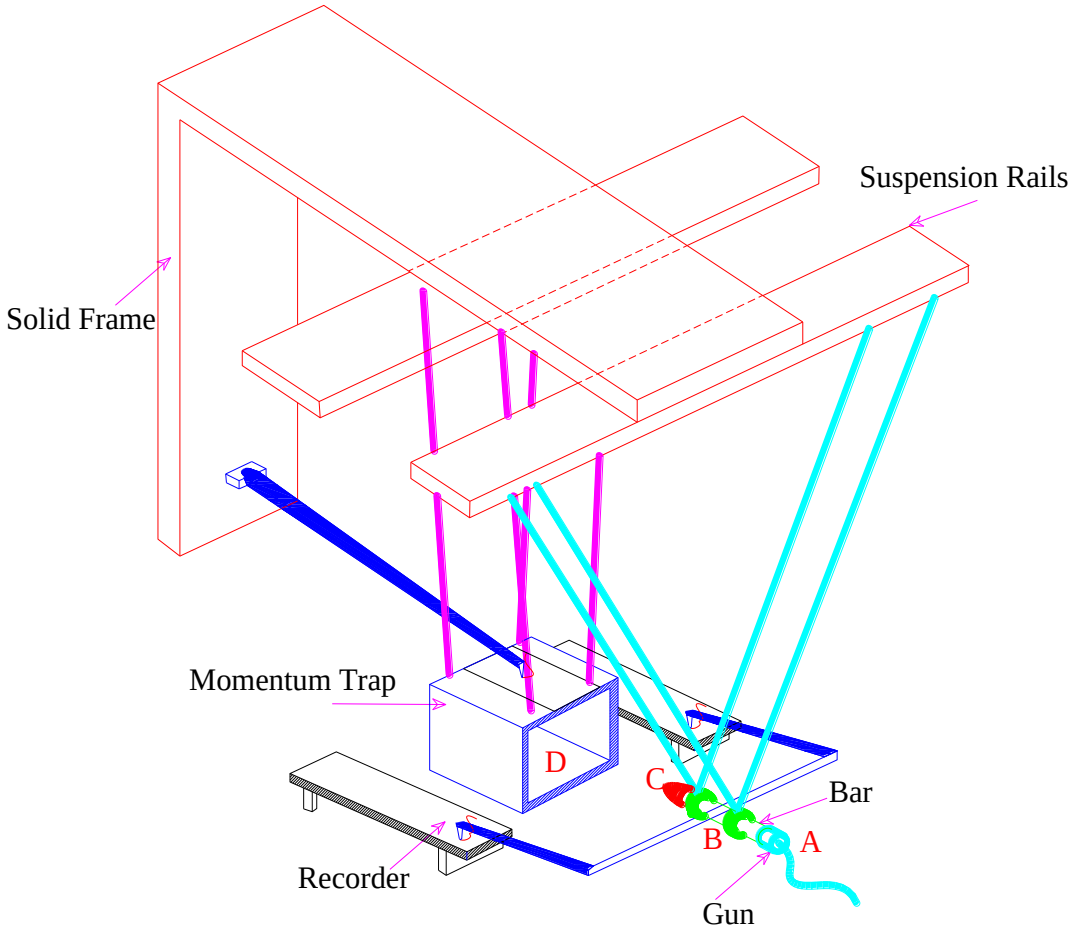

Figure 2.1 General arrangement of Hopkinson's Pressure Bar.

Modified from Hopkinson (1914)

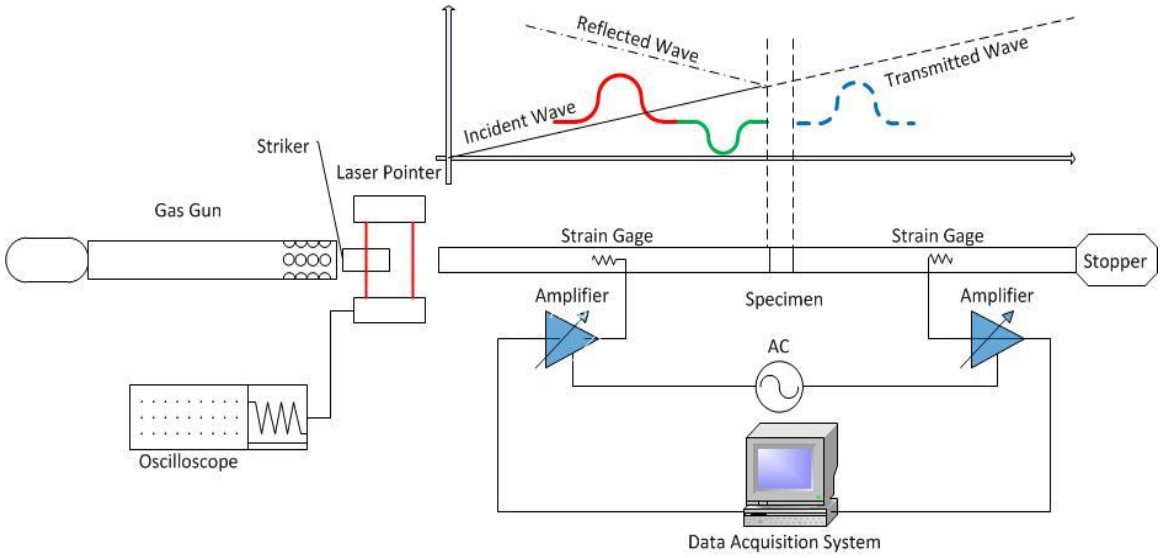

Figure 2.2 Schematic diagram of the SHPB apparatus.

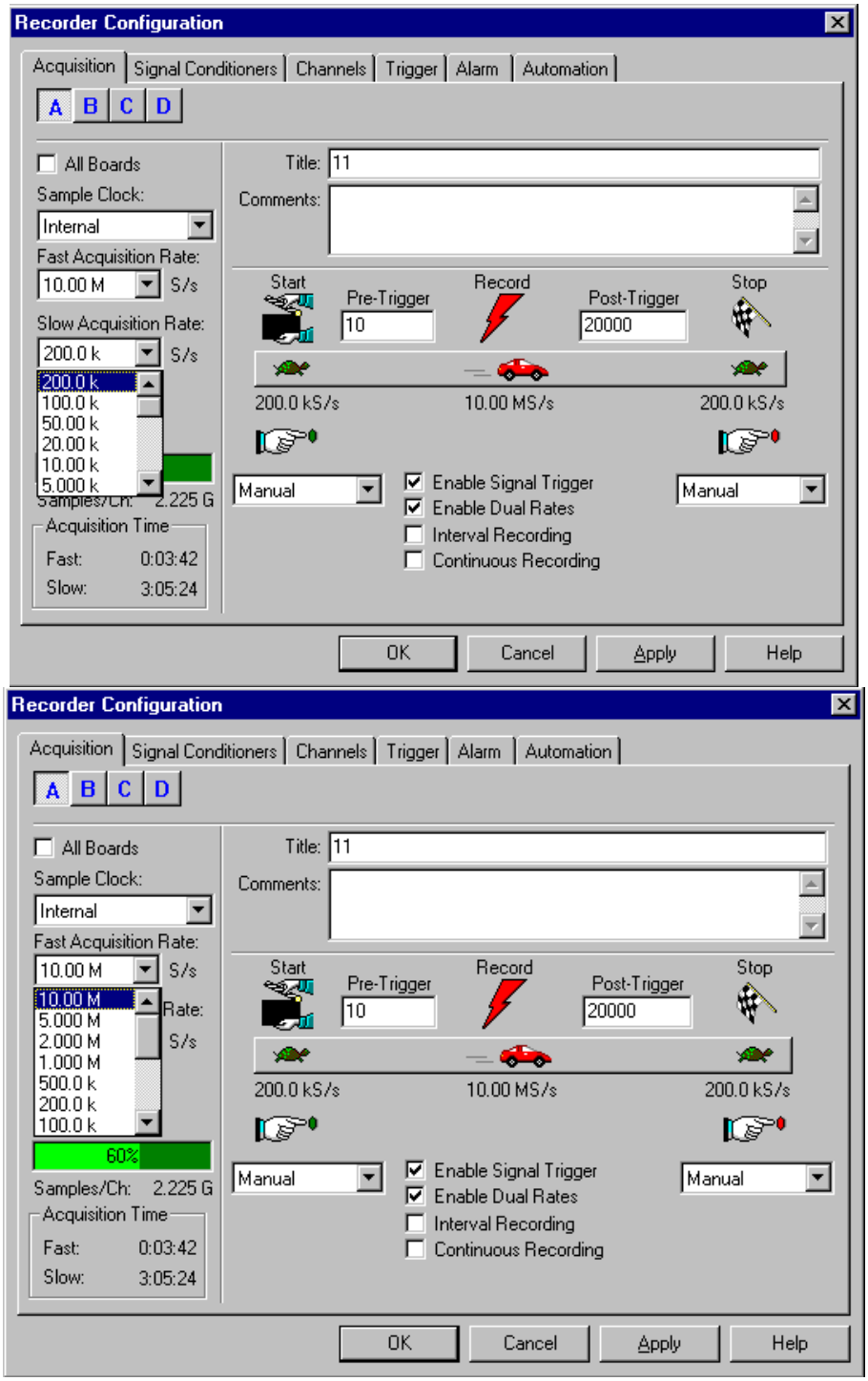

Figure 2.3 Slow and fast acquisition rate of the data acquisition system.

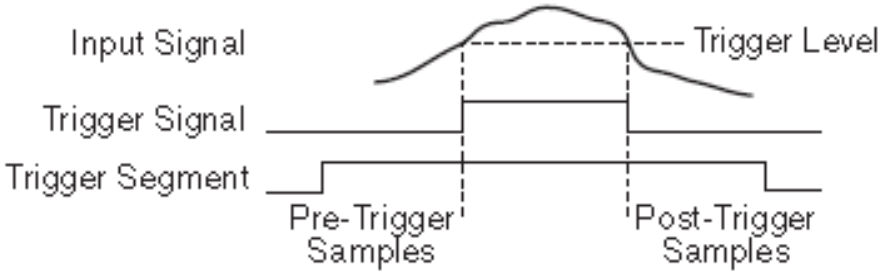

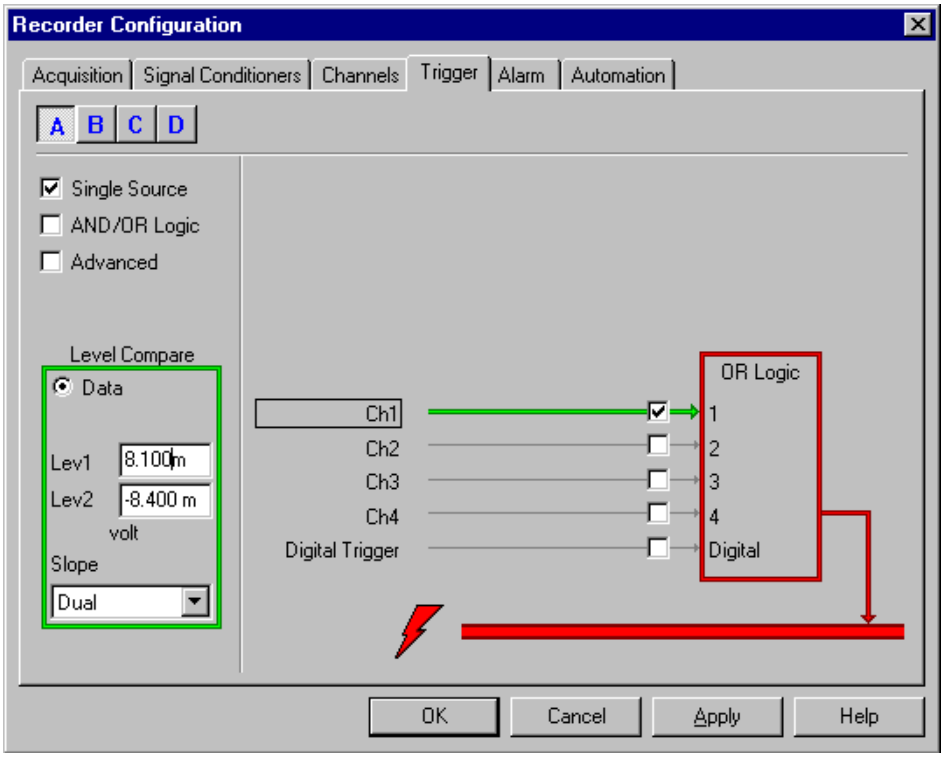

Figure 2.4 Trigger levels and trigger mode in data acquisition system.

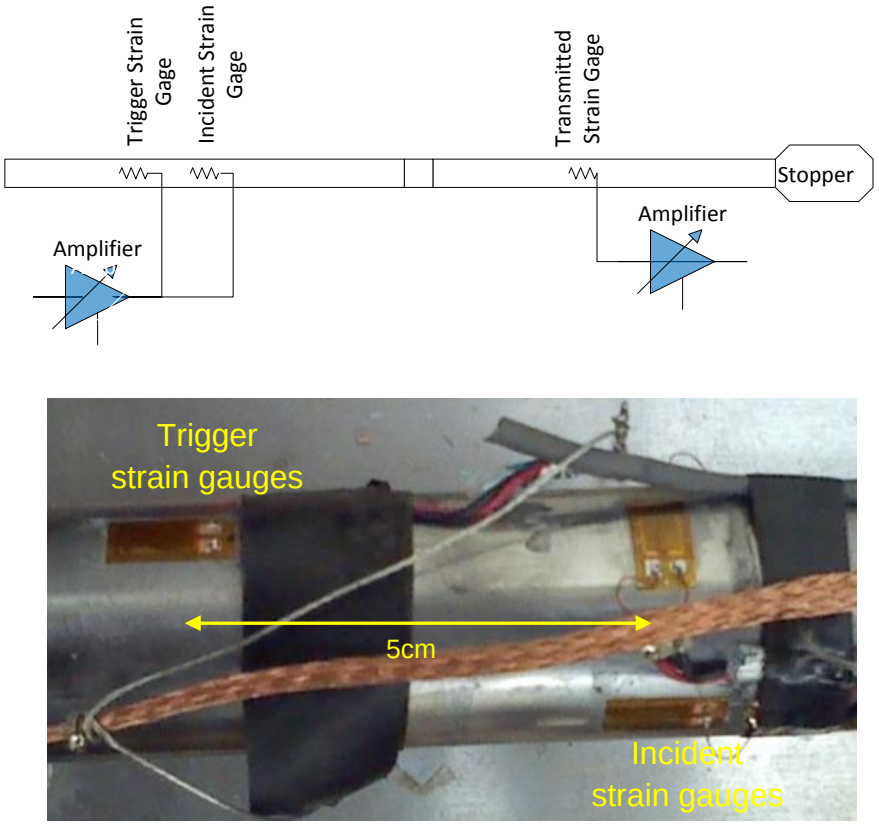

Figure 2.5 Location of the trigger and incident strain gauges on the incident bar.

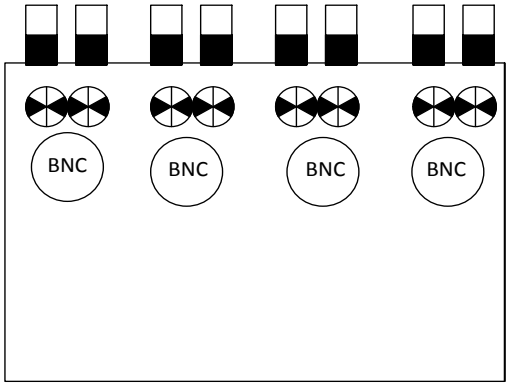

Figure 2.6 Schematic view of amplifier.

Figure 2.7 Aluminum 7075-T6 samples.

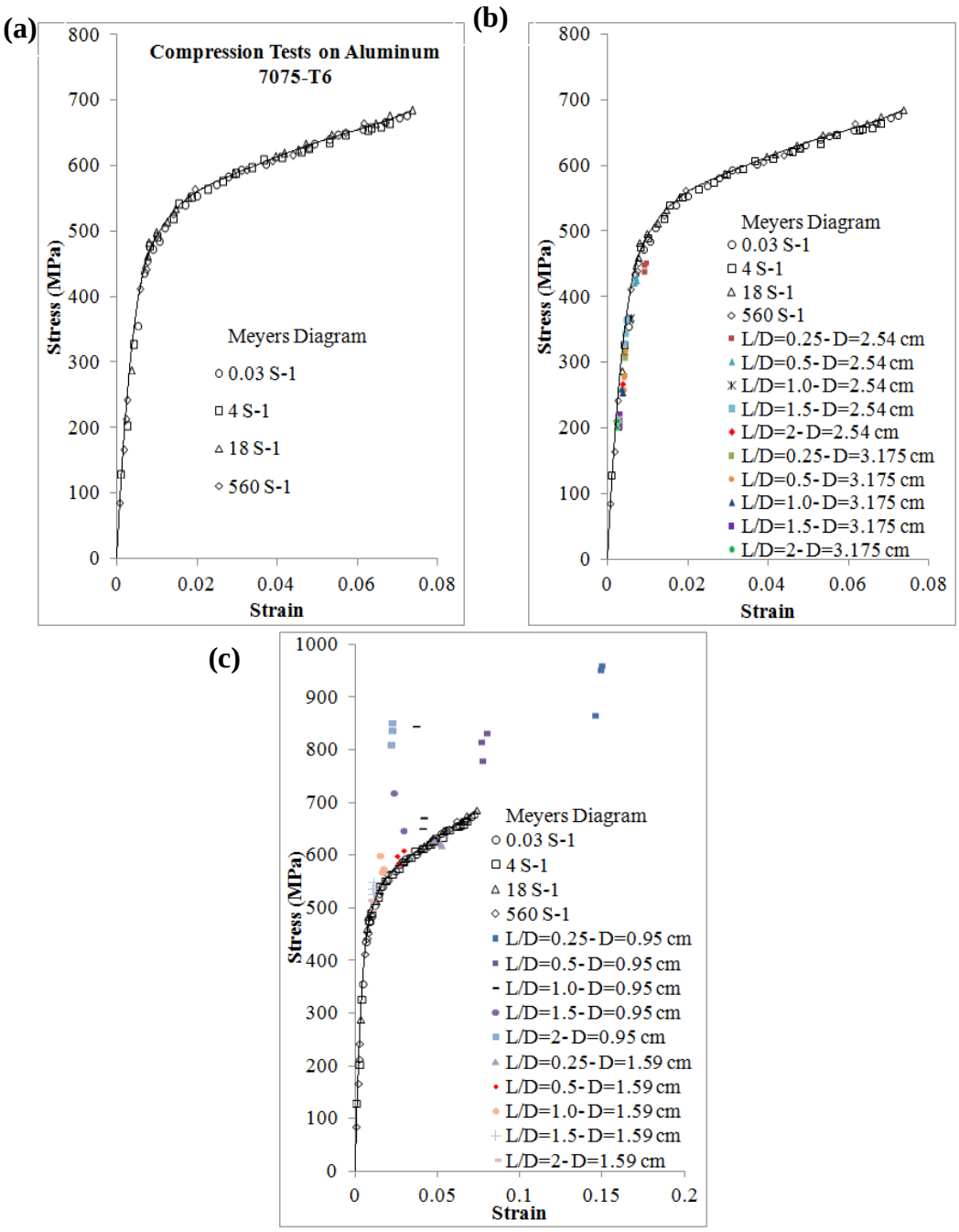

Figure 2.8 a) Stress-strain results of Al 7075-T6 at different strain rate (Maiden and Green 1966), specimens with b) 3.175 and 2.54 cm diameter, c) 1.59 and 0.95 cm diameter

Modified from Davies (1948)

CHAPTER 3

ROCK MATERIAL AND PROPERTIES

3.1 Rock type

In this research, two types of Utah sandstone were selected for evaluating the rock behavior in dry and saturated conditions. These two rocks were red and buff sandstone. Because of linear elastic response before failure, these rocks were suitable for studying dynamic behavior and for comparing static and dynamic strength.

These two types of sandstone are fine grained and have thin bedding layers, which are visible because of color differences (see Appendix for more detail). All of the samples were cored perpendicular to bedding from two rock blocks, each with a height of 2 ft.

3.2 Density determination

These rock blocks were cored with 5.46 and 3.175 cm diameter bits, and their lengths were cut based on ASTM standards for uniaxial, and triaxial tests (L/D=2.0). These lengths were also used for both static and dynamic tests. Density is an intrinsic, physical property of sandstone that is influenced by mineral content, discontinuities, and saturation. The density of all samples was measured in both dry and saturated conditions,

and the measured values are shown in Figures 3.1 and 3.2.

3.3 Porosity

Porosity of the rock is the ratio of porous volume in the rock occupied by air and water divided by the total volume of the sample. It can be expressed as:

$$P = \frac{V_w + V_a}{V_w + V_a + V_s} \tag{3.1}$$

where V_w is water volume, V_a is air volume and V_s is the volume that the solid material occupies. The rock sample porosity was determined by the water saturation method suggested by the International Society of Rock Mechanics, or ISRM (Ulusay and Hudson 2006). In the first step, the samples were left in an oven for 24 hours at a temperature of 105° Celsius. After cooling, the oven-dried weight of each sample was measured. Next, samples were placed into distilled water for 48 hours under 25 cm Hg vacuum. Saturation was considered to be achieved when all pore volumes were occupied by water. The saturated weight of the samples was measured after blotting the surface with a moist cloth. Based on dry and saturated weight and the density of distilled water at room temperature (997 kg/m^3), the porosity of each sample was measured and the results are shown in Figures 3.3 and 3.4. The sample sizes that were used for measuring porosity varied from the small cylinder size (3.175 cm) to the large cylinder size (NX-5.46 cm). The 3.175 cm core will be identified by the letters AX in that it is close to this standard size.

3.4 P and S wave velocities

Longitudinal (P wave) and transverse (S wave) wave velocities are intrinsic properties of solid materials. The P and S wave front shapes usually depend on the source characteristics that are used for wave generation. The ultrasonic pulse velocity technique was used for measuring the P and S wave velocity of rock samples. In this method, a piezoelectric transducer converts a mechanical deformation into an electrical charge and vice-versa. In this laboratory test, a frequency of 1.0MHz was used to measure P and S wave velocity of rock cylindrical samples with 3.175 and 5.46 cm diameters and an L/D ratio of 2.0. All samples that were used in this research followed the ASTM D2845. Based on this standard, the minimum lateral dimension of the specimen should be five times longer than the pulse wavelength, and the wavelength should be ten times longer than the average grain size of the rock samples (ASTM D2845).

The distance between the two transducers, the sample's length divided by the delay or arrival time, which is measured by an ultrasonic machine, gives the corresponding wave velocity in the rock specimens. The obtained P and S wave values are presented in Figures 3.5 and 3.6.

The dynamic elastic properties of these types of sandstones such as dynamic Young's modulus (E), the bulk modulus (K), and shear modulus (G) as a function of P-wave velocity (V_p), the S-wave velocity (V_s) and the rock density (ρ), can be calculated by using the following equations:

$$E = \frac{\rho V_s^2 (3V_p^2 - 4V_s^2)}{V_p^2 - V_s^2} \tag{3.5}$$

$$K = \rho (V_p^2 - \frac{4}{3} V_s^2) \tag{3.6}$$

$$G = \rho V_s^2 \tag{3.7}$$

Table 3.1 summarizes all of the dynamic elastic properties; i.e., the P and S wave velocities, Young's modulus, shear modulus, and bulk modulus of red and buff sandstones in two different sizes (AX 3.175 cm diameter and NX 5.398 cm diameter).

3.5 Tensile strength

The indirect tensile strength of the rock samples was determined by the Brazilian method. In this method, the compressive load is applied on a disk-shaped sample. In this case, most of the samples in a biaxial stress field break in tension at their uniaxial tensile strength when one of the principal stresses was compressive and the other was tensile. In the indirect tensile test, the test results were valid only when the fracture occurred in the center of the disk.

Tension strength values can be affected by the geometry and rate of loading the sample, as well as intrinsic properties of the rock specimen such as porosity and water content, and rock structures such as bedding and joints. To reduce the effect of these factors, disk specimens should have a thickness to diameter ratio of 0.3-1 (ASTM D3967. The tensile strength of rock in this test was calculated by Equation 3.8:

$$\sigma_t = \frac{2P}{\pi D t} \tag{3.8}$$

where P is the maximum load at failure, D is the diameter of specimen, and t is the height or thickness of the specimen. Table 3.2, Figures 3.7 and 3.8 show the measured tensile strength for red and buff sandstone in dry and fully saturated conditions. The averages and respective standard deviations are also shown. The measured tensile strength of the more porous buff sandstone is lower than that of the red sandstone.

3.6 Compressive strength

Rock strength is influenced by many factors, including load direction, intensity, duration, porosity, moisture, water content, and temperature. With respect to testing samples for compressive strength, the applied load for breaking the sample should work against friction, plastic deformation and generation of microcracks. During compressive failure, fine particles are created at the weakest inclined plane. Compressive strength may be measured by applying an uniaxial load to a cylindrical specimen under standard conditions. In this study, sandstone specimens with two different diameters, AX and NX, were prepared based on ASTM standards with a length to diameter ratio of 2:1. The sample diameter, as suggested in this standard, was chosen at more than ten times the maximum grain size (ASTM D7012). Small diameter specimens were used for comparing corresponding static compressive strengths with dynamic strengths of a similar L/D ratio.

After coring samples from rock blocks, each core was cut perpendicular to its axis at about a 2:1 L/D ratio, and then the ends were ground until the sample ends were parallel.

According to ASTM standard D7012, unconfined compressive strength (UCS) of intact rock samples is defined as the load at failure divided by the cross section area; it is worth noting that ASTM does not require visible destruction of the sample. All static unconfined and triaxial strength measurements for the sandstone samples tested and analyzed in this study were determined using a load frame equipped with an MTS Teststar IIM control system and Multipurpose Testware (operated and maintained by the Mining Engineering Department). This machine is used for both instruction as well as

research, and testing protocols have been established to conform to ASTM standards where applicable. For both UCS and triaxial samples, the assigned loading rate fell within acceptable limits (0.5 to 1 MPa/sec or slightly less).

With regards to the specific process employed for UCS testing of rock samples, this control system updates all transducer values at the system rate of 4096 Hz, and the axial force and displacement is added to the data file at 2-second intervals. The data at 2-second intervals are useful only for determining the elastic modulus. A failure detector is programmed in the procedure. The maximum force transducer value is updated with a new maximum value for every increasing increment of 250 lbf. If the force transducer value is 96% or less than the previous maximum sampled value, then a failure is detected, and the force ramp is automatically terminated (software trigger). The procedure then writes the maximum force along with the 2-second data stream to an output file. All UCS samples were tested with this procedure. Even though, some of the buff samples, BSS33, BSS34, BSS10, BSS13, BSS15, BSS37, BSS25, were not destroyed, all have failed according to the programmed failure detection criteria. In addition, posttest computer tomography (CT) scans suggest that all but two of these (BSS10 and BSS33) exhibit tangible internal inelastic deformation.

It may be argued that the failure detection level may be set too high for buff sandstone and similar materials. Confirming that the load required for destruction of a sample is equal to or more than the failure detection load was not considered as part of the scope of this thesis. However, based on the shape of the force-displacement curve (2-second samples), comparison of the failure detection value with other samples that did exhibit fracturing, and the behavior of samples equipped with strain gauges, the recorded

failure load for intact specimens appears reasonable. Experience has shown that setting failure detection at the 96% level is appropriate for most materials for either UCS or triaxial loading. Setting the level lower can cause difficulty and equipment damage especially when samples are tested under triaxial loading. To be consistent, all materials tested in this thesis under static conditions were subjected to the same failure detection criteria.

Oven-dried and fully saturated samples were used. For measuring Poisson's ratio, rosette strain gauges were installed on the dried samples. In the static strength experiments unconfined compressive strength (UCS) was measured perpendicular to the bedding. Tables 3.3 and 3.4 tabulate the compressive strength, Poisson's ratio, and Young's modulus in both dry and saturated conditions.

The measured compressive strength of AX (3.175 cm diameter) and NX (5.398 cm diameter) samples are shown in Figures 3.9 and 3. 10. The effect of sample size is manifest in the difference in the strength of the rock samples. As the size decreases, the weak joints or discontinuities diminish.

The Young's modulus, shear modulus, bulk modulus and Poisson's ratio are used in evaluating rock deformation under different loading conditions. The stress-strain ratios under uniaxial, shear stress, and compressibility application give the Young's, shear, and bulk modulus, respectively. The Poisson's ratio is defined as the ratio of the horizontal strain (transverse) to the corresponding axial strain during uniaxial loading within the elastic limit of the stress-strain curve. In the typical stress-strain curve for any sample, the modulus in the beginning of the loading cycle is low (due to crack closure and seating of the platens), and then, in the linear stress-strain part of the diagram, it becomes fairly

constant. Based on the stress-strain curve of rock samples, the value of the Young's modulus of dry and saturated red and buff sandstones was calculated using the tangent modulus (Figure 3.11 and 3.12). The tangent modulus is usually calculated at 50% of the ultimate strength in uniaxial testing, a method followed here.

The strength and deformability of these two types of sandstone were measured under static load conditions and were not useful in predicting rock behavior under dynamic conditions. The dynamic strength of the rocks was related to the loading rate, which was applied on the samples during the breakage, and as in blasting, was in the range of 10^{-2}-10^{4}/s. The dynamic behavior of these sandstones is explained in Chapter 4.

3.7 Triaxial strength

To describe the relationship between shear strength of materials and the applied normal stress, the Mohr-Coulomb failure envelope describes how brittle materials such as rock and concrete behave under stress. To obtain a failure envelope for a material, Mohr circles are plotted, and the failure envelope is determined as the best-fit line tangent to the available Mohr's circles. The failure envelope reveals the cohesion as a tangent line intercept and the tangent line slope reflects the angle of internal friction of the rock. For this purpose, several pairs of principal stress values (σ_3, σ_1) allow for the calculation of a failure envelope. Mohr circles can be shown in the Cartesian coordinate system by considering the relationship between the confining and axial stresses within the radius and center of the Mohr circles. By using the equation for a circle (Equation 3.9), a formula can be created for each stress sample in terms of the principal stress values ($\sigma_1$and σ_3).

$$(x-a)^2 + y^2 = r^2 \tag{3.9}$$

$$r = \frac{1}{2}(\sigma_1 - \sigma_3) \tag{3.10}$$

$$a = r + \sigma_3 \tag{3.11}$$

By substituting the r and a into Equation 3.9 for a circle and solving this equation for a positive y-value, the equation shows the Mohr circle for a stress sample (Eq. 3.10).

$$[x - (\sigma_3 + \frac{1}{2}(\sigma_1 - \sigma_3)]^2 + y^2 = [\frac{1}{2}(\sigma_1 - \sigma_3)]^2 \tag{3.12}$$

with the solution for y being

$$y = \sqrt{[\frac{1}{2}(\sigma_1 - \sigma_3)]^2 - [x - (\sigma_3 + \frac{1}{2}(\sigma_1 - \sigma_3)]^2} \tag{3.13}$$

Based on these equations, the Mohr circles for red and buff sandstones were constructed for both dry and saturated conditions. For this purpose, these rock samples were tested with three different confining pressures (7.0, 27.6, and 48.3 MPa). After fitting the Mohr-Coulomb failure envelope on these circles (Figures 3.13 and 3.14), the cohesion and internal friction angle of dry and saturated red and buff sandstones were calculated and are presented in Table 3.5.

Table 3.1 The average of dynamic elastic properties of red and buff sandstones

Type	Sample Size	Number of Samples	P-wave Velocity	S-wave Velocity	Dynamic Young's Modulus	Bulk Modulus	Shear Modulus
			m/s	m/s	GPa	GPa	GPa
Buff Sandstone	AX	40	2111.0	1453.4	9.0	3.4	4.3
	NX	20	2054.1	1469.6	8.6	2.7	4.4
Red Sandstone	AX	40	3977.0	2773.1	38.5	13.6	18.8
	NX	20	3943.5	2757.3	37.9	13.2	18.6

Table 3.2 The Brazilian tensile strength of red and buff sandstones

Sample Number		Thickness	Diameter	t/D	Peak Load	Time	loading rate	BTS
		mm	mm		kN	Sec	kN/s	MPa
Dry Red	RSBT-1	21.48	53.85	0.4	115.49	340	0.34	26.46
	RSBT-2	22.66	53.89	0.4	107.27	260	0.41	23.28
	RSBT-4	21.49	53.81	0.4	122.84	342	0.36	28.15
	RSBT-6	20.74	53.82	0.4	105.97	235	0.45	25.16
	RSBT-15	21.62	53.72	0.4	120.46	300	0.40	27.49
	RSBT-17	21.15	53.87	0.4	129.11	305	0.42	30.03
	RSBT-20	21.03	53.87	0.4	119.16	293	0.41	27.87
	RSBT-21	21.86	53.89	0.4	117.43	342	0.34	26.42
	RSBT-22	20.50	53.77	0.4	104.24	303	0.34	25.06
Sat. Red	RSBT-7	20.80	53.89	0.4	66.18	186	0.36	15.64
	RSBT-8	21.27	53.87	0.4	77.64	215	0.36	17.95
	RSBT-9	21.40	53.87	0.4	71.80	191	0.38	16.50
	RSBT-14	21.21	53.77	0.4	54.72	148	0.37	12.71
	RSBT-24	21.15	53.85	0.4	71.37	210	0.34	16.61
	RSBT-25	21.44	53.81	0.4	77.64	210	0.37	17.83
	RSBT-26	20.52	53.77	0.4	63.58	177	0.36	15.27
	RSBT-27	21.16	53.85	0.4	73.96	200	0.37	17.20
	RSBT-37	23.53	53.57	0.4	75.26	206	0.37	15.82
Dry Buff	BSBT-1	20.84	53.81	0.4	33.09	158	0.21	7.82
	BSBT-5	20.17	53.77	0.4	35.90	145	0.25	8.77
	BSBT-6	20.71	53.81	0.4	30.93	108	0.29	7.35
	BSBT-7	20.50	53.75	0.4	35.04	177	0.20	8.43
	BSBT-8	20.70	53.80	0.4	32.22	45	0.72	7.67
	BSBT-9	20.90	53.84	0.4	33.95	178	0.19	7.99
Sat. Buff	BSBT-19	20.80	53.77	0.4	17.52	67	0.26	4.15
	BSBT-21	21.01	53.76	0.4	24.22	80	0.30	5.68
	BSBT-22	20.40	53.75	0.4	22.06	67	0.33	5.33
	BSBT-23	20.90	53.80	0.4	24.87	80	0.31	5.86
	BSBT-25	21.67	53.77	0.4	22.92	60	0.38	5.21
	BSBT-26	21.36	53.80	0.4	25.09	82	0.31	5.78

Table 3.3 Compressive strength, Young's modulus, and Poisson's Ratio for red and buff sandstones (~5.46 cm diameter)

Sample No.		Length	Diameter	L/D Ratio	Loading Rate	UCS	Young's Modulus
		mm	mm		kN/sec.	MPa	GPa
Dry Red	RS20	110.1	53.5	2.06	1.31	179.3	24.78
	RS19	110.1	53.8	2005	1.33	180.4	24.67
	RS18	110.1	53.5	2.06	1.33	174.3	23.75
Sat. Red	RS2	110.2	53.5	2.06	1.33	123.4	23.03
	RS3	110.1	53.8	2.05	1.33	122.1	22.28
	RS4	110.1	53.9	2.04	1.33	121.7	21.39
	RS5	109.8	53.8	2.04	1.33	122.0	22.94
	RS6	110.1	53.9	2.04	1.33	122.0	21.12
	RS7	107.9	53.6	2.01	1.33	122.6	21.71
Dry Buff	BS20	109.9	53.8	2.04	1.33	66.9	10.15
	BS19	109.6	53.8	2.04	1.33	61.7	9.04
	BS18	110.3	53.8	2.05	1.33	65.5	9.79
Sat. Buff	BS1	109.9	53.8	2.04	1.33	46.8	8.06
	BS2	110.2	53.8	2.05	1.34	50.6	8.63
	BS3	108.6	53.8	2.02	1.33	48.7	8.39
	BS4	109.9	53.8	2.04	1.33	47.8	8.18
	BS5	109.8	53.8	2.04	1.33	49.0	8.72
	BS6	110.0	53.8	2.04	1.34	49.2	8.88

Sample No.		Poisson's Ratio	
		ST-St	St-LVDT
Dry Red	RS20	0.24	0.25
	RS19	0.22	0.21
	RS18	0.25	0.26
Dry Buff	BS20	0.30	0.31
	BS19	0.32	0.31
	BS18	0.25	0.27

Table 3.4 Compressive strength, Young's modulus, and Poisson's Ratio for red and buff sandstones (~3.175 cm diameter)

Sample No.		Length	Diameter	L/D Ratio	Loading Rate	UCS	Young's Modulus
		mm	mm		kN/sec.	MPa	GPa
Dry Red	RSS32	65.8	31.5	2.09	1.20	205.6	26.39
	RSS29	65.4	31.5	2.08	1.33	207.4	25.81
	RSS13	65.5	31.5	2.08	1.33	185.1	24.79
	RSS31	65.4	31.4	2.08	1.33	192.4	25.23
	RSS11	65.5	31.5	2.08	1.33	190.8	26.04
	RSS44	65.5	31.5	2.08	1.33	189.7	25.45
Sat. Red	RSS15	65.8	31.5	2.09	1.33	156.0	23.70
	RSS21	65.8	31.5	2.09	1.33	153.6	23.87
	RSS33	65.3	31.5	2.07	1.33	150.5	23.37
	RSS34	65.8	31.4	2.09	1.19	149.1	21.84
	RSS35	65.0	31.4	2.07	1.33	154.2	23.78
	RSS36	65.9	31.5	2.10	1.33	158.1	24.00
Dry Buff	BSS33	66.2	31.2	2.12	1.31	Note[a]	12.61
	BSS34	66.6	31.3	2.13	1.31	76.1	13.03
	BSS10	65.5	31.3	2.09	1.30	Note[a]	12.55
	BSS13	66.2	31.3	2.11	1.33	80.2	12.39
	BSS12	66.2	31.4	2.11	1.33	72.2	12.04
	BSS27	66.3	31.4	2.11	1.33	72.2	12.92
	BSS40	66.4	31.4	2.11	1.33	71.9	11.58
Sat. Buff	BSS15	66.4	31.3	2.12	1.33	60.6	11.06
	BSS37	65.4	31.3	2.09	1.33	64.4	11.75
	BSS25	66.5	31.3	2.12	1.33	63.3	11.41
	BSS18	66.3	31.3	2.12	1.33	61.0	10.59

[a]Result omitted due to no discernable fractures in tested sample.

Sample No.		Poisson's Ratio	
		ST-St	St-LVDT
Dry Red	RSS32	0.18	0.16
	RSS29	0.25	0.19
	RSS13	0.28	0.21
	RSS31	0.30	0.22
Dry Buff	BSS33	0.38	0.31
	BSS34	0.41	0.40
	BSS10	0.47	0.41

Table 3.5 Frictional properties of red and buff sandstones in dry and saturated conditions

Type	Property	Dry sample	Sat. sample
Buff Sandstone	Friction Angle (φ°)	30.1	27.7
	Cohesion (MPa)	19.4	15.4
Red Sandstone	Friction Angle (φ°)	45.4	43.5
	Cohesion (MPa)	36.7	27.4

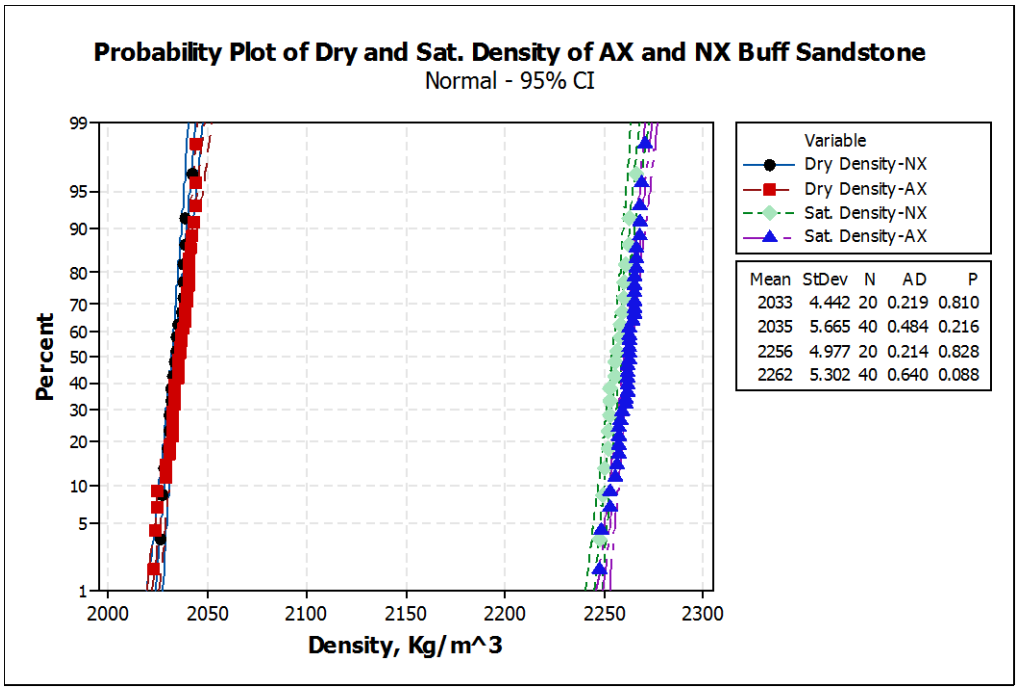

Figure 3.1 Dry and saturated density of buff sandstone.

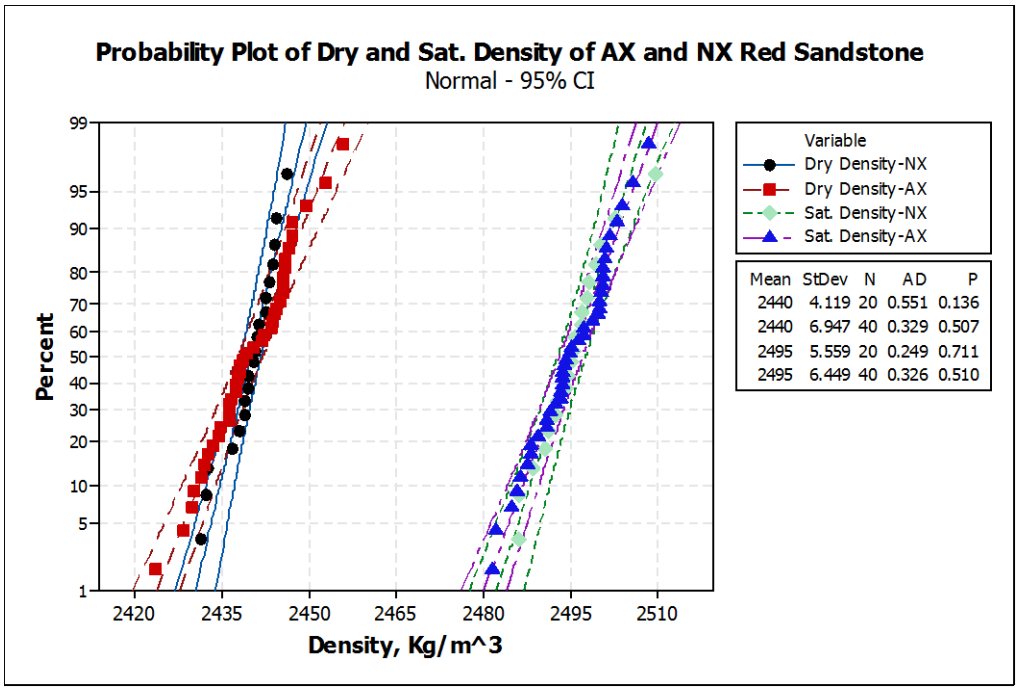

Figure 3.2 Dry and saturated density of red sandstone.

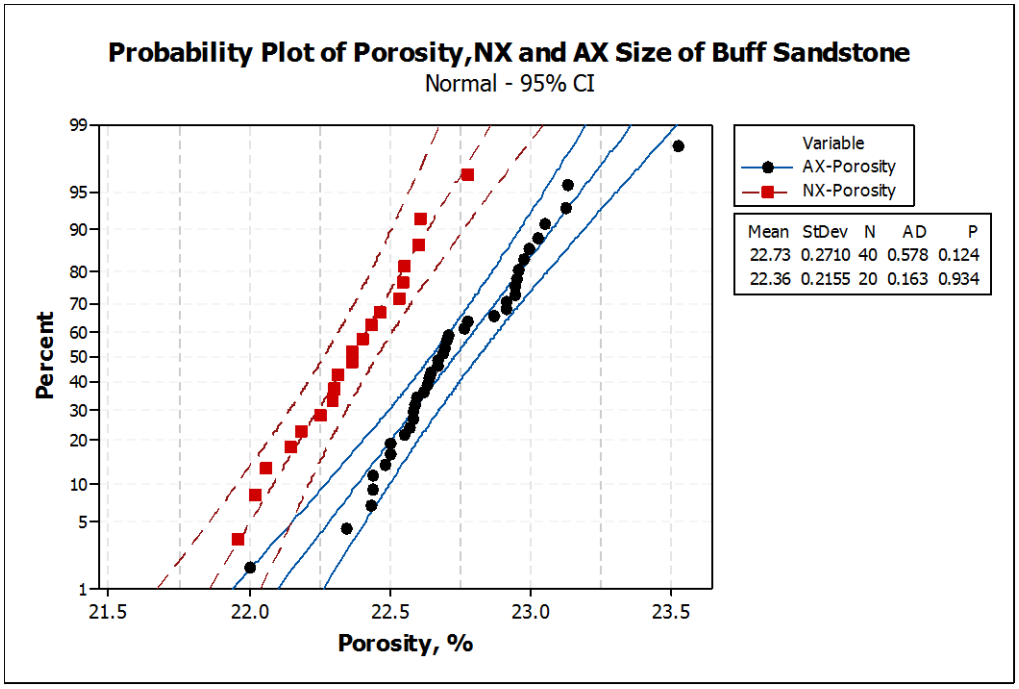

Figure 3.3 Porosity of buff sandstone.

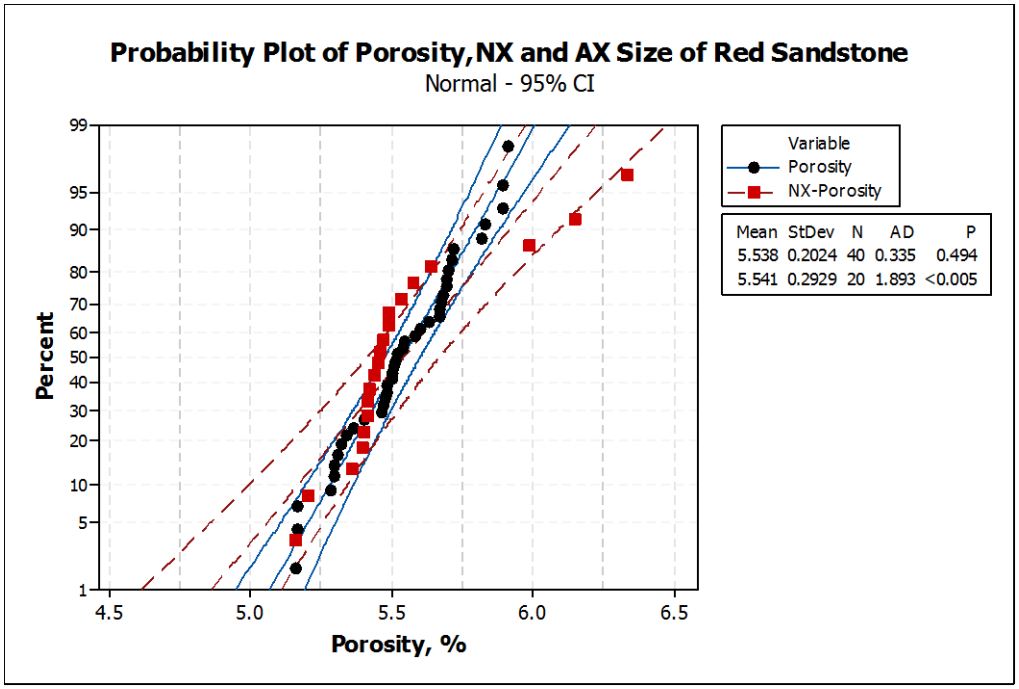

Figure 3.4 Porosity of red sandstone.

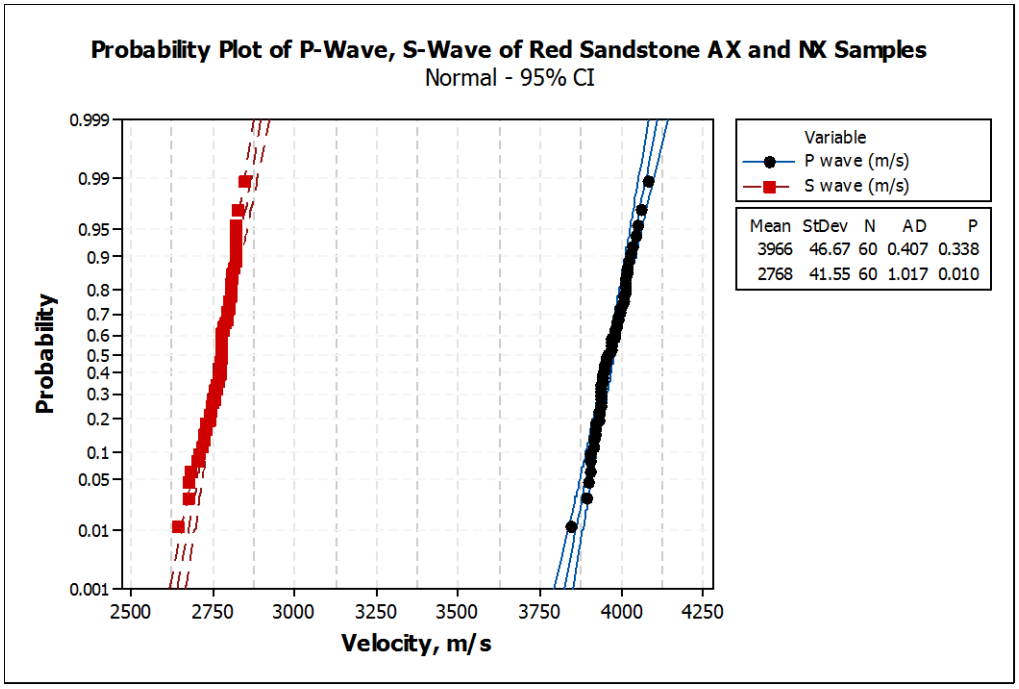

Figure 3.5 P and S waves' velocity of red sandstone.

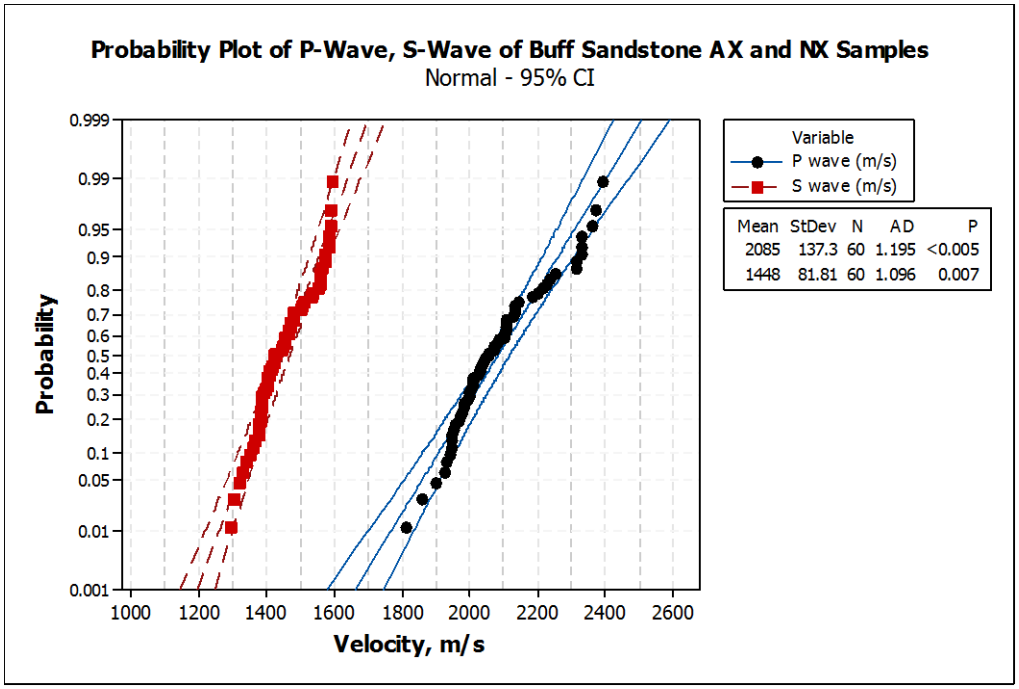

Figure 3.6 P and S waves' velocity of buff sandstone.

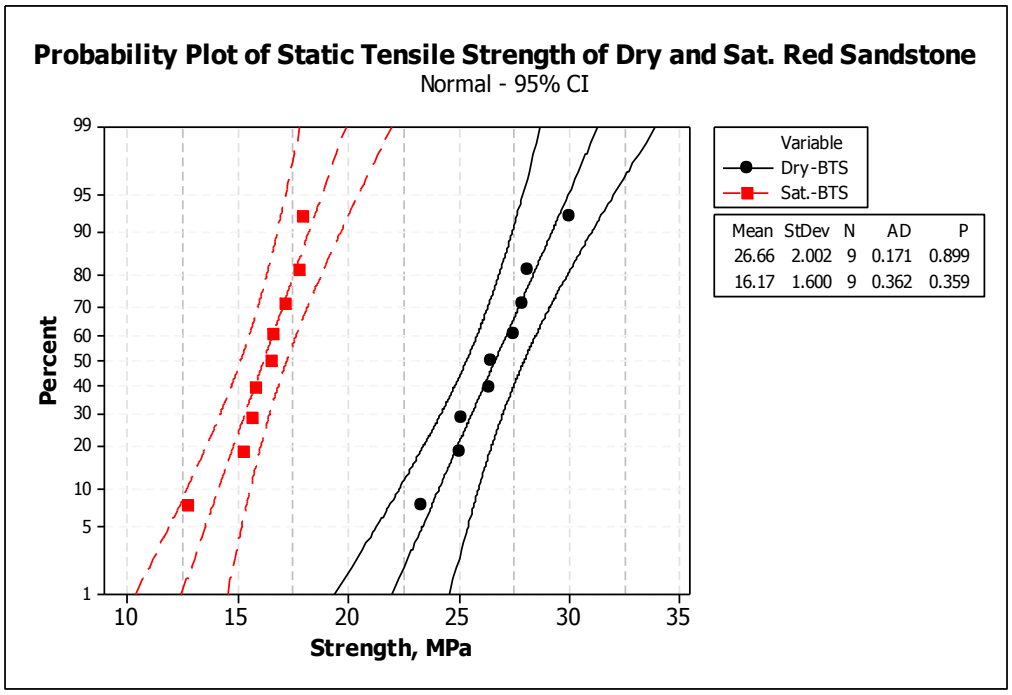

Figure 3.7 Tensile strength of dry and saturated red sandstone.

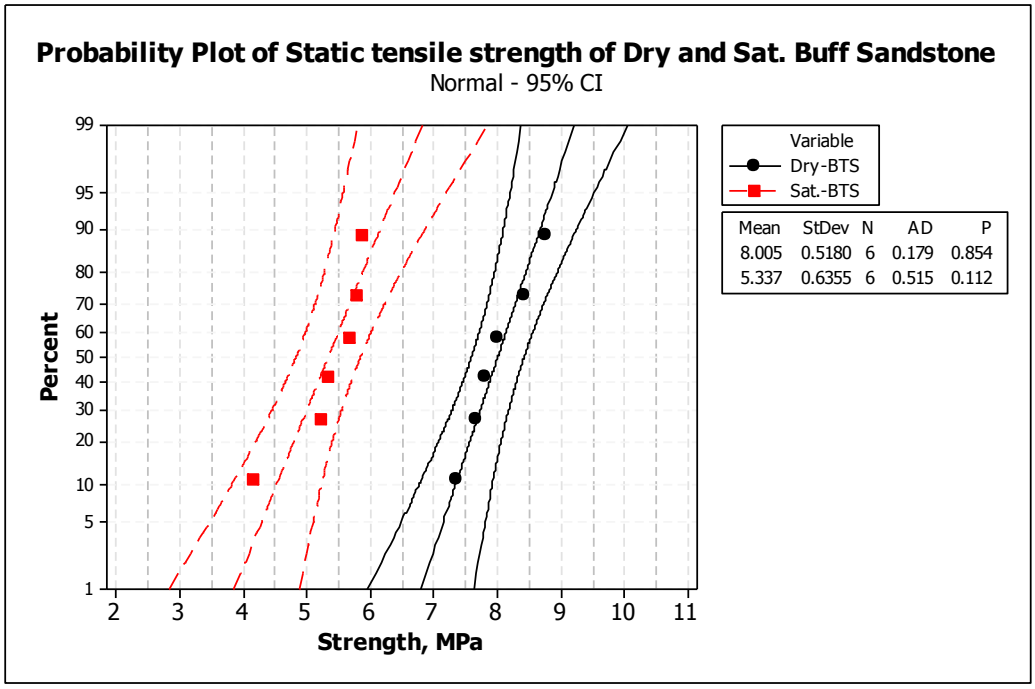

Figure 3.8 Tensile strength of dry and saturated buff sandstone.

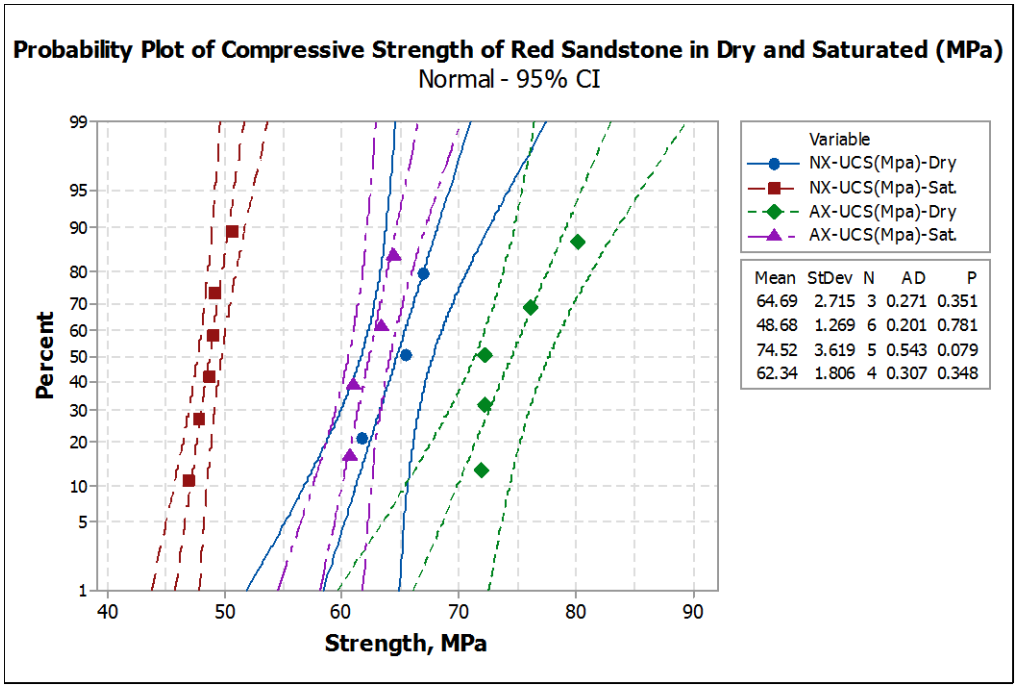

Figure 3.9 Compressive strength of dry and fully saturated buff sandstone.

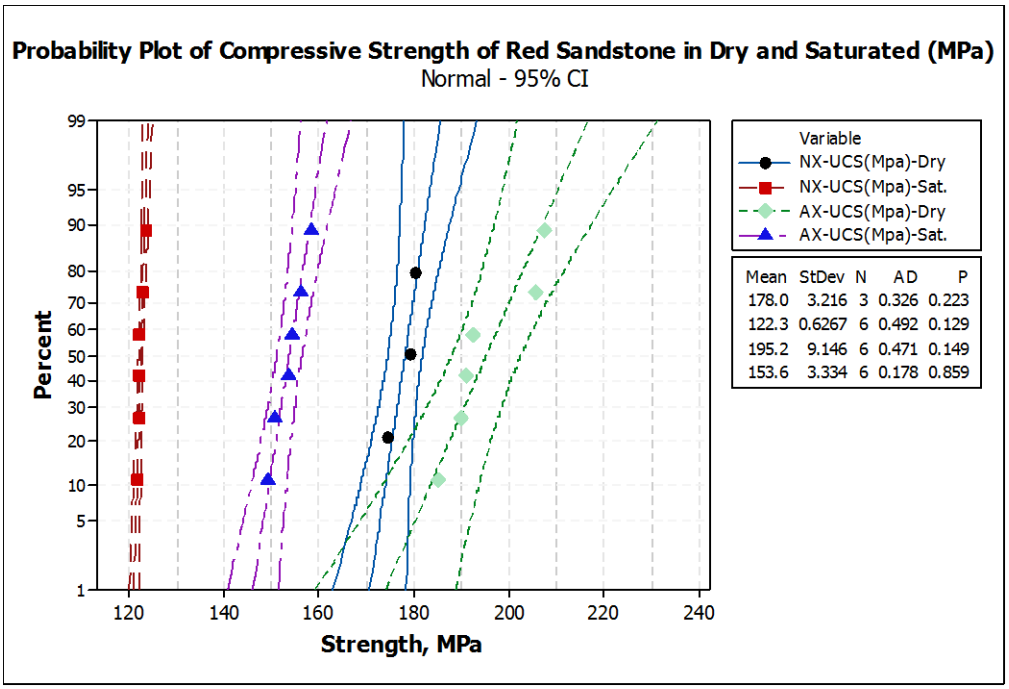

Figure 3.10 Compressive strength of dry and fully saturated red sandstone.

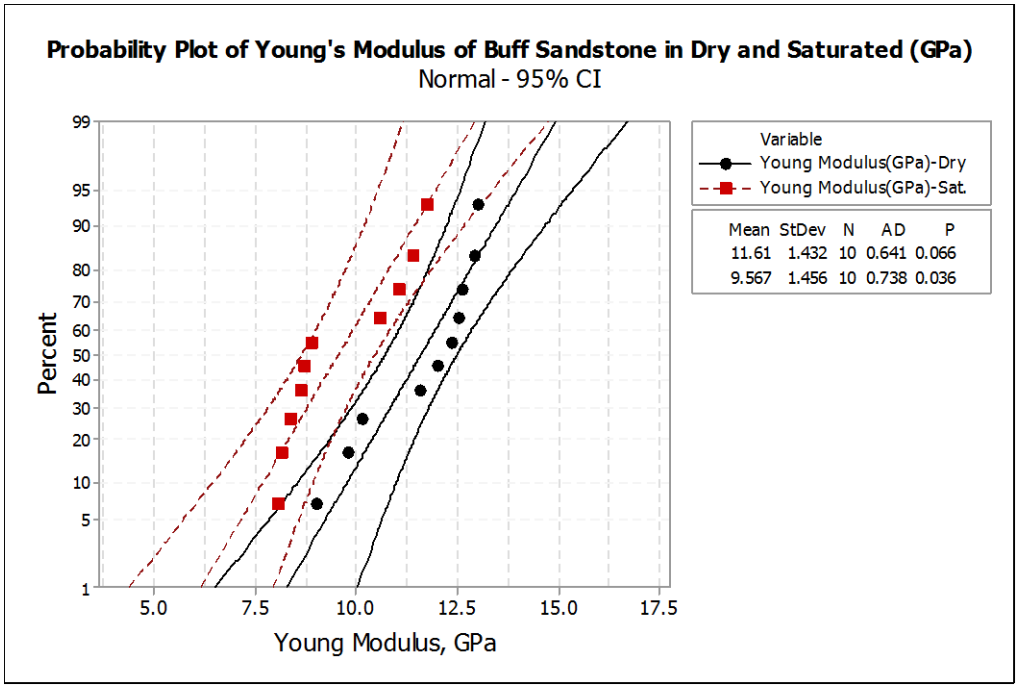

Figure 3.11 Young's modulus of dry and fully saturated buff sandstone.

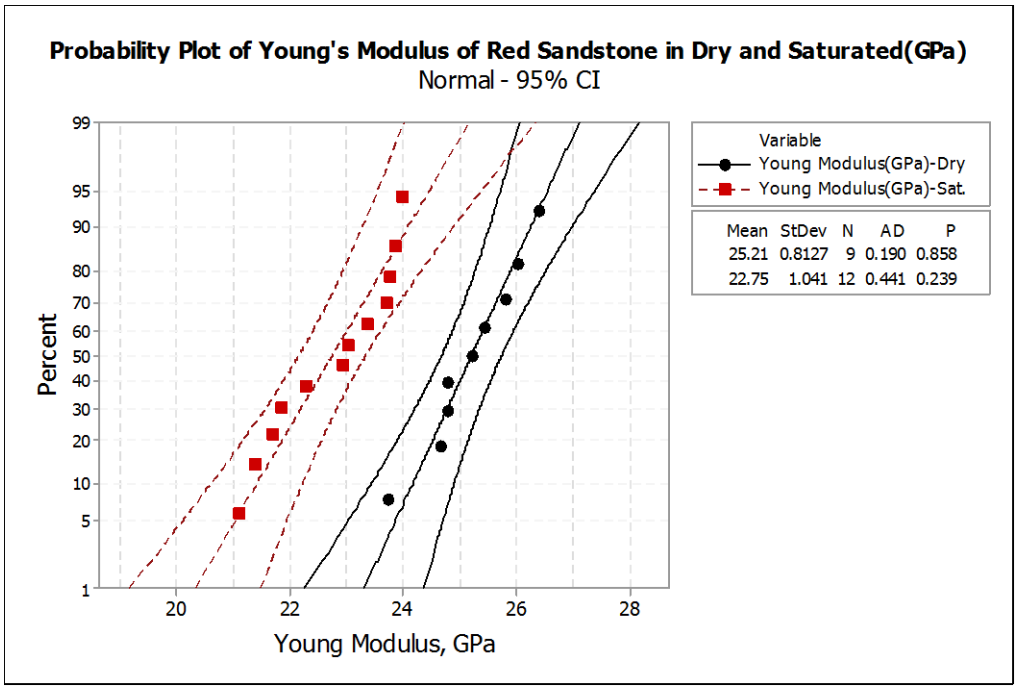

Figure 3.12 Young's modulus of dry and fully saturated red sandstone.

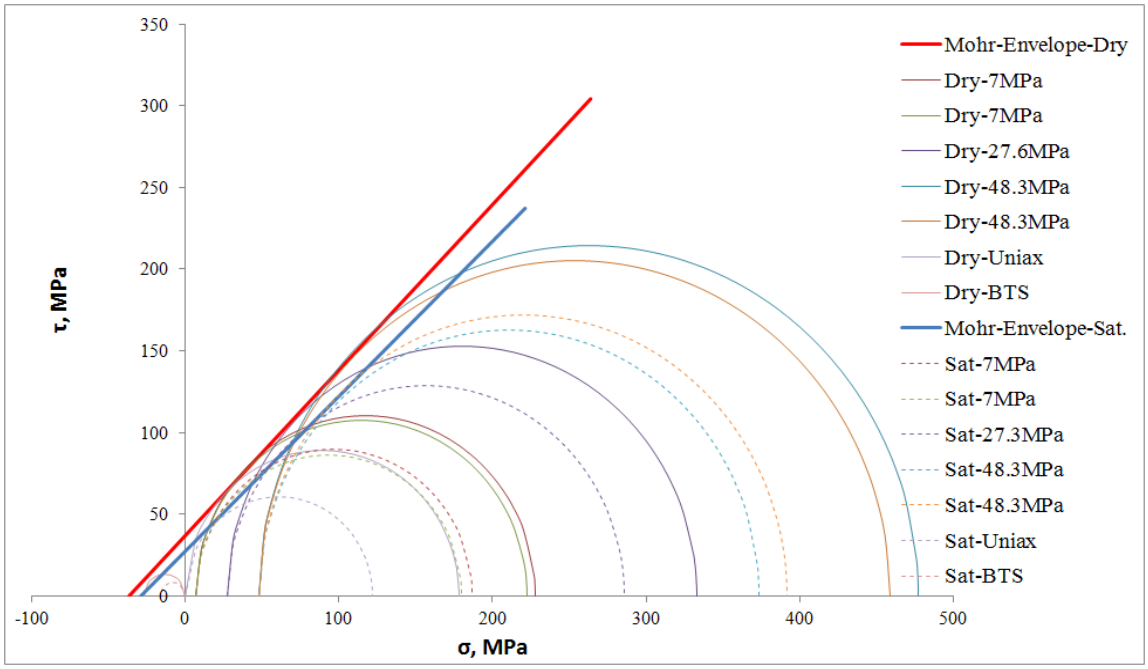

Figure 3.13 Mohr-Coulomb failure envelope for red sandstone.

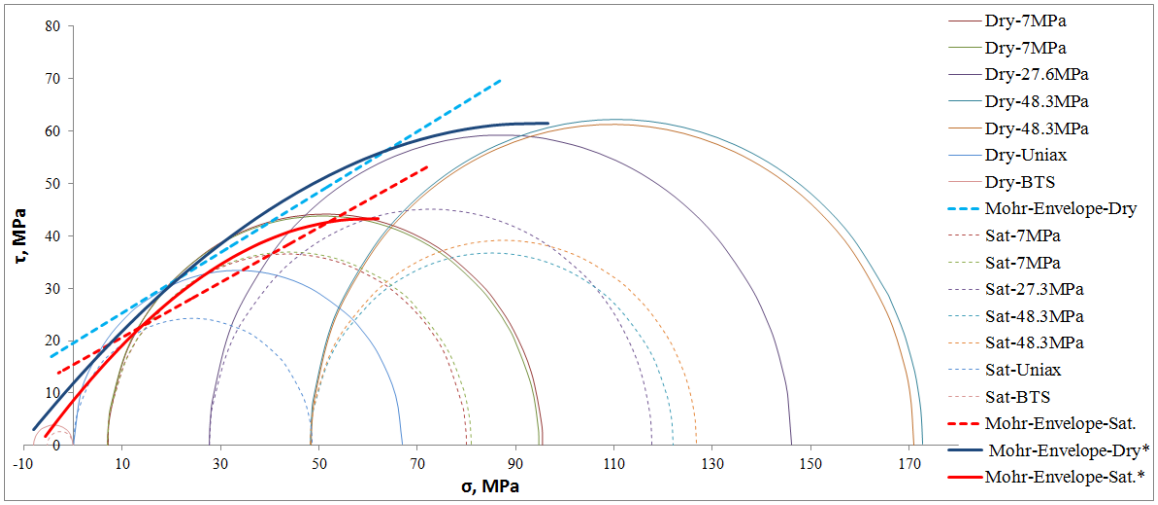

Figure 3.14 Mohr-Coulomb failure envelope for buff sandstone.

*Solid line Mohr-Envelops shows how buff sandstone is deformable and how its behavior depends on confining stress.

CHAPTER 4

ROCK BEHAVIOR UNDER HIGH STRAIN RATES

4.1 Introduction

Rock dynamic strength is usually measured when a rock is subjected to a high loading rate during mining, tunneling, and hydrofracturing (fracking) operations. In mining, the ore extraction process consists of drilling, blasting, crushing, and grinding. During these processes the rock encounters different dynamic stresses. In processes of creating open space underground, a better understanding of rock behavior under these dynamic loads is essential in designing a suitable drilling and blasting pattern and in using an optimum amount of suitable explosives (Atchison and Pugliese 1964). In fracking operations in the oil industry, knowledge of the dynamic response of rocks might help in improving design of perforating charges, tools, and fracturing processes. Modeling of these processes and predicting results during drilling, blasting, and fracking are becoming increasingly important economically and, in some cases, because of environmental pressures. For these purposes, it is very useful to know the strength properties of rocks under high strain rate conditions for the analytical modeling of rocks.

Rock strength under dynamic conditions has been investigated since the early work of Rinehart (1965), who measured the dynamic tensile strength of rock based on the

stress wave reflection that was generated by a detonator (Rinehart, 1965).

Goldsmith (1966) was the first researcher to use Hopkinson bars made of rocks. In his experiment, the impact of steel ball bullets generated the strain wave along the rock bar and was measured by using surface mounted strain gauges on the rock bars (Goldsmith, 1966). As cited by Prasad (2000), the Hopkinson bar, or some alteration of this machine, has been used in past investigations of rock dynamic behavior under compression by Kumar (1968), Hakalehto (1969), Lindholm (1974), Lundberg (1976), Buchar and Bilek (1981); under tension by Birkimer (1971), Mohanty (1988); and under torsion by Lipkins et al. (1980). Shockey et al. (1974) and Grady and Kipp (1979) used the plate impact induced spall for dynamic measurement purposes. Table 4.1 shows the dynamic compressive strength measured by SHPB, strain rates, and the ratio of dynamic to static strength (Prasad 2000). There are a variety of means that can be used for measuring the dynamic strength of rocks such as drop weight, pendulum, spring or explosively driven hammer, and Split Hopkinson Pressure Bar machine. In this research, the compression and tensile dynamic strength of two types of sandstone (either oven dried or fully saturated) were measured by use of a SHPB.

4.2 Red sandstone

As stated earlier, two rock types were selected for this study. Samples were prepared from cores drilled from rock blocks. For the dynamic compressive experiment, specimens were cut and ground with a 3.175 cm diameter core, and for dynamic tensile tests, samples were cut with a 5.40 cm diameter core. Nineteen red sandstone cylindrical samples with 3.175cm diameters and L/D ratios of 2.0 were used in dynamic compressive

tests. Nineteen red sandstone disk samples with a thickness/diameter (t/D) ratio of 0.4 were used in dynamic tensile tests. In addition, 12 samples with an L/D ratio of 2.0 were prepared for measuring the loading rate effect on rock compressive strength under fast loading conditions.

4.2.1 Dynamic compressive strength of red sandstone

Nineteen specimens were prepared for measuring the compressive strength of the red sandstone with about 5.5% porosity. For evaluating the moisture content effects on the dynamic compressive strength of this type of rock, eight samples were fully saturated for 48 hours under vacuum (25 cm-Hg), and 11 specimens were placed into an oven for 48 hours and completely dried (105°C). Following this, measurements were taken to investigate the effect of water content on dynamic compressive strength. Based on the tests on both oven-dried and fully saturated rocks by SHPB, rock strength in static conditions among selected rock specimens is compared in Chapter 5. All of the tests for red sandstone were conducted at an impact velocity of 20 m/s, which corresponds to a gas gun pressure of approximately 100 psi. The results in terms of acquired strain signal versus time, time histories of strain rate, stress at both ends of sample, average stress along the sample, and stress-strain behavior are shown in Figures 4.1–4.5 for sample RSS10.

Based on the results given in Table 4.2 and Figure 4.6, it was observed that water content reduced rock strength. Furthermore, saturated rock samples were broken at a lower strain, and increasing the pore fluid pressure in a rock sample caused a reduction in cohesion and affected rock strength (Figure 4.7). Another interesting phenomenon in the

results was observed. Using the same impact velocity in all of these specimens, the loading rate in the saturated samples was about 60% of the loading rate in dry specimens (Figure 4.8).

4.2.2 Dynamic compressive strength of red sandstone under fast loading condition

As mentioned in Table 4.2 and Figure 4.8, the loading rate for dynamic experiments on rock specimens was about 10,000–16,000 MN/sec., and increasing the loading rate in comparison to the static test (1.3 kN/s) increased rock strength. To cover the range between 1.3 kN/s and 16,000 MN/s and collect some in this range, a servo-control machine with MTS controller had the maximum loading rate capacity of 265 kN/s. Twelve specimens were tested at this capacity in oven-dried and saturated conditions. As shown in Figure 4.9, the samples were loaded in less than 3 seconds. Based on the results shown in Table 4.3 and Figure 4.10 water content reduced the rock strength by 22% (219.4 MPa to 170.8 MPa; Figure 4.10) in fast loading conditions.

4.2.3 Dynamic tensile strength of red sandstone

In this research, a modified SHPB technique was used for measuring the dynamic tensile strength of both red and buff sandstone. Similar to the compressive test by SHPB, the sample was sandwiched between the incident and transmitted bars (Figure 4.11). The dynamic load was generated by the striker bar being launched by a low pressure gas gun (25 psi) and impacting the incident bar.

In this experiment, as before, by using the three stress waves identified in Figure 4.12, the forces P_1 and P_2, were calculated as:

$$P_1 = EA[\varepsilon_I(t) + \varepsilon_R(t)] \quad (4.1)$$

$$P_2 = EA\varepsilon_T(t) \quad (4.2)$$

where E and A are the Young's modulus and the cross section of the bars, respectively. The strain rate and dynamic tensile strength (Figures 4.13, 4.14) were then calculated using the following equation:

$$\sigma_t = \frac{2P_{max}}{\pi DB} \quad (4.3)$$

where, σ_t is the tensile strength, P_{max} is the maximum value of loading P_2, D is the sample diameter and B is the disk thickness (Bieniawski and Hawkes 1978).

For evaluating the water content effects on dynamic tensile strength of red sandstone, 18 specimens were prepared. Nine samples were tested in an oven-dried condition, and the remaining nine samples were saturated for 48 hours and then tested. Table 4.4 and Figure 4.15 illustrate the results of the dynamic tensile tests on dry and saturated red sandstone specimens. Based on these results, it can be concluded that moisture has the same effects on dynamic tensile strength of red sandstone as it does on static tensile strength. The rock's strength decreased by about 18% (30.42 MPa to 24.97 MPa –Figure 4.15), which reduced the failure strain and loading rate.

4.3 Buff sandstone

The effect of porosity and water content on the dynamic behavior of the buff Utah sandstone with 22.5% porosity was also investigated. The required samples were prepared from cores drilled from rock blocks, and for each experiment specimens were made by cutting and grinding a 3.175 cm diameter core for the dynamic compressive strength experiment. For dynamic tensile tests, samples were cut from 5.40 cm diameter

cores. Cylindrical samples with a L/D ratio of about 2.0 (15 samples for SHPB and eight samples for fast loading) and 14 disk samples with a t/D ratio of about 0.4 were used for measuring the dynamic tensile strength of this sandstone.

4.3.1 Dynamic compressive strength of buff sandstone

Similar measurements were carried out on the buff sandstone samples as on the red sandstone samples to measure the dynamic compressive strength, porosity, and water content effects on its dynamic strength. Various parameters from these specimens and test results are given in Table 4.5. Experiments on buff sandstone were carried out at an impact velocity of about 20 m/s that was produced by a gas pressure of 100 psi, but because of the low strength of this rock, the recorded results were very noisy. To eliminate this problem, the gas pressure was reduced to 75 psi. The impact velocity in this case was about 17 m/s. The results of the test in terms of recorded pulses by the data acquisition system, time histories of strain rate, stress along the samples, and dynamic stress strain behavior are shown in Figures 4.16 to 4.20. To evaluate the effect of water content and porosity on the dynamic strength and loading rate, the dynamic strength of buff sandstone and loading rate obtained from these experiments are summarized in Figures 4.21 and 4.22. It is noted from Figure 4.21 that water content and pore pressure in this rock type reduced the dynamic compressive strength by about 17.5% (150 MPa to 124.1 MPa, Figure 4.21). As the triaxial tests in the last chapter showed, water content reduced the cohesion of this rock by about 8%, but increasing the pore pressure in the saturated samples reduced loading rate by about 15% in comparison to dry buff sandstone (Figure 4.22).

4.3.2 Dynamic compressive strength of buff sandstone under fast loading

Experiments were carried out on buff sandstone to determine the rock strength at which fast loading failure initiated. In this case, as in red sandstone, eight samples in oven-dried and fully saturated conditions were tested with a servo-control machine at an average loading rate of about 215 kN/s. Dry samples failed in less than 6 seconds, whereas fully saturated samples took about 12 seconds. As seen in the results (Figures 4.23, 4.24 and Table 4.6) the water content reduced the rock strength by about 22% in the fast loading condition.

4.3.3 Dynamic tensile strength of buff sandstone

As mentioned before, the SHPB was used to conduct an indirect tension test for measuring the dynamic tensile strength. A close-up view of one of the dynamic tensile test disc samples in the SHPB machine that was sandwiched between the incident and transmitted bars shows that the specimen was loaded diametrically, and it failed due to tension along the loading diameter near the center (Figure 4.25). The dynamic load for this experiment, similar to the red sandstone, was generated by the impact of the striker bar on the incident bar. The striker bar was launched by a low gas pressure (25 psi), and all of the experiments were carried out at a striker bar velocity of 12.5 m/s. For evaluating the moisture effect on dynamic tensile strength of buff sandstone, 14 samples were tested. Seven samples were tested in an oven-dried condition, and seven samples were saturated for 48 hours before testing. The dynamic strength parameters obtained from these tests are given in Table 4.7. The results in terms of recorded signals, time histories of stress, strain rate, and stress-strain curve for sample BSBT2, as tested in the same condition as

others, are shown in Figures 4.26 to 4.30.

Table 4.7 and Figure 4.30 illustrate the results of the dynamic tensile test on dry and saturated buff sandstone specimens. Based on these results, it can be concluded that moisture has the same effect on tensile strength of buff sandstone as it does on red sandstone. It decreases rock strength by about 22% (Figure 4.30) under dynamic tensile load, which reduces the failure strain and loading rate.

4.4 Loading rate effects on rock strength

Loading rate effects on rock strength are measured through laboratory experiments, and many researchers attempt to derive an empirical equation to find the relationship between rock specimen strength and loading rate (strain rate). Lankford (as cited by Zhou and Zhao 2011), using limestone specimens, proposed the following equation based on the uniaxial compressive strength and strain rates in the range of 10^{-6}-10^{4} s^{-1}:

$$\sigma_{dc} \propto \begin{cases} \dot{\varepsilon}^{1/(1+n_c)} & \dot{\varepsilon} < 10^2 s^{-1} \\ \dot{\varepsilon}^{1/n} & \dot{\varepsilon} > 10^2 s^{-1} \end{cases} \tag{4.4}$$

where σ_{dc} is the uniaxial dynamic compressive strength, $\dot{\varepsilon}$ is strain rate, n and n_c are material constants that are equal to 0.3 and 130, respectively.

Another study of compressive strength in the strain rate range of 10^{-6} to 10^{3} s^{-1} was done by Olsson (as cited by Zhou and Zhao 2001) on tuff rocks. Both Olsson and Lankford used a strain rate less than critical value ($76s^{-1}$) in their experiments, resulting in a slight increase in compressive strength. The rock strength increased with strain rate when the strain rate was higher than critical (Zhou and Zhao 2011).

$$\sigma_{dc} \propto \begin{cases} \dot{\varepsilon}^{0.007} & \dot{\varepsilon} < 76 s^{-1} \\ \dot{\varepsilon}^{0.35} & \dot{\varepsilon} > 76 s^{-1} \end{cases} \tag{4.5}$$

Based on similar tests on granite at strain rates of 10^{-4} to 10^{0} s^{-1}, Masuda et al. (1987) noted that the dynamic compressive strength of rock increases with the strain rate. The relationship is given as:

$$\sigma_{dc} = C\ log(\dot{\varepsilon}) + \sigma_c \tag{4.6}$$

where σ_c is the static uniaxial compressive strength, and *C* is a constant for the rock material. In the same condition, Zhao (as cited by Zhou and Zhao 2011) suggested another relationship based on his experiments on granite:

$$\sigma_{dc} = RSC_d log(\dot{\sigma}_{dc}/\dot{\sigma}_{sc}) + \sigma_{sc} \tag{4.7}$$

where $\dot{\sigma}_{dc}$ is the dynamic loading rate, $\dot{\sigma}_{sc}$ is the quasistatic loading rate, σ_{sc} is the uniaxial compressive strength at quasistatic loading rate (0.5-1.0 MPa/s), and RSC_d is the dynamic rock strength constant for the rock.

For buff sandstone specimens that were tested at different loading rates, as given in Figures 4.31 and 4.32 and summarized in Table 4.8, increasing the loading rate from 1.3 kN/s (static test) to 215 kN/s in fast loading experiments led to an increase in rock strength by about 1.15 and 1.08 times for dry and saturated conditions, respectively. In comparison to static strength, increasing the loading rate from 215 kN/s (fast loading) to 8.0E6 kN/s in dynamic tests caused an increase in dynamic compressive strength of about 2.01 and 1.99 times under dry and saturated conditions, respectively. In indirect tensile experiments (Brazilian Tensile Strength-BTS) that were conducted using the BTS machine and the SHPB, the dynamic increase factor (DIF) for dry and saturated specimens of buff sandstone was 1.1 and 1.3, respectively (Figure 4.33). The DIF values and variation of buff sandstone specimens with different strain rates are given in Table 4.8.

The strength of red sandstone also increases with increasing loading rate. As seen in the results given in Figures 4.34-4.36 and summarized in Table 4.8, increasing the loading rate from 1.3 kN/s to 250 kN/s caused an increase in the rock strength by about 1.12 times under dry and 1.11 times under saturated conditions. In addition, the dynamic increase factor in the SHPB results for dry and saturated conditions was about 1.36 and 1.41 in compression, and 1.14 and 1.54 in tensile strength, respectively.

As aforementioned, and also as seen in Figures 4.37 and 4.38, it can be concluded that rock strength is affected by loading rate. The compressive strength versus loading rate plotted on a logarithmic scale shows that compressive strength rapidly increases with loading rate.

Empirical equations were derived to express the relationship between loading rate and rock material strength in dry and saturated conditions for the selected sandstones.

$$\sigma_{dc-red\ sandstone} = \begin{cases} UCS_{dry} LR^{0.0182} \\ UCS_{sat.} LR^{0.0214} \end{cases} \tag{4.8}$$

$$\sigma_{dc-buff\ sandstone} = \begin{cases} UCS_{dry} LR^{0.0444} \\ UCS_{sat.} LR^{0.0472} \end{cases} \tag{4.9}$$

where σ_{dc} is the uniaxial dynamic compressive strength in MPa, UCS_{dry} and $UCS_{sat.}$ are uniaxial compressive strength of the sample (MPa) in oven-dried and fully saturated conditions, respectively, and *LR* is loading rate in kN/s.

In tensile experiments, only static and dynamic tests were performed, so the equations for these data are less well-constrained (Figures 4.38, 4.39). The dynamic tensile strengths of these rocks are also related to the loading rate and static tensile strength (Figure 4.40). These relationships are given as:

$$\sigma_{t-dc-red\ sandstone} = \begin{cases} (-2E-6)LR - BTS_{dry} \\ (-5E-6)LR - BTS_{sat.} \end{cases} \quad (4.10)$$

$$\sigma_{t-dc-buff\ sandstone} = \begin{cases} (-2E-6)LR - BTS_{dry} \\ (-3E-6)LR - BTS_{sat.} \end{cases} \quad (4.11)$$

4.5 Energy absorption in dynamic rock fragmentation

Most past investigations of rock fracture have been performed using quasistatic loads. Recently, however, evaluation of rock fracture and fragmentation under dynamic loading conditions has been performed using the Split Hopkinson Pressure Bar and other similar devices. Thus, Hakalehto, Wu, and Lundberg (as cited by Lundberg 1976) studied fragmentation of unconfined cylindrical rock specimen and energy absorption due to stress wave loading. The aim of this research has been to study the effect of porosity and water content on energy absorption and fragment size distribution in the two different sandstones. In this case, the energy absorbed by the fractured specimens of buff and red sandstone was evaluated from the recorded stress pulses.

In each specimen the incident stress pulse (σ_I) was partly reflected (σ_R) and partly transmitted (σ_T). As a consequence of the stress wave load, the specimens were fragmented, and the fragments were recovered in the box surrounding the ends of the bar and specimen. Recovered materials, as shown in Figures 4.41 and 4.42, confirm that the specimens in dry and saturated conditions were extensively fragmented, and that fragments of dry samples were larger than fragments of saturated samples. For evaluating this issue, the stress wave records obtained with the data acquisition system were analyzed, and based on these stress waves and the following equations, the energy of incident (W_I), transmitted (W_T), and reflected (W_R) stress waves were determined:

$$W_I = (\frac{A_b C_b}{E_b}) \int \sigma_I^2 \, dt \tag{4.12}$$

$$W_R = (\frac{A_b C_b}{E_b}) \int \sigma_R^2 \, dt \tag{4.13}$$

$$W_T = (\frac{A_b C_b}{E_b}) \int \sigma_T^2 \, dt \tag{4.14}$$

where A_b, C_b, and E_b are the bar cross sectional area, sonic velocity of steel bars, and the Young's modulus of the bars, respectively. Based on the Equations of 4.12 to 4.14, the energy absorbed by the specimens to break them is expressed by the following equation:

$$W_L = W_I - (W_R + W_T) \tag{4.15}$$

After each experiment of dynamic compressive testing, all of the rock fragments were collected for sieve analysis. The sieve analysis was done with standard Tyler series sieves varying from 4.76 mm to 0.075 mm (ASTM C136/C136M-14). Figures 4.43 and 4.44 summarize the sieve analysis for the fragments obtained after dynamic compressive tests for dry and fully saturated samples. The size of fragments of saturated samples was found to be consistently lower than the size of fragments from dry samples. In addition, the fragment size increased with increasing dynamic strength in red sandstone in comparison with buff sandstone. In dynamic compressive breakage, the stress was distributed over the entire specimen. In contrast, static breakage was mostly localized in shear or tensile failure planes or cones, and for identical levels of applied dynamic stress, the stronger rocks yielded larger fragments. Water content in the same rock with the same conditions reduced the rock strength and fragments size.

Fragment size distribution and energy absorption in these types of sandstone were evaluated. As can be seen in Figure 4.45 the energy components, incident wave (W-I), reflected wave (W-R), transmitted wave (W-T), and the energy absorbed (W-L) by saturated rock were lower than for dry rock. As shown in Figure 4.46 and 4.47, the

energy absorbed by saturated specimens (W-L) is about 18 to 19% less than dry rock specimens in red and buff sandstone, respectively. Therefore fine rock fragments were obtained with lower energy when saturated.

Table 4.1 Ratio of dynamic and static compressive strength of selected rock

Rock types (reference)	$\sigma_{c\ (dynamic)}$ (MPa)	Strain rate	$\sigma_{c\ (dynamic)}/\sigma_{c\ (static)}$
Gray Basalt (Kumar, 1968)	190	1300	2.2
Grey Granite (Kumar, 1968)	200	1300	2.4
Bohus Granite (Lundberg, 1976)	283	n.a.	1.8
Solenhofen Lst (Lundberg, 1976)	342	n.a.	1.3
Basalt (Buchar & Bilek, 1981)	520	1000	3.0
Granite (Buchar & Bilek, 1981)	274	1000	3.7
Limestone (Buchar & Bilek, 1981)	188	1000	3.9
Graywacke (Buchar & Bilek, 1981)	203	1000	4.0

Modified from Prasad (2000)

Table 4.2 Dynamic compressive strength from measurements of dry and saturated red sandstones

Sample condition	Sample No.	Length	Diameter	Loading rate	Dynamic strength	Max. Strain rate	Failure strain	Young's modulus
		mm	mm	MN/s	MPa	1/s	mm/mm	GPa
Sat.	RSS5	57.19	31.53	9853	218	282	0.0016	252
	RSS8	57.37	31.51	9128	201	231	0.0011	252
	RSS12	65.79	31.50	10048	222	228	0.0015	244
	RSS19	66.00	31.46	10780	220	270	0.0014	263
	RSS25	65.48	31.46	10526	207	285	0.0015	256
	RSS26	65.79	31.47	10098	216	251	0.0010	254
	RSS27	65.91	31.48	11080	219	249	0.0013	251
	RSS28	65.66	31.48	9439	234	223	0.0010	261
Dry	RSS2	56.78	31.53	14395	245	253	0.0015	288
	RSS3	57.16	31.50	16095	286	273	0.0020	275
	RSS4	57.43	31.52	15164	240	280	0.0021	271
	RSS16	65.54	31.47	15118	240	227	0.0014	283
	RSS17	65.76	31.45	17689	285	273	0.0015	286
	RSS20	65.53	31.48	18167	289	294	0.0019	294
	RSS40	65.14	31.46	16270	273	264	0.0016	277
	RSS41	65.11	31.44	16365	266	258	0.0016	288
	RSS43	65.80	31.45	16066	255	232	0.0014	278
	RSS9	66.00	31.52	17305	280	290	0.0020	264
	RSS10	65.79	31.52	15357	272	297	0.0018	271

Table 4.3 Experimental results on fast loading of red sandstone specimens

Sample condition	Sample No.	Loading Rate (kN/s)	Max. Stress (MPa)	Young Modulus (GPa)
Dry	RSS30	257.620	228	23.95
	RSS18	247.416	217	23.59
	RSS23	236.659	211	22.85
	RSS22	247.281	217	23.71
	RSS6	251.083	212	21.94
	RSS7	252.788	232	23.55
Saturated	RSS14	251.127	170	21.20
	RSS42	244.454	176	21.38
	RSS24	262.634	175	23.06
	RSS37	250.973	166	21.29
	RSS38	263.227	160	20.57
	RSS39	255.191	177	22.57

Table 4.4 Dynamic tensile strength of dry and saturated red sandstone

Sample Situation	Sample No.	Thickness	Diameter	Dynamic strength	Max Strain rate	Failure Strain	Loading rate
		mm	mm	MPa	1/s	mm/mm	MN/s
Dry	RSBT3	20.5	53.8	32.59	519.80	0.009	2337.59
	RSBT5	21.0	53.8	34.56	562.74	0.010	2690.13
	RSBT10	20.3	53.8	30.14	454.84	0.009	1961.44
	RSBT11	20.6	53.6	26.28	487.97	0.009	2204.72
	RSBT12	20.7	53.8	32.17	597.15	0.013	2436.24
	RSBT13	21.3	53.7	28.41	619.97	0.017	2208.65
	RSBT16	20.7	53.8	24.49	811.45	0.017	1768.74
	RSBT18	20.8	53.9	33.28	550.06	0.013	2740.90
	RSBT19	20.6	53.9	31.90	541.96	0.010	2366.77
Saturated	RSBT23	20.9	53.7	25.04	466.45	0.010	1769.75
	RSBT28	22.7	53.5	25.32	518.60	0.010	2184.28
	RSBT29	21.4	53.9	24.19	593.89	0.013	1907.63
	RSBT30	20.6	53.8	18.88	635.08	0.014	1420.00
	RSBT31	21.2	53.8	24.62	477.16	0.008	1722.60
	RSBT32	21.0	53.8	25.76	531.48	0.009	1718.87
	RSBT33	21.2	53.8	24.60	554.29	0.010	1964.51
	RSBT34	21.5	53.8	24.83	534.43	0.010	1966.54
	RSBT35	21.3	53.8	26.42	502.03	0.008	1985.43
	RSBT36	21.0	53.8	23.96	537.74	0.011	1806.39

Table 4.5 Dynamic compressive strength from measurements of dry and saturated buff sandstones

Sample condition	Sample No.	Length	Diameter	Loading rate	Dynamic strength	Max. Strain rate	Failure strain	Young's modulus
		mm	mm	MN/sec.	MPa	1/sec.	mm/mm	GPa
Sat.	BSS3	55.91	31.41	7345.91	124	401.05	0.0014	176
	BSS5	55.89	31.38	7171.34	123	382.56	0.0012	173
	BSS36	65.72	31.33	7836.49	123	363.14	0.0010	195
	BSS20	66.19	31.29	7320.94	128	301.20	0.0013	188
	BSS26	64.90	31.28	7098.27	111	273.20	0.0015	185
	BSS35	66.34	31.37	7695.49	126	315.59	0.0014	181
	BSS23	65.81	31.32	7445.47	122	307.12	0.0012	187
	BSS1	56.34	31.41	8055.60	130	324.34	0.0014	171
	BSS8	66.14	31.31	7815.03	130	345.74	0.0017	206
Dry	BSS4	56.05	31.36	8697.65	144	361.26	0.0016	201
	BSS9	66.07	31.39	8527.36	142	310.62	0.0012	202
	BSS11	66.26	31.33	9074.85	161	318.93	0.0021	195
	BSS16	66.43	31.28	9131.76	164	333.32	0.0013	208
	BSS21	66.11	31.28	8719.75	152	298.78	0.0010	202
	BSS24	66.31	31.28	8483.53	141	281.77	0.0016	212

Table 4.6 Buff sandstone strength in dry and saturated condition in fast loading

Sample condition	Sample No.	Loading Rate (kN/s)	Max. Stress (MPa)	Young's Modulus (GPa)
Dry	BSS14	231.545	87	12.22
	BSS19	214.968	84	11.92
	BSS38	210.821	85	12.30
	BSS2	209.629	87	11.98
Saturate	BSS28	213.148	69	11.67
	BSS39	206.432	64	11.13
	BSS31	212.778	67	11.46
	BSS6	218.663	70	11.76

Table 4.7 Dynamic tensile strength of buff sandstone in dry and saturated conditions

Sample Situation	Sample No.	Thickness	Diameter	Dynamic Strength	Max Strain Rate	Failure Strain	Loading Rate
		mm	mm	MPa	1/s	mm/mm	MN/s
Dry	BSBT3	21.1	53.8	9.64	652.33	0.018	786.27
	BSBT10	20.0	53.8	8.88	590.56	0.014	531.56
	BSBT11	23.7	53.8	8.60	468.52	0.013	667.88
	BSBT12	20.5	53.8	8.99	629.51	0.016	652.87
	BSBT13	21.4	53.8	9.52	568.46	0.016	661.78
	BSBT20	20.2	53.7	8.02	618.67	0.015	536.78
	BSBT24	20.8	53.8	9.09	607.47	0.017	701.41
Saturated	BSBT2	20.9	53.8	6.03	531.88	0.016	395.86
	BSBT4	21.0	53.8	7.72	645.80	0.018	618.17
	BSBT14	21.0	53.7	7.60	537.66	0.014	489.67
	BSBT15	20.8	53.7	6.84	659.68	0.017	312.67
	BSBT16	20.2	53.8	6.32	705.70	0.020	435.06
	BSBT17	21.0	53.8	7.59	656.42	0.017	479.31
	BSBT18	20.4	53.8	7.06	689.88	0.021	549.96

Table 4.8 Loading rate effect on DIF in buff and red sandstone

Rock type	Sample condition		Experiment type	Loading rate (kN/s)	Rock strength (MPa)	DIF
Red sandstone	Compressive test	Dry	Static	1.3	195.2	1.0
			Fast Loading	248	219	1.12
			Dynamic	16E6	264	1.36
	Tensile test		Static	0.08	26.66	1.0
			Dynamic	2.3E6	32.44	1.22
	Compressive test	Saturated	Static	1.3	153.6	1.0
			Fast Loading	254	171	1.11
			Dynamic	10E6	215	1.41
	Tensile test		Static	0.07	16.17	1.0
			Dynamic	1.8E6	24.97	1.54
Buff Sandstone	Compressive test	Dry	Static	1.3	74.8	1.0
			Fast Loading	216	86.0	1.15
			Dynamic	8.7E6	149	2.01
	Tensile test		Static	0.06	8.01	1.0
			Dynamic	0.65E6	8.96	1.12
	Compressive test	Saturated	Static	1.3	62.3	1.0
			Fast Loading	212	67.6	1.08
			Dynamic	7.4E6	122	1.99
	Tensile test		Static	0.06	5.34	1.0
			Dynamic	0.47E6	6.89	1.29

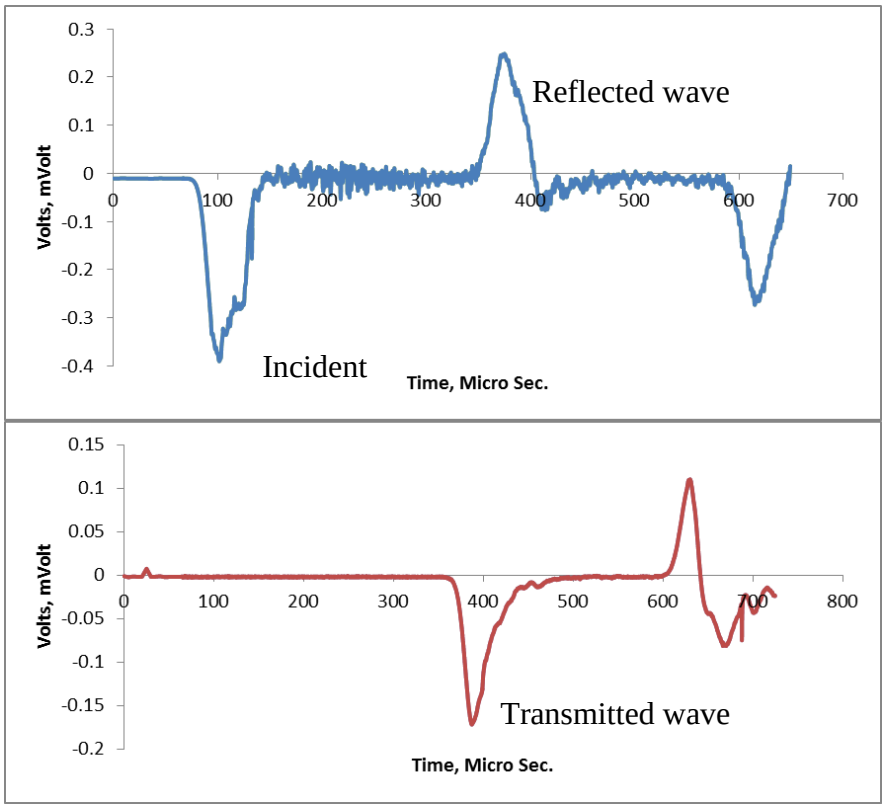

Figure 4.1 Recorded strain pulses acquired for red sandstone samples (RSS10).

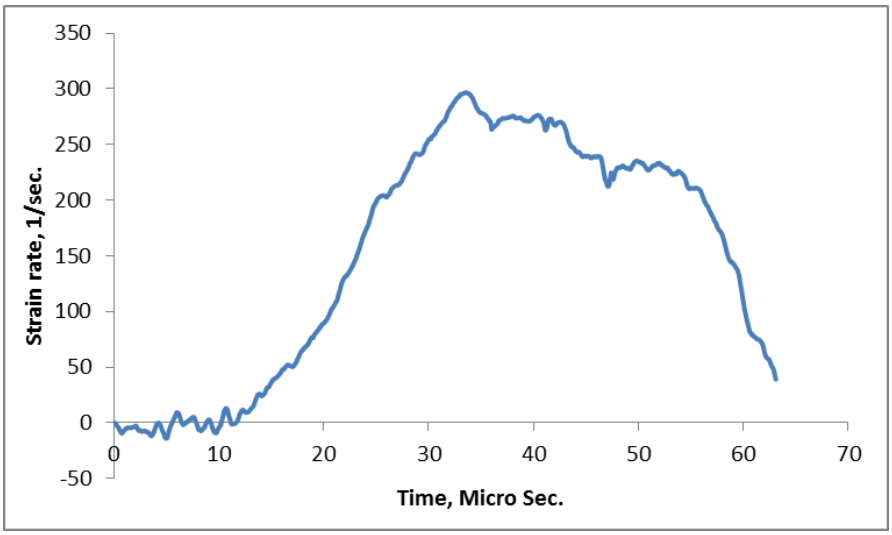

Figure 4.2 Strain rate (sec^{-1}) variation with time for sample RSS10.

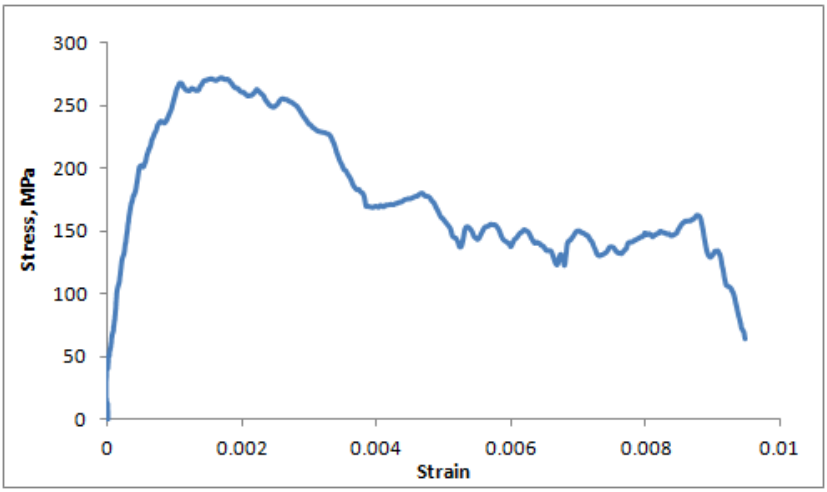

Figure 4.3 Dynamic stress strain behavior of red sandstone sample (RSS10).

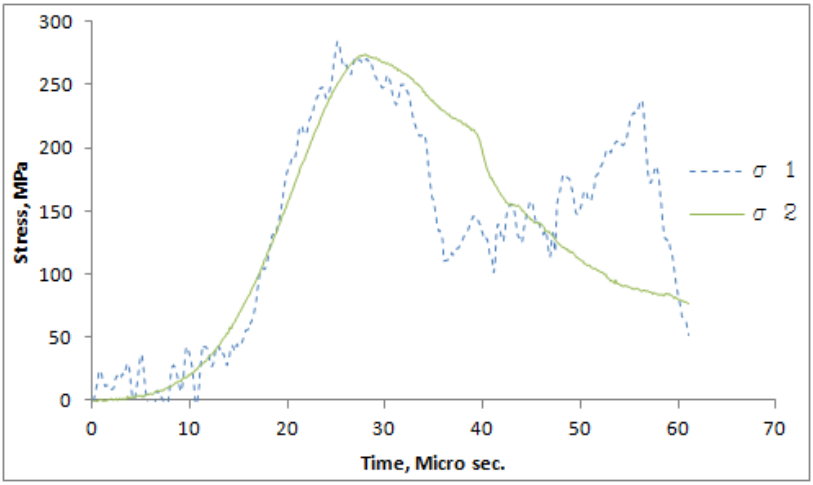

Figure 4.4 Variation of stress at interface versus time for sample RSS10 (σ1 is the incident bar-sample interface stress and σ 2 is the sample-transmitted bar interface stress).

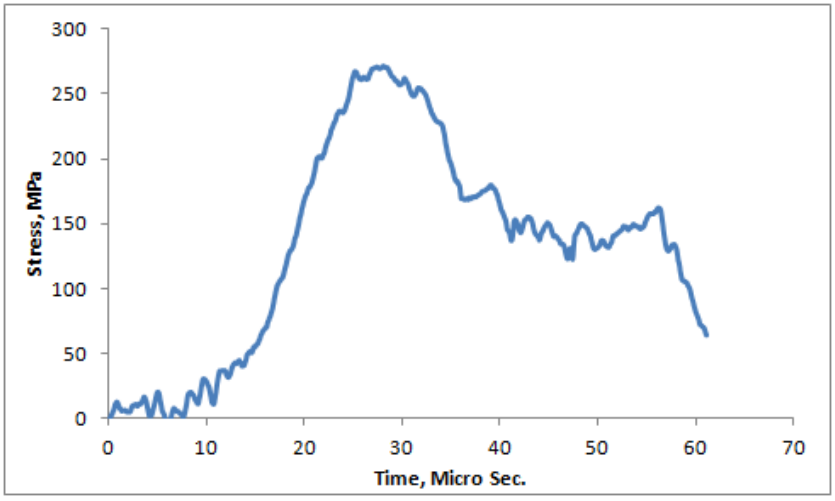

Figure 4.5 Variation of average stress in the sample vs. time for RSS10.

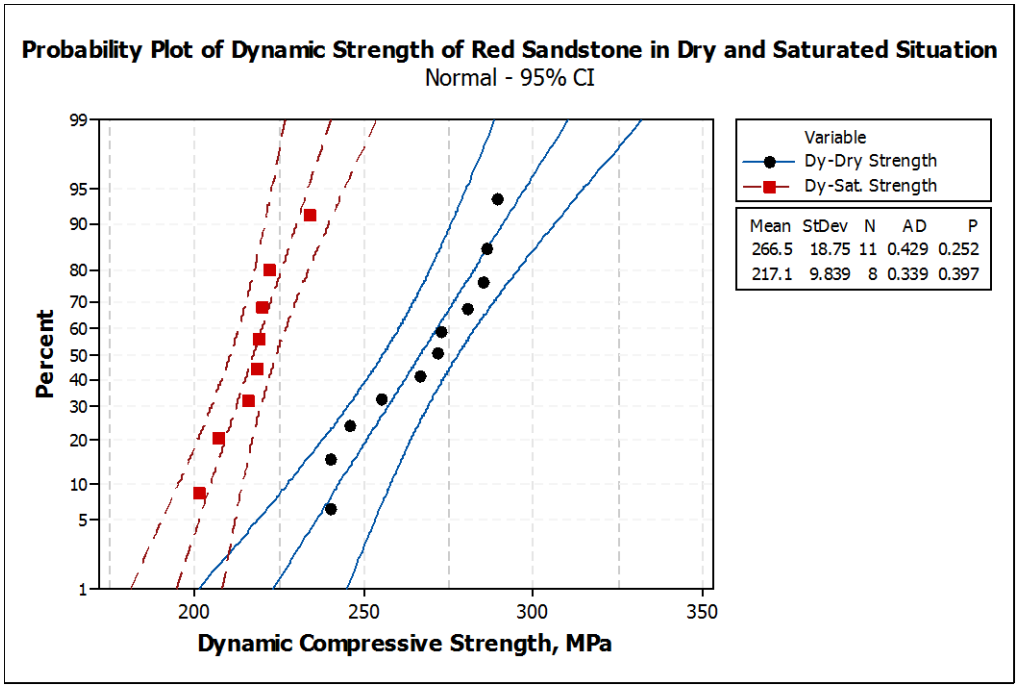

Figure 4.6 Variation of dynamic strength of dry and saturated red sandstone.

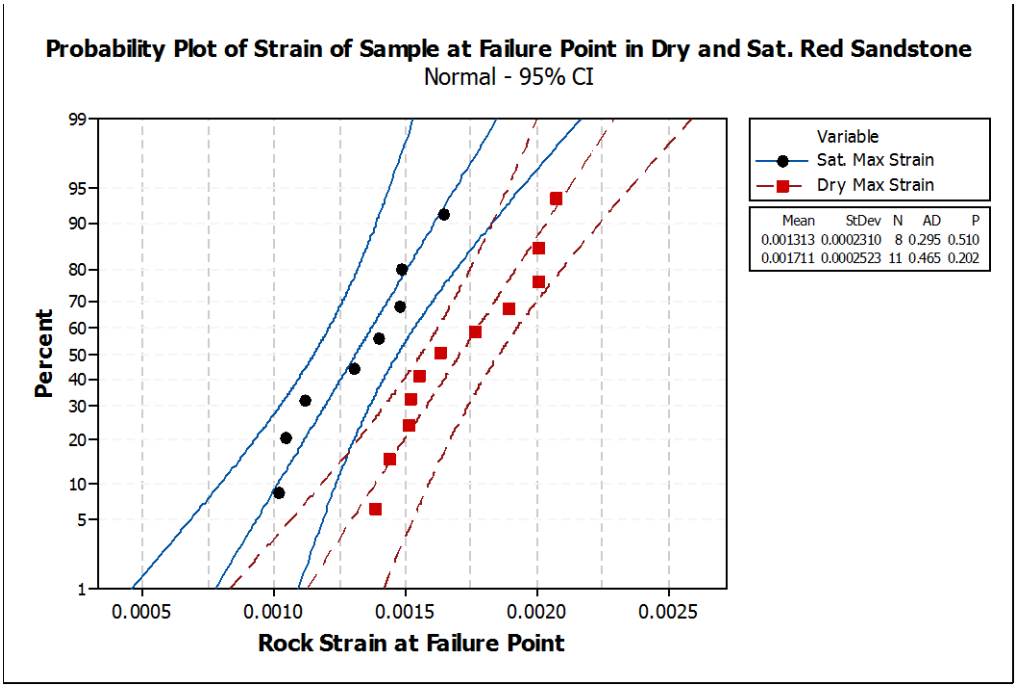

Figure 4.7 Rock specimens' strain at failure points for dry and saturated red sandstones.

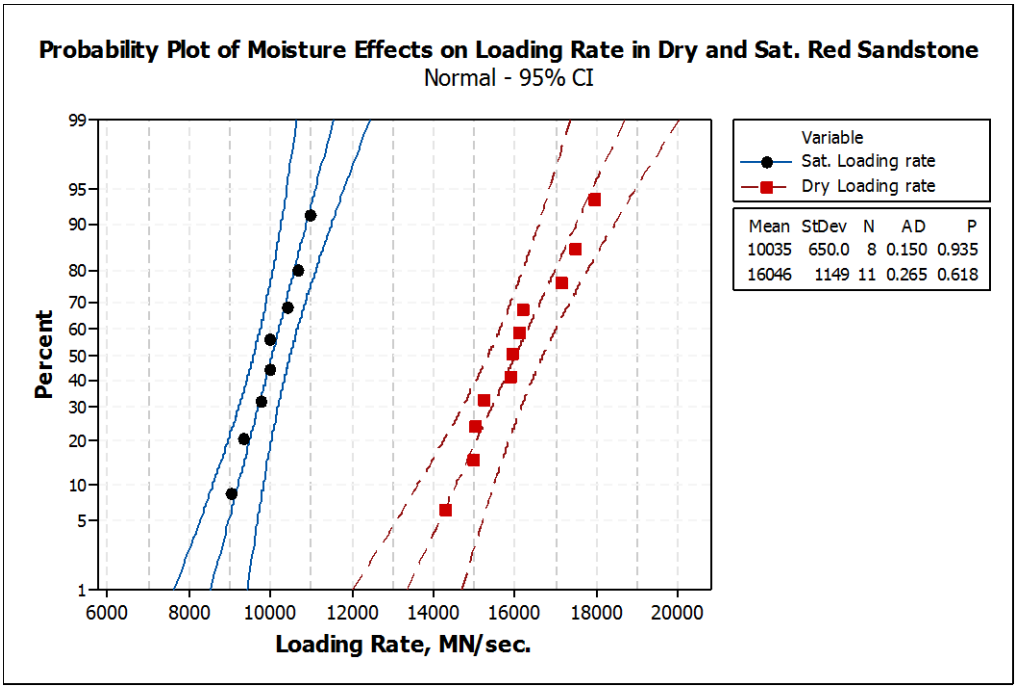

Figure 4.8 Moisture effect on loading rate during dynamic compressive test of red sandstone by SHPB.

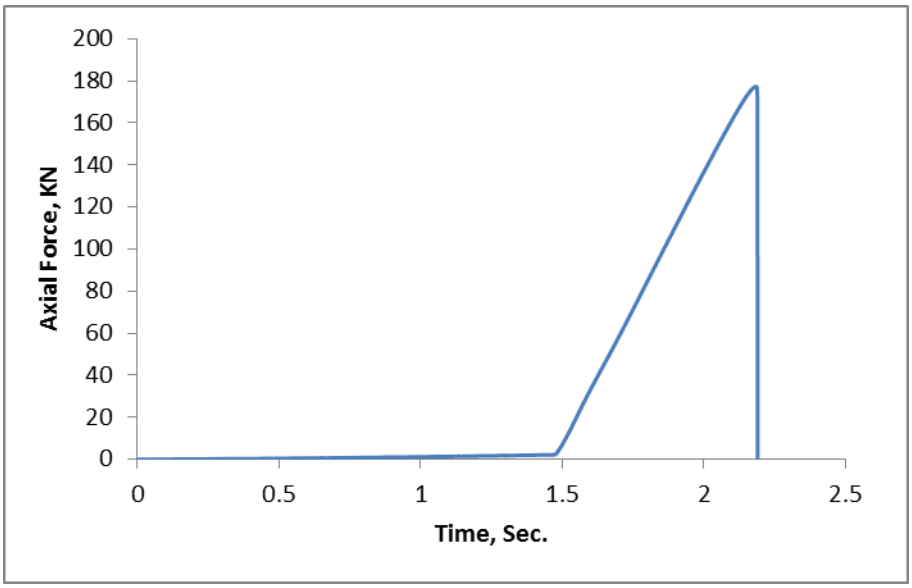

Figure 4.9 Loading condition in fast loading tests (RSS30).

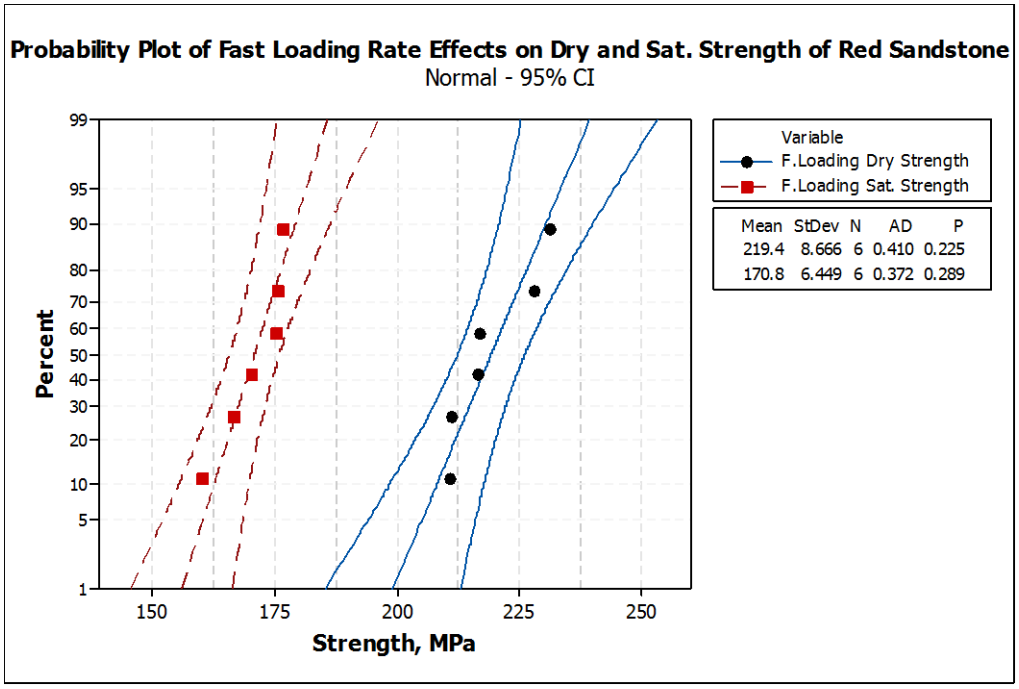

Figure 4.10 Red sandstone compressive strength under fast loading condition.

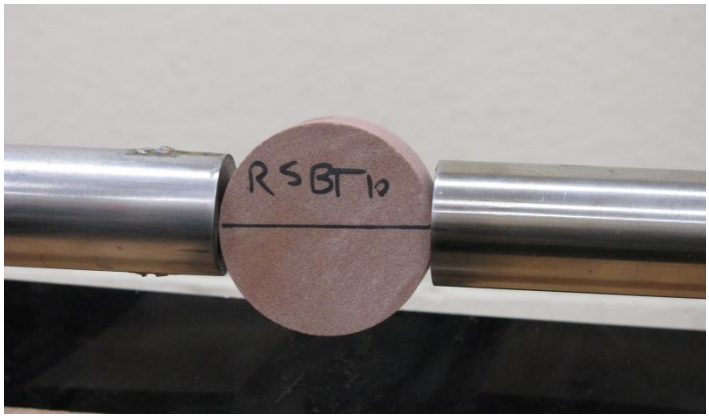

Figure 4.11Dynamic tensile strength test by SHPB.

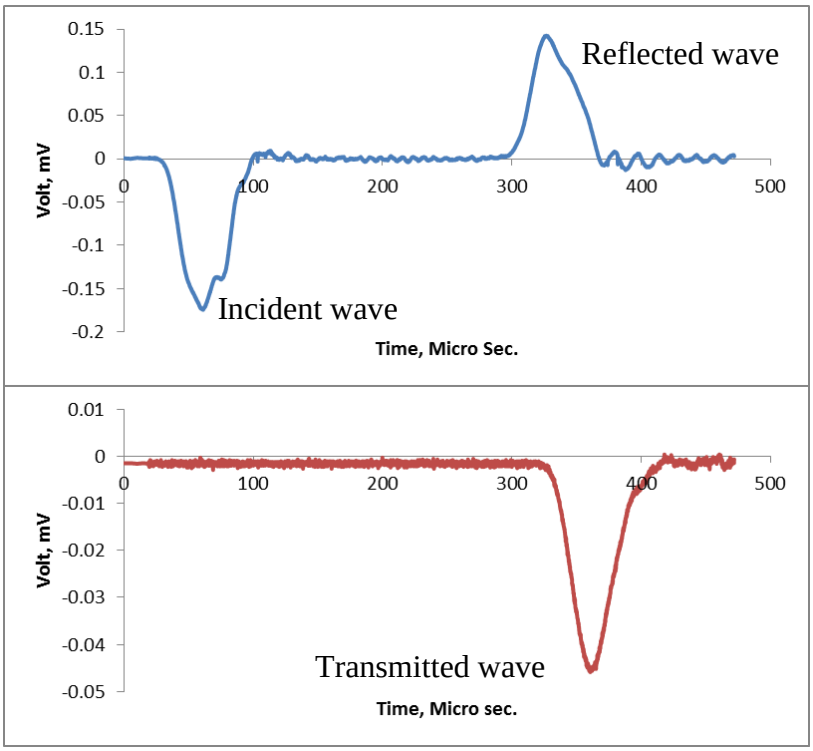

Figure 4.12 Recorded strain pulses acquired for red sandstone samples (RSBT19).

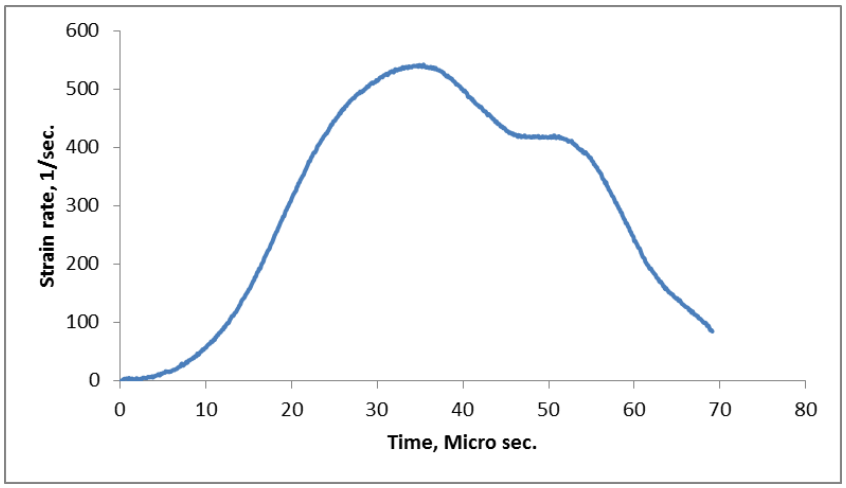

Figure 4.13 Strain rate (sec.$^{-1}$) variation with time for sample RSBT19.

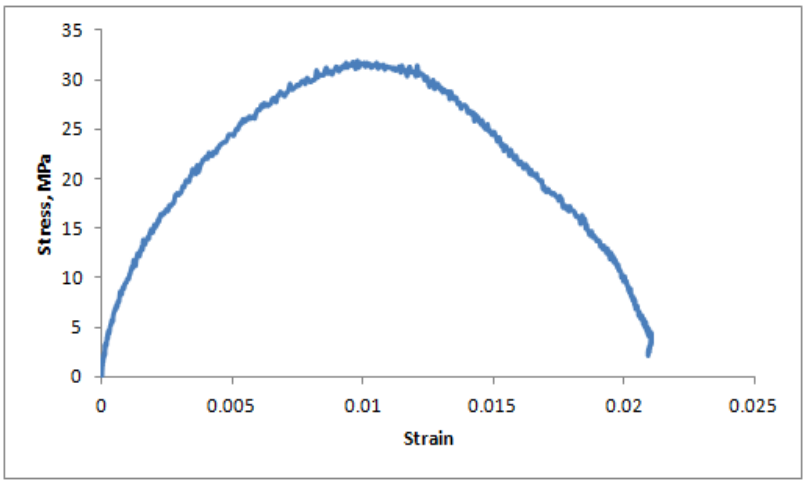

Figure 4.14 Stress-strain curve of dynamic tensile strength of red sandstone (RSBT19).

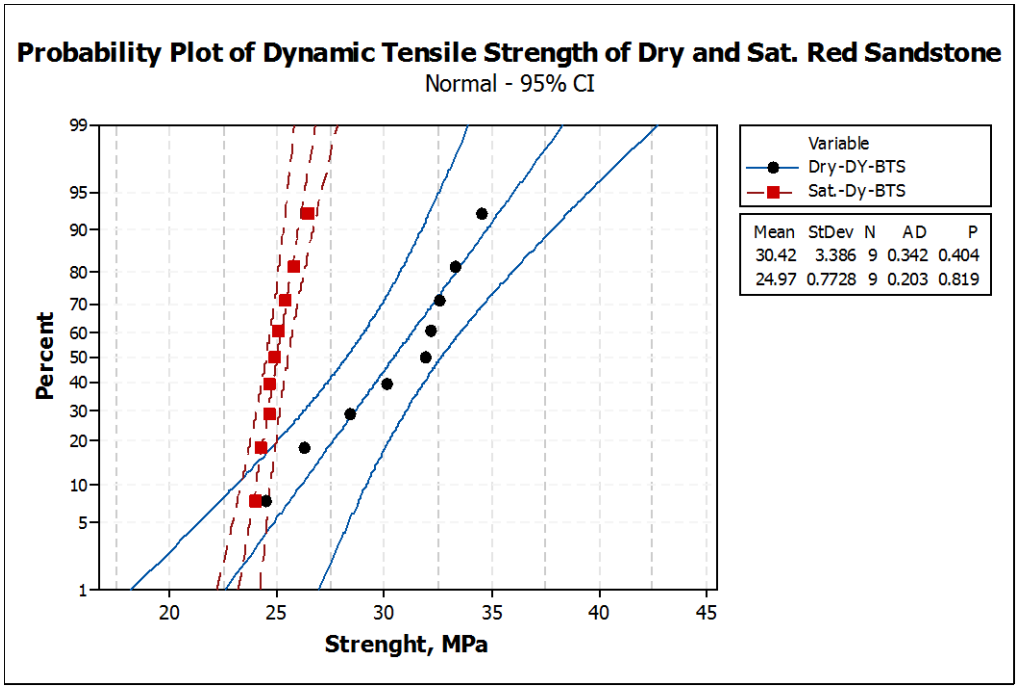

Figure 4.15 Summary results of red sandstone dynamic tensile strength.

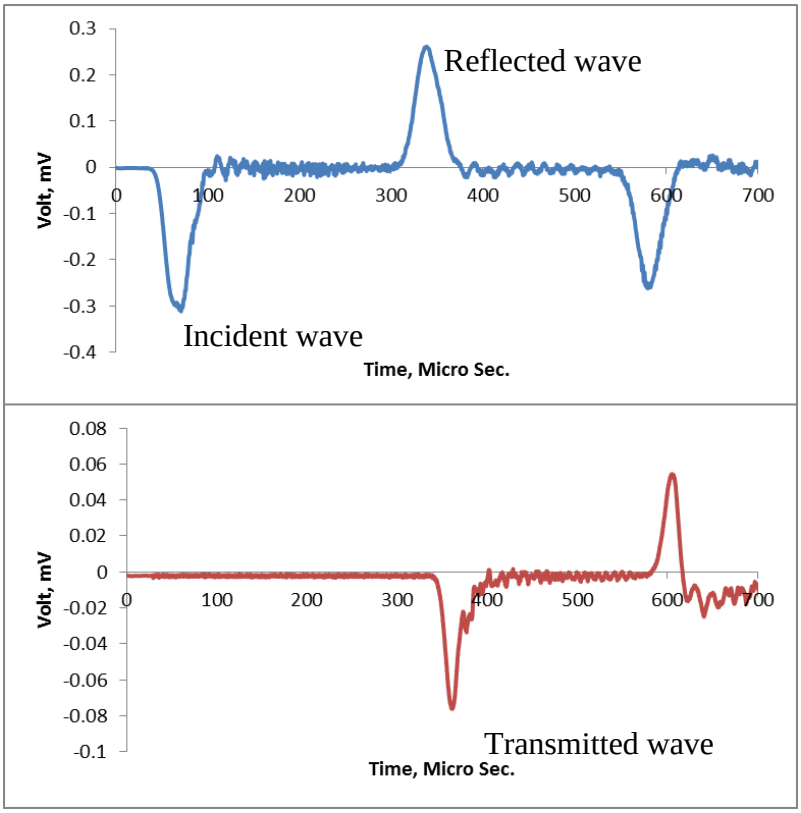

Figure 4.16 Recorded strain pulses acquired for buff sandstone samples (BSS8).

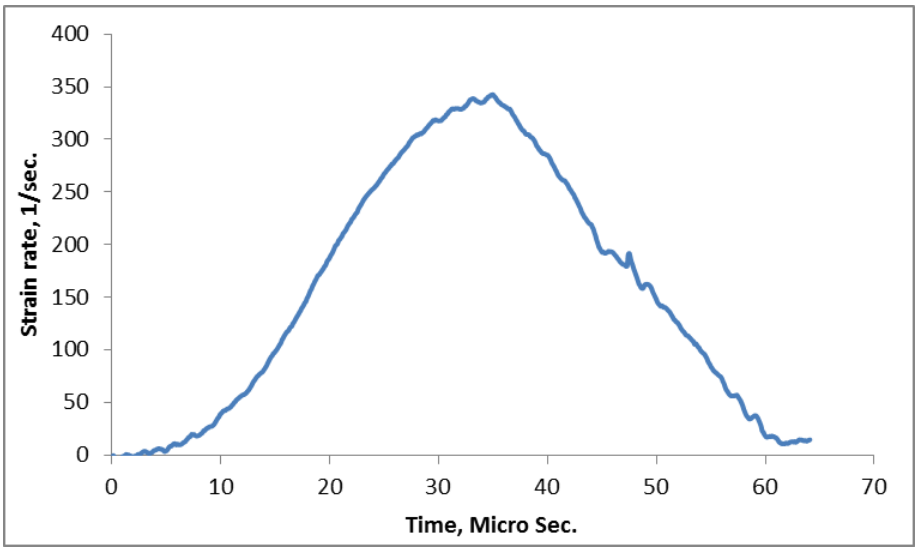

Figure 4.17 Strain rate (sec^{-1}) variation with time for sample BSS8.

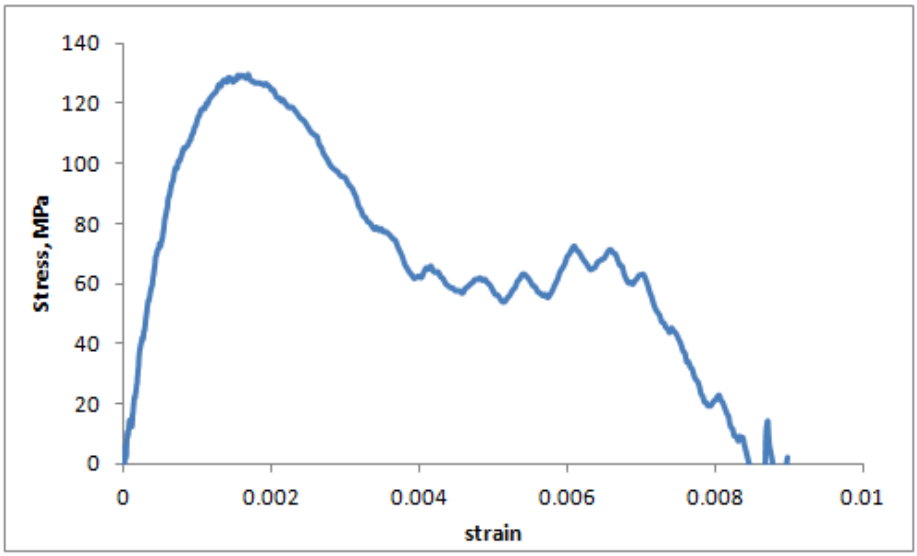

Figure 4.18 Dynamic stress strain behavior of buff sandstone sample (BSS8).

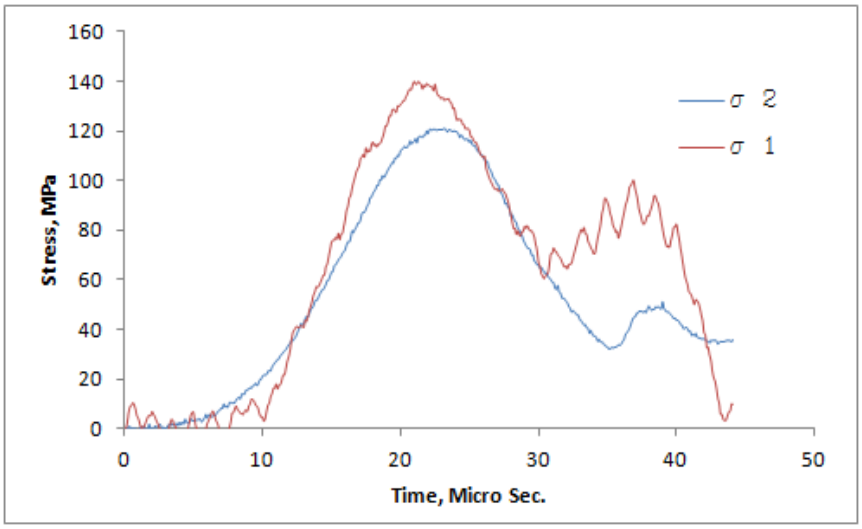

Figure 4.19 Variation of stress at interface versus time for sample BSS8 (σ1 is the incident bar-sample interface stress and σ2 is the sample-transmitted bar interface stress).

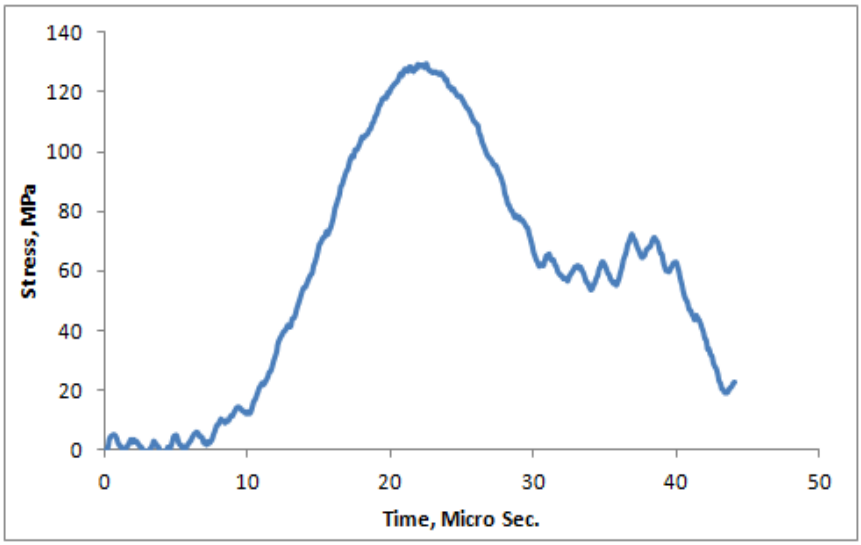

Figure 4.20 Variation of average stress in the sample vs. time for BSS8.

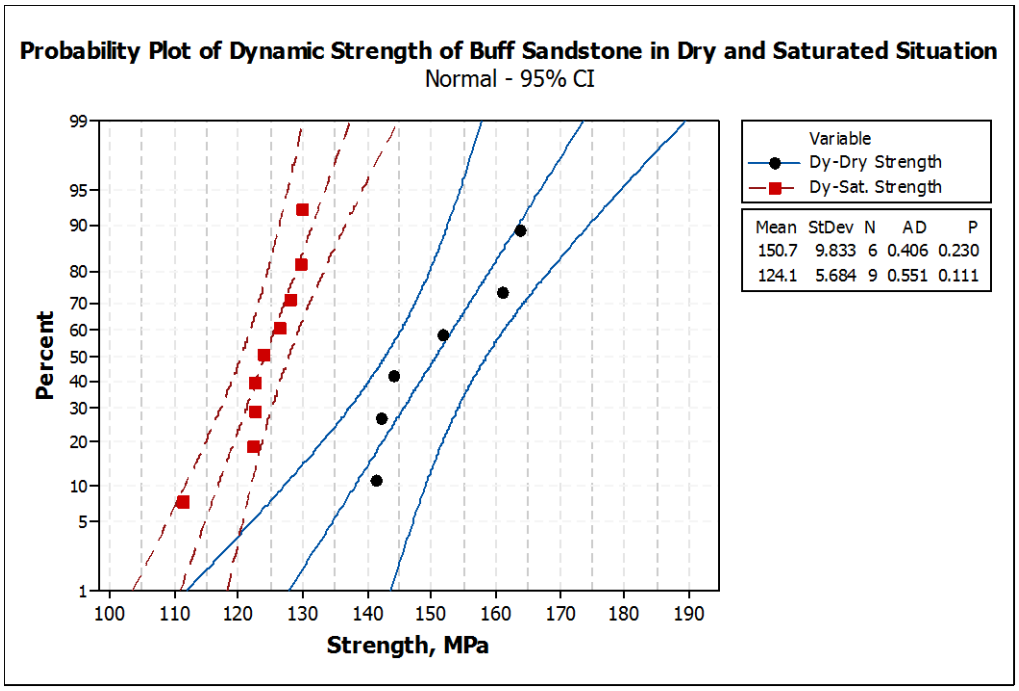

Figure 4.21 Dynamic compressive strength variation of buff sandstone in dry and saturated condition.

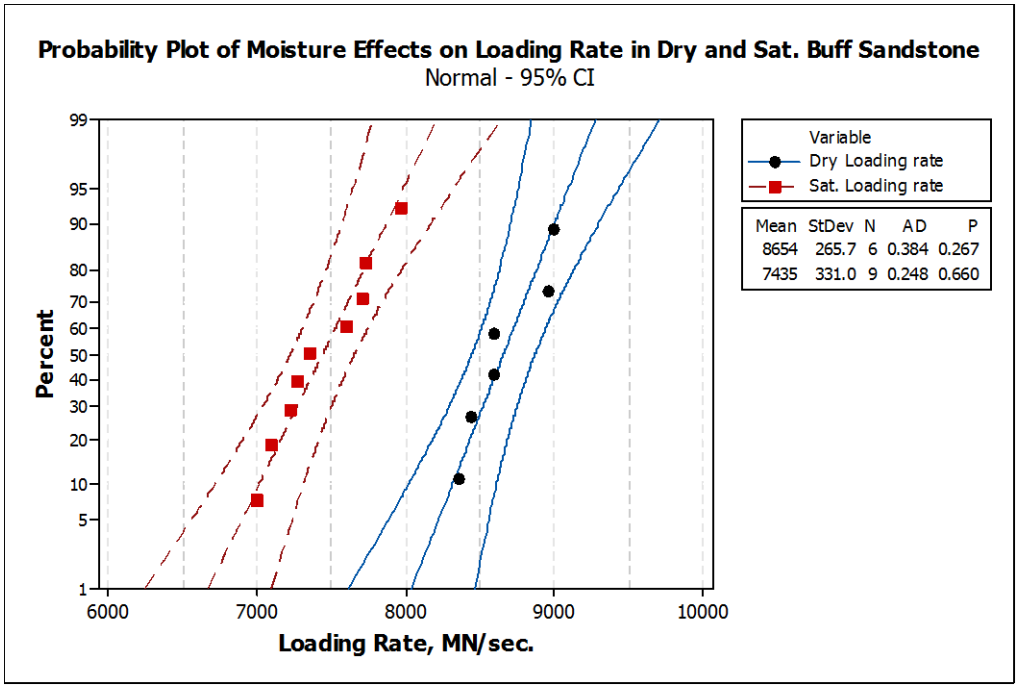

Figure 4.22 Moisture effect on loading rate during dynamic compressive test of buff sandstone by SHPB.

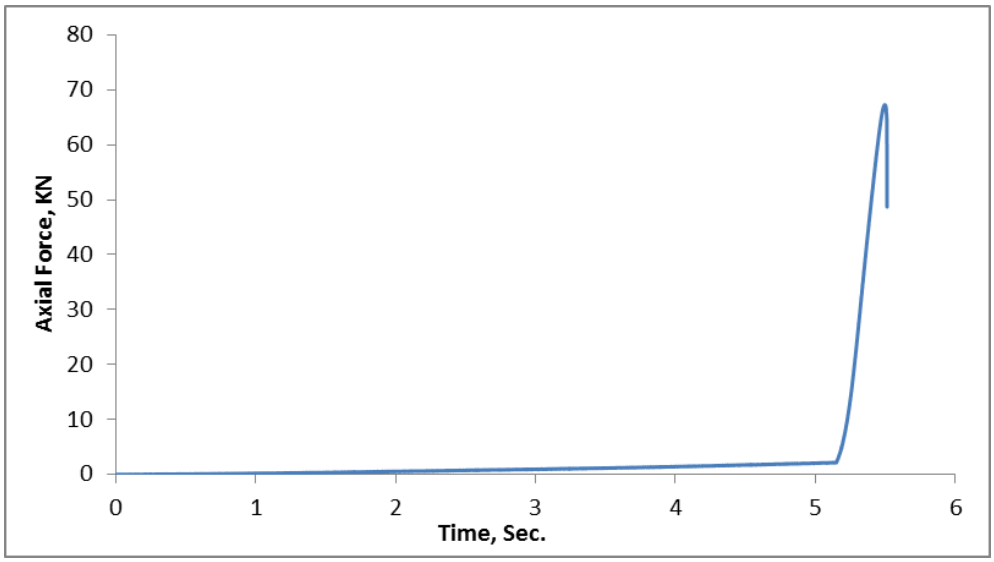

Figure 4.23 Loading rate in fast loading experiment on buff sandstone (BSS14).

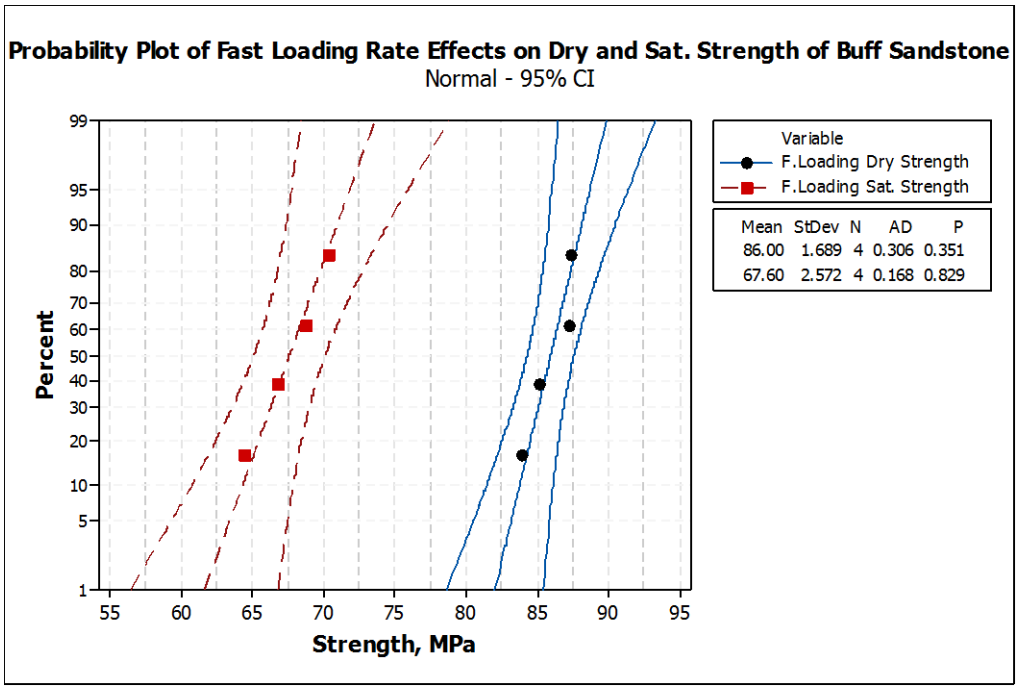

Figure 4.24 Moisture effect on buff sandstone strength under fast loading condition.

Figure 4.25 Buff sandstone disc after dynamic tension test by SHPB.

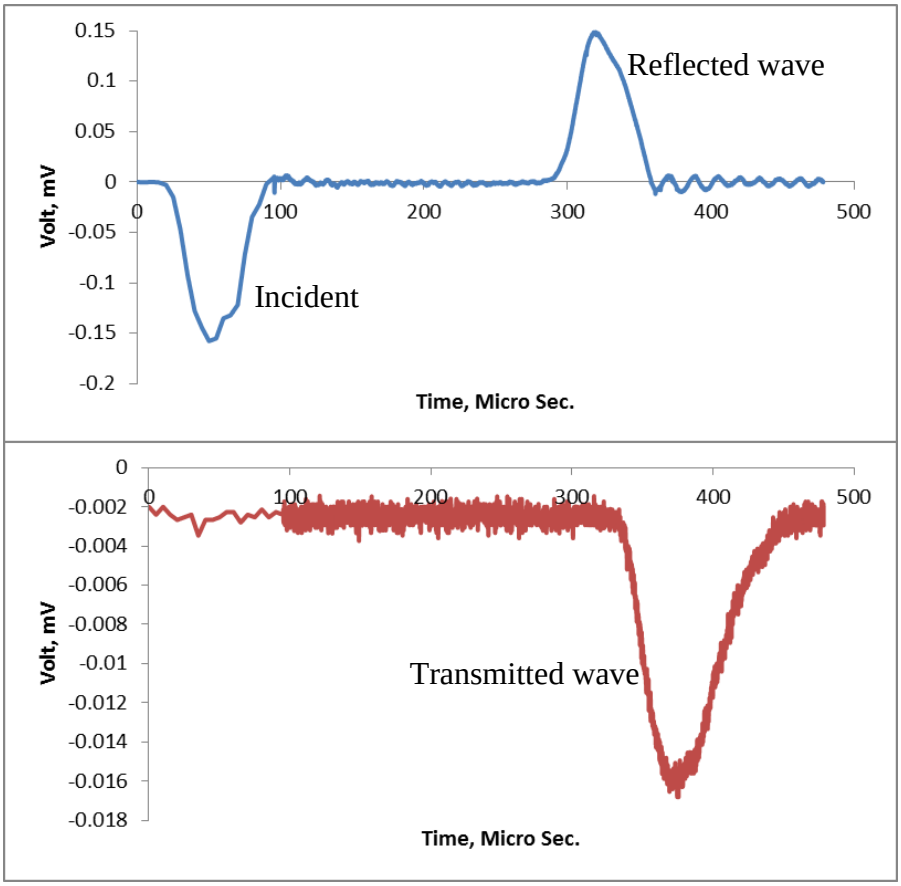

Figure 4.26 Recorded strain pulses acquired for buff sandstone samples (BSBT13).

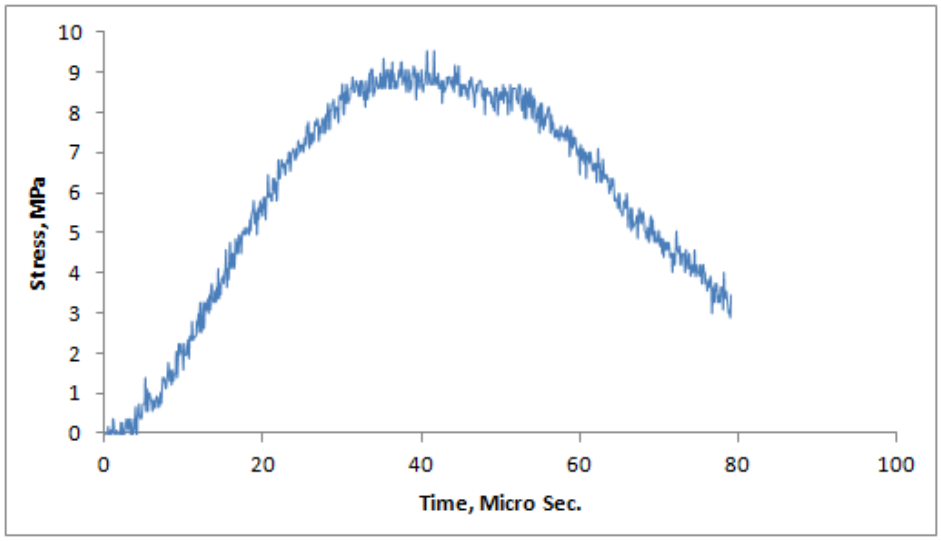

Figure 4.27 Dynamic stress strain behavior of buff sandstone sample (BSBT13).

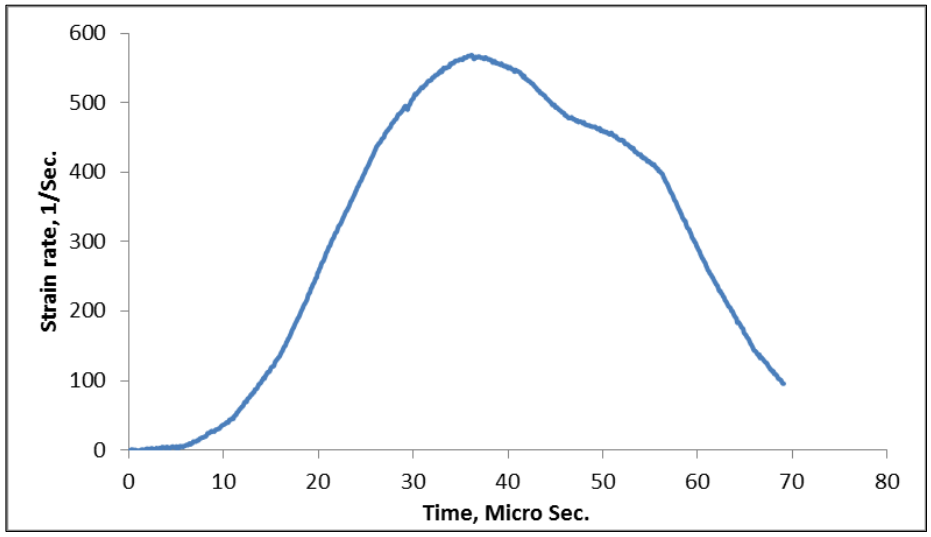

Figure 4.28 Strain rate (sec^{-1}) variation with time for sample BSBT13.

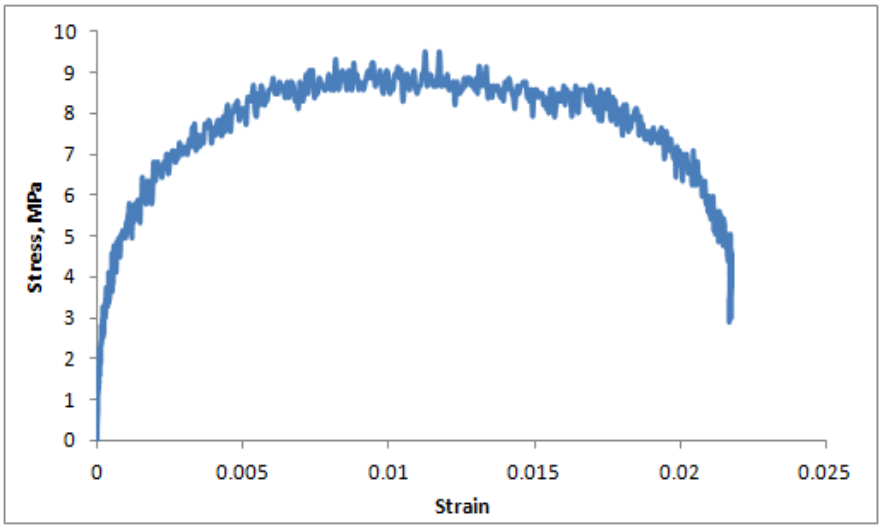

Figure 4.29 Dynamic stress strain behavior of buff sandstone sample (BSBT13).

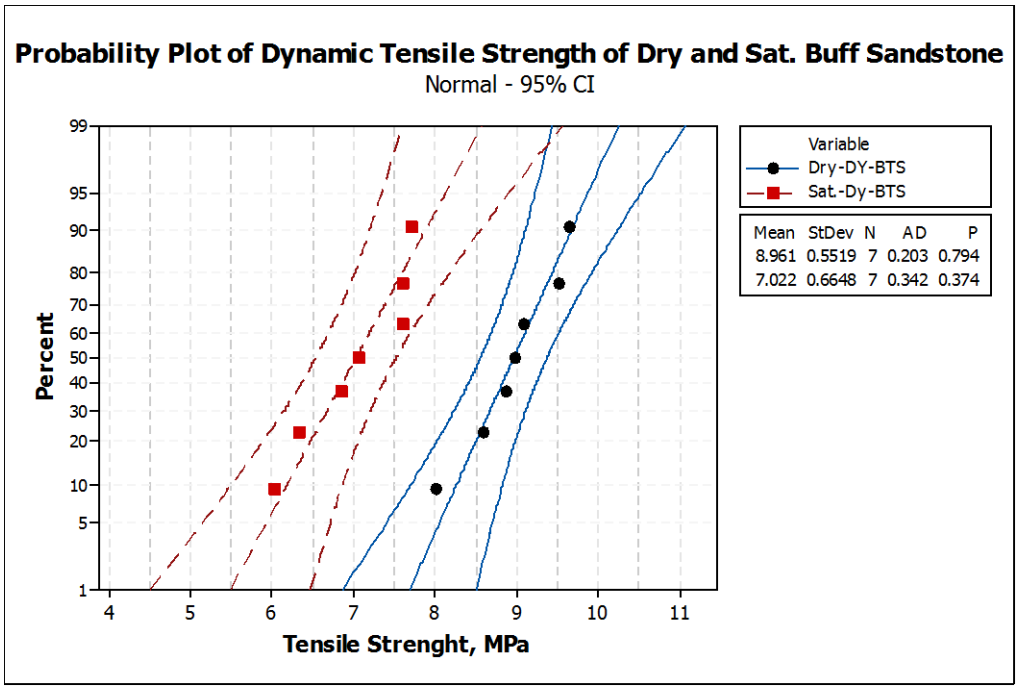

Figure 4.30 Moisture effect on dynamic tensile strength of buff sandstone.

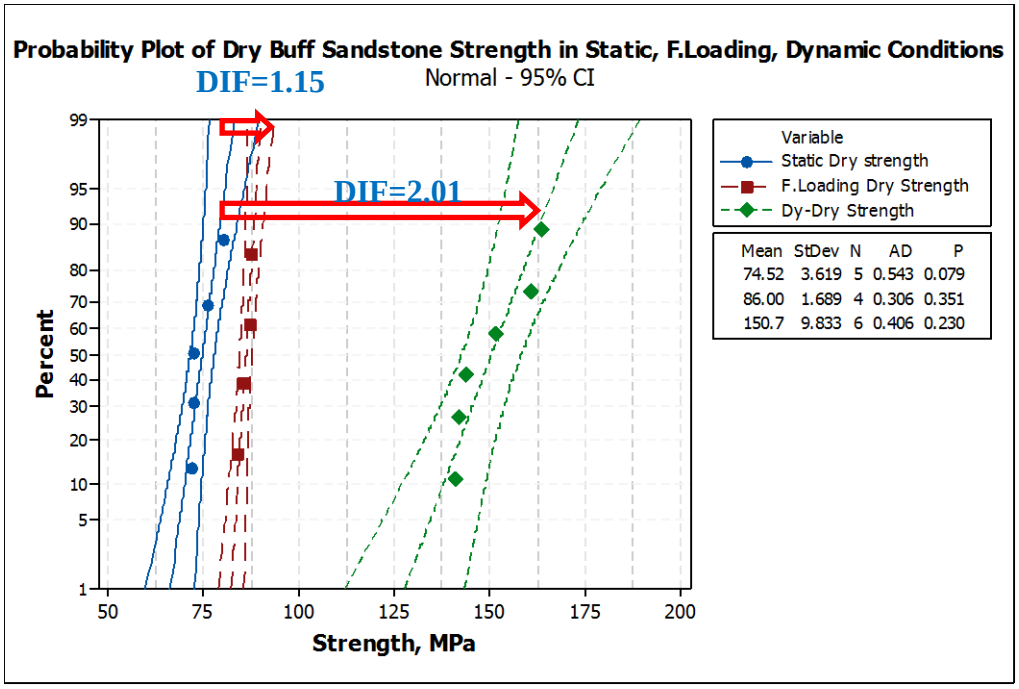

Figure 4.31 Loading rate effects on compressive strength of dry buff sandstone.

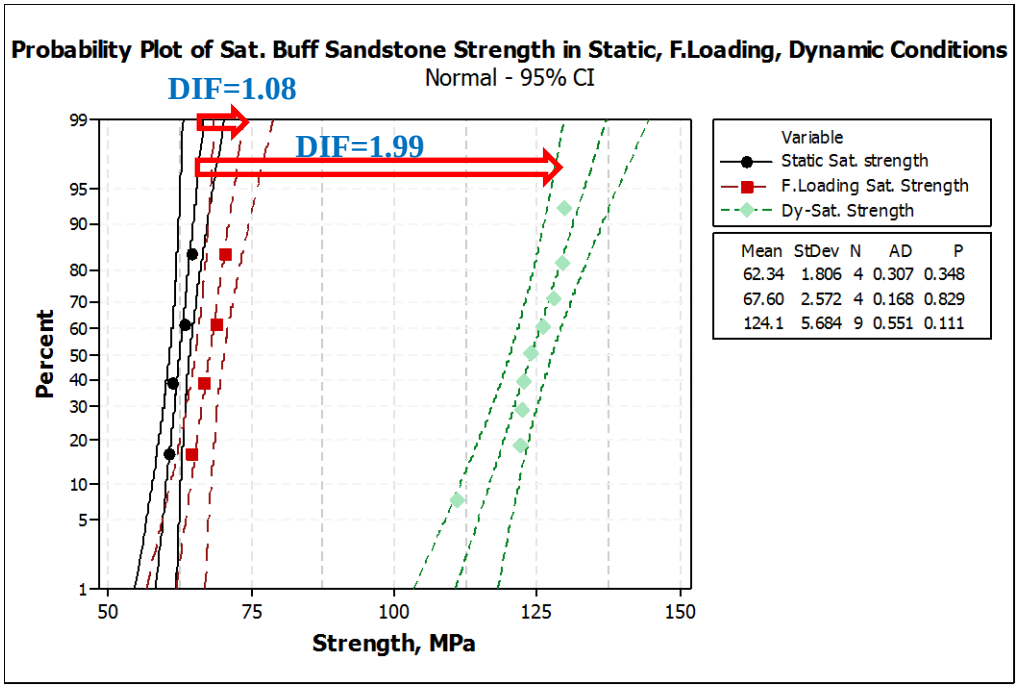

Figure 4.32 Loading rate effects on compressive strength of saturated buff sandstone.

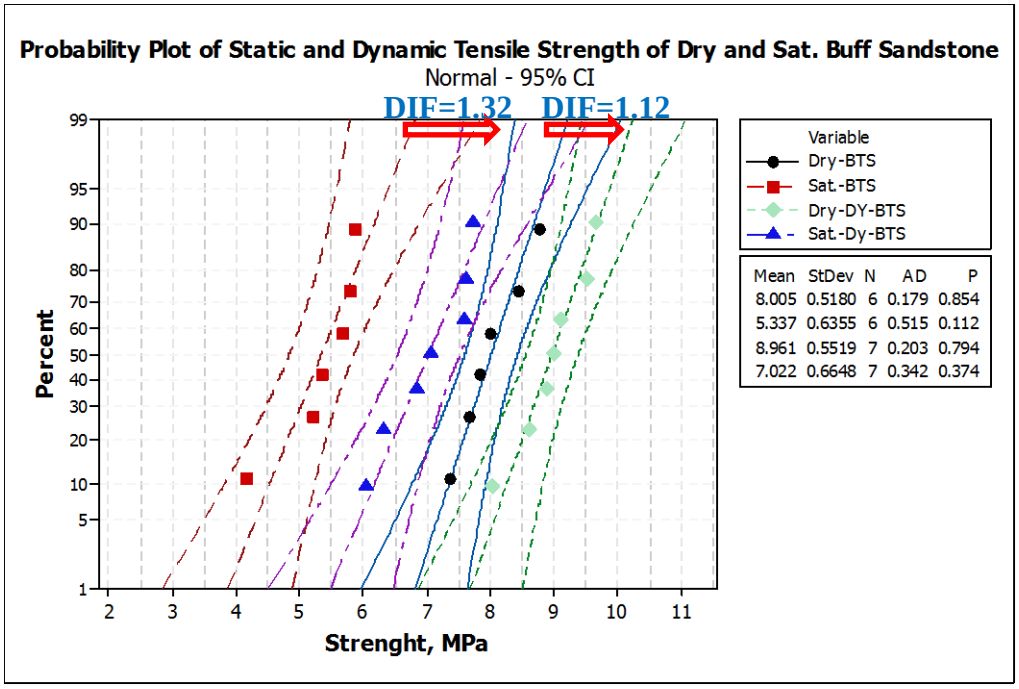

Figure 4.33 Loading rate effects on tensile strength of dry and saturated buff sandstone.

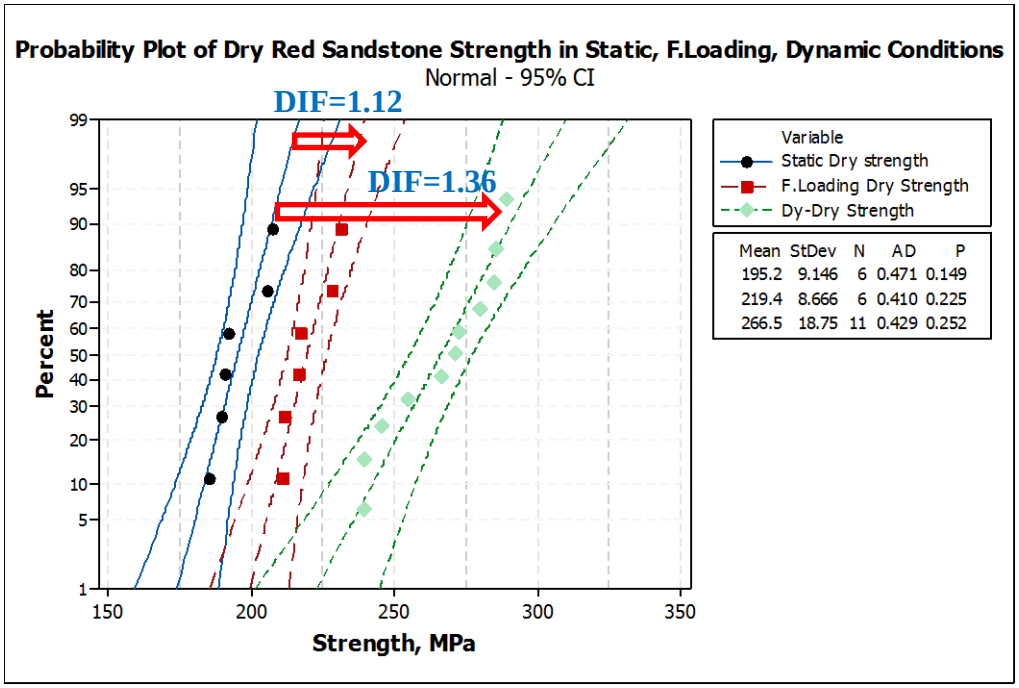

Figure 4.34 Loading rate effects on compressive strength of dry red sandstone.

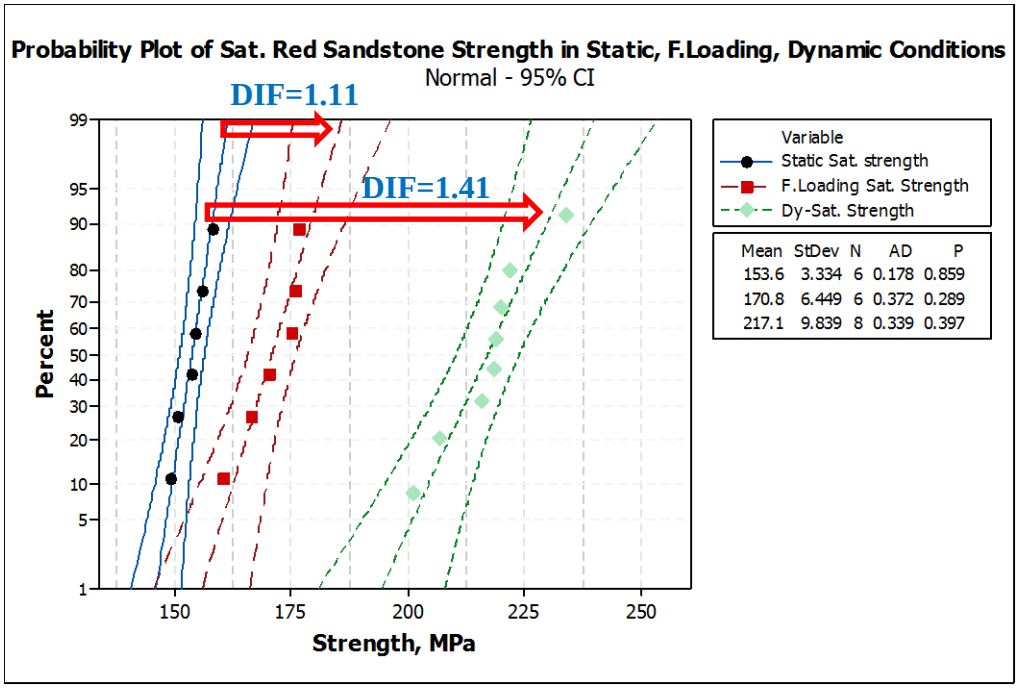

Figure 4.35 Loading rate effects on compressive strength of saturated red sandstone.

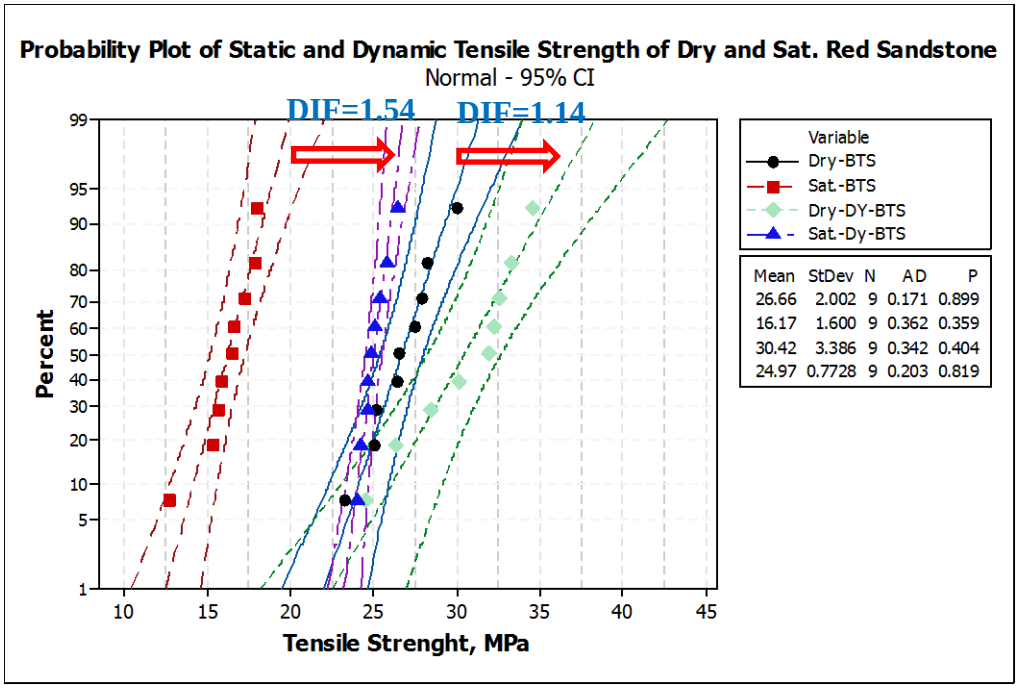

Figure 4.36 Loading rate effects on tensile strength of dry and saturated red sandstone.

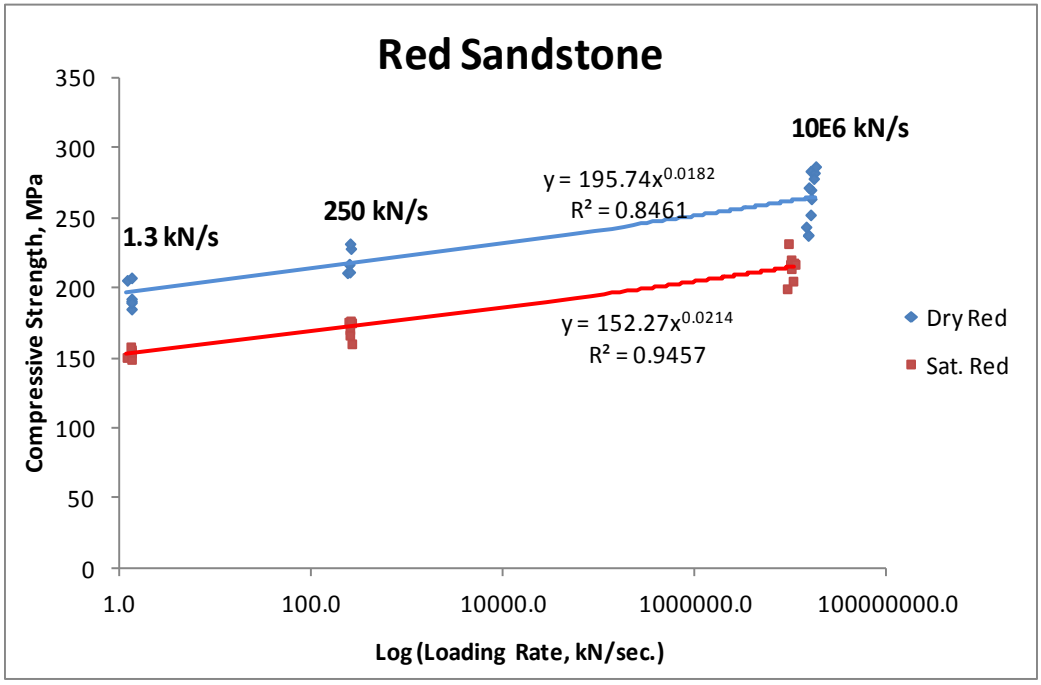

Figure 4.37 Loading rate effect on dry and saturated red sandstone.

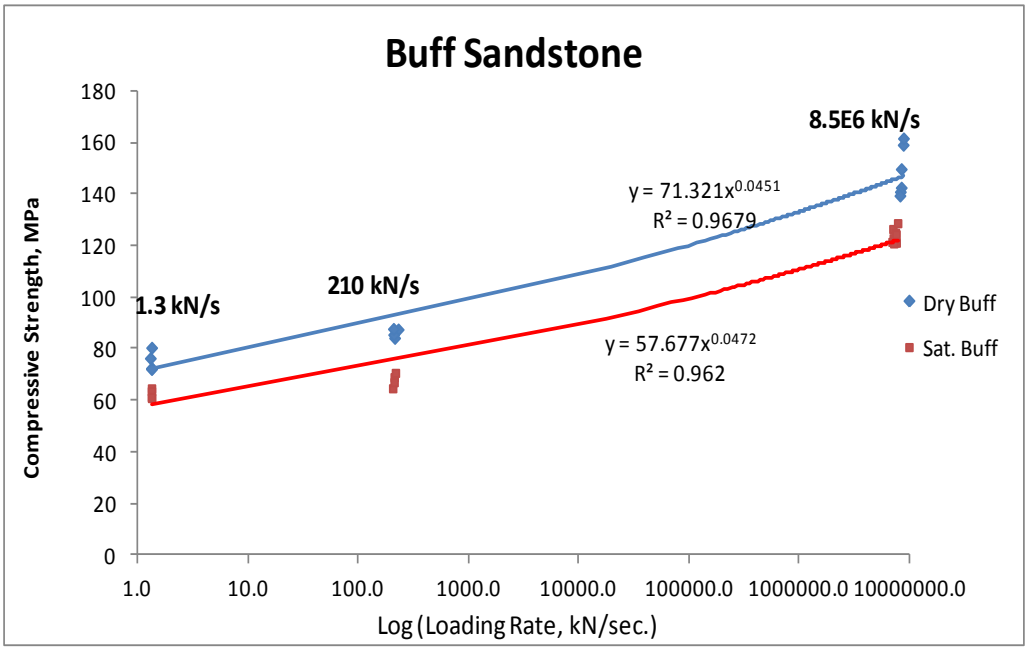

Figure 4.38 Loading rate effect on dry and saturated buff sandstone.

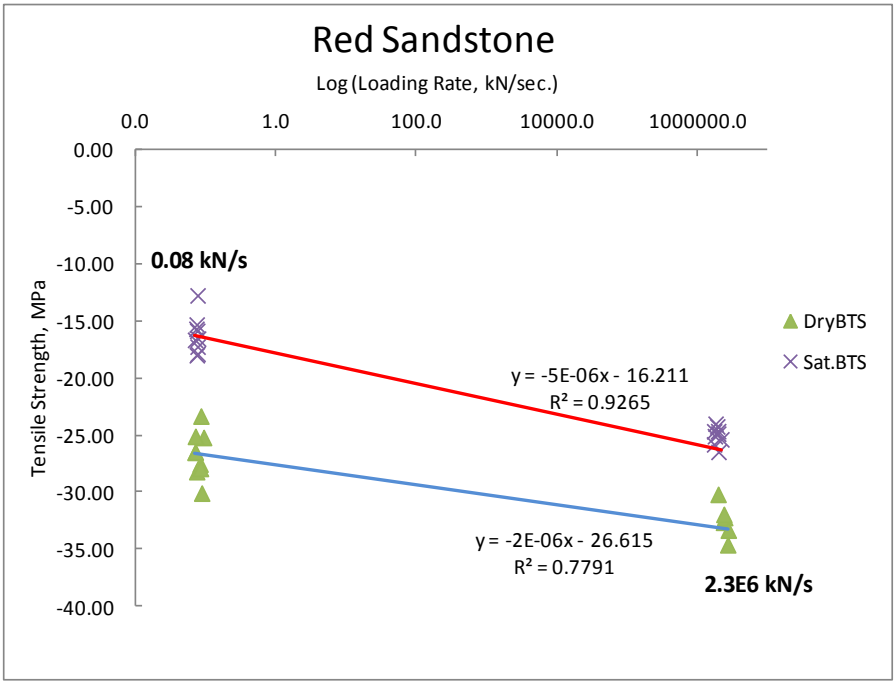

Figure 4.39 Loading rate effect on tensile strength of dry and saturated red sandstone.

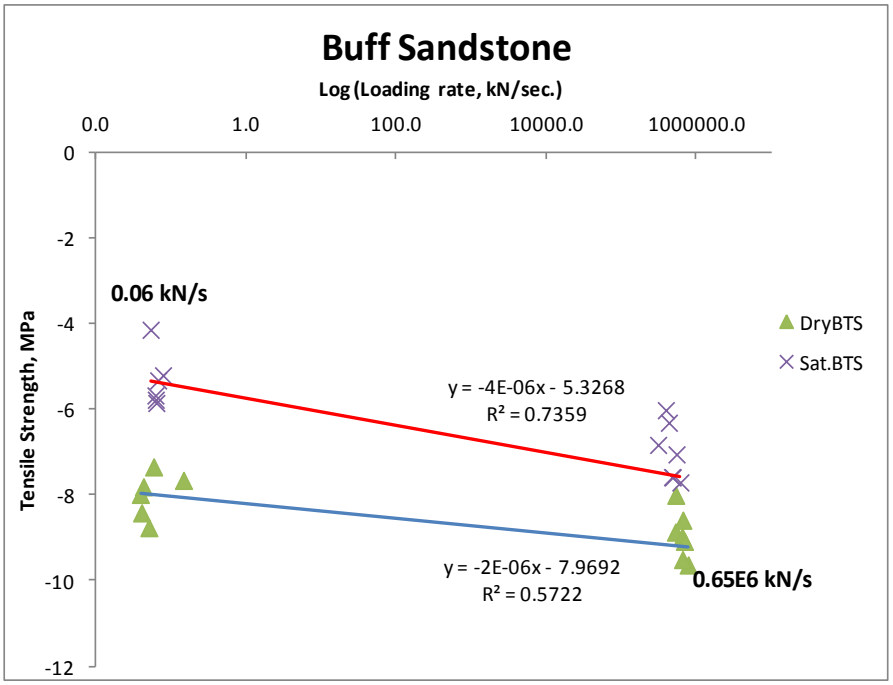

Figure 4.40 Loading rate effect on tensile strength of dry and saturated buff sandstone.

Figure 4.41 Fragment samples of buff sandstone (left: Saturate; right: Dry sample).

Figure 4.42 Fragment of samples of red sandstone (left: Saturated; right: Dry sample).

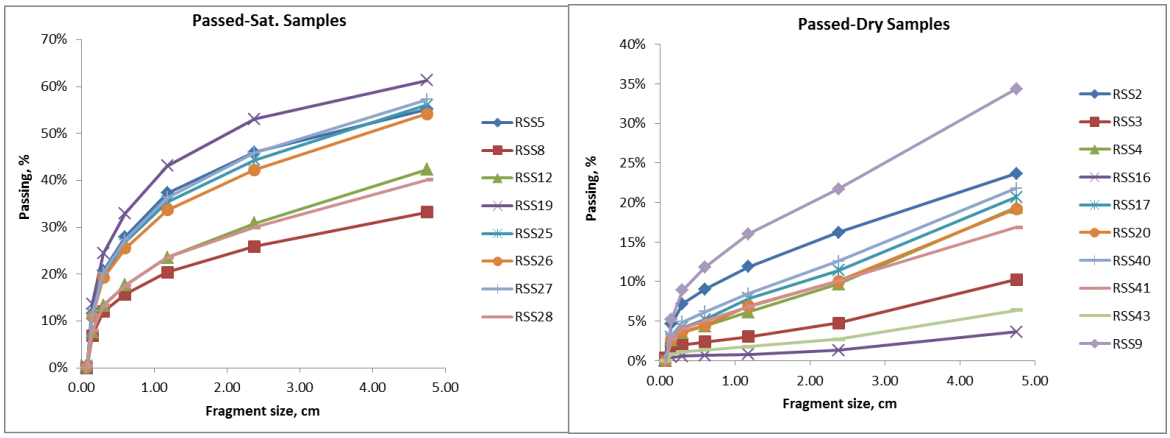

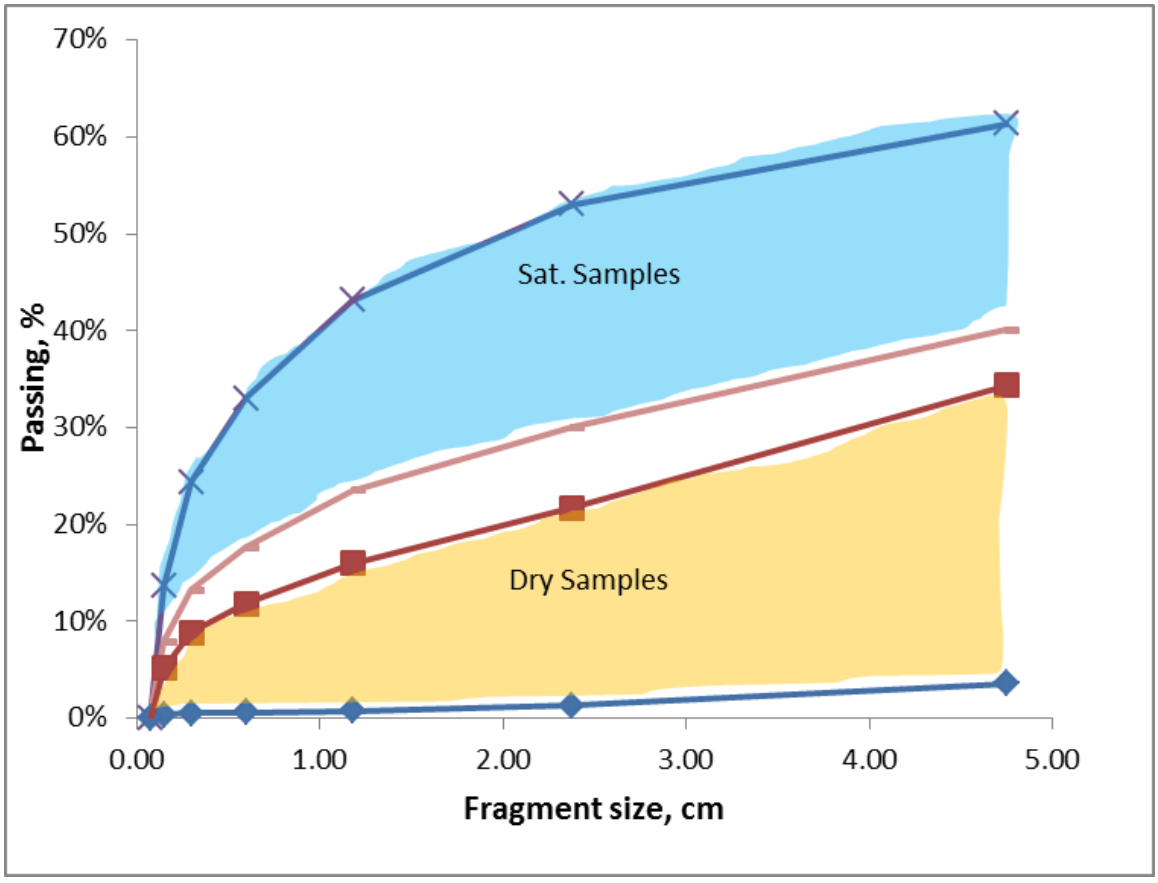

Figure 4.43 Rock fragment size distribution for dry and saturated red sandstone.

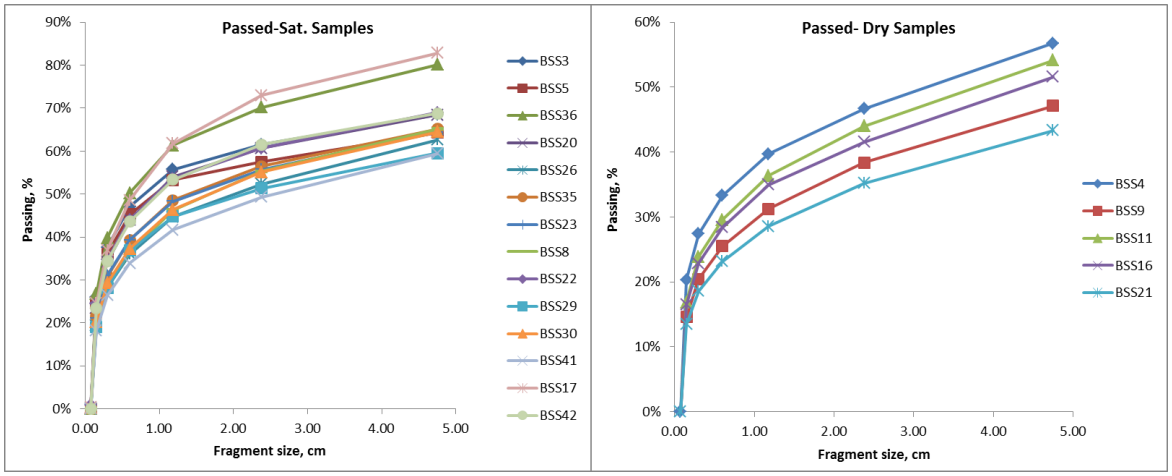

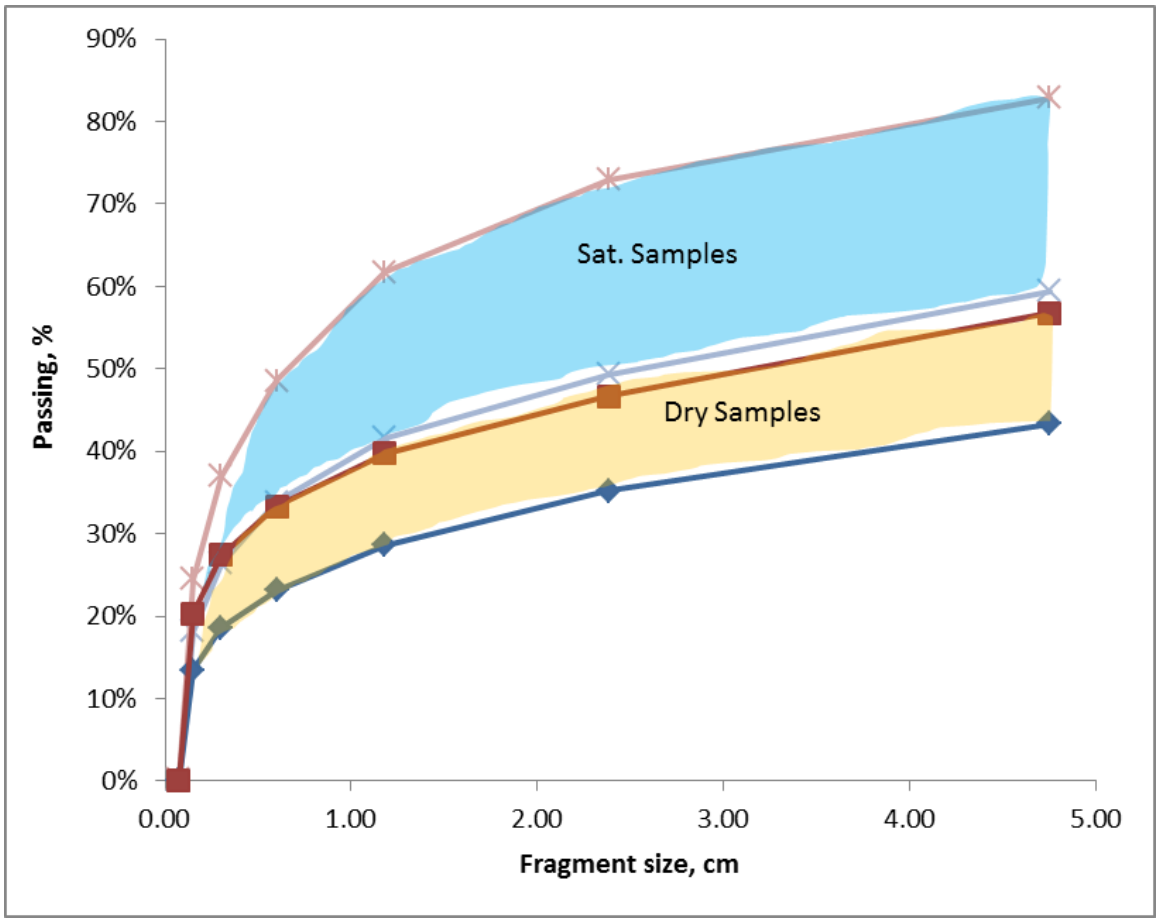

Figure 4.44 Rock fragment size distribution for dry and saturated buff sandstone.

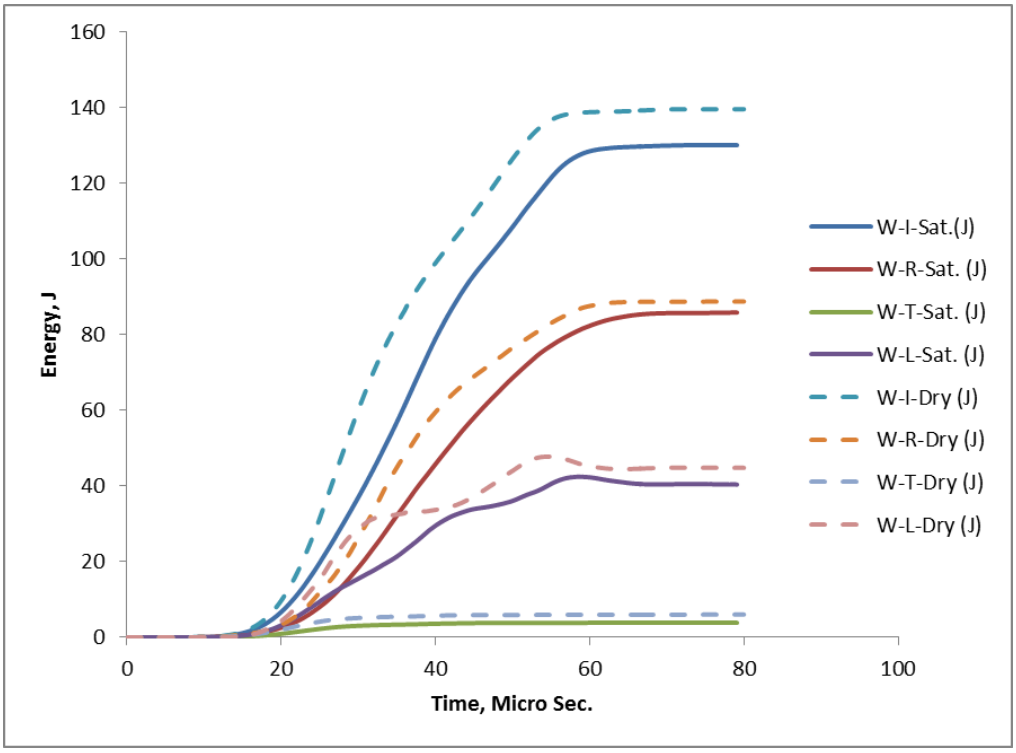

Figure 4.45 Difference between energy absorption components in dry and saturated conditions.

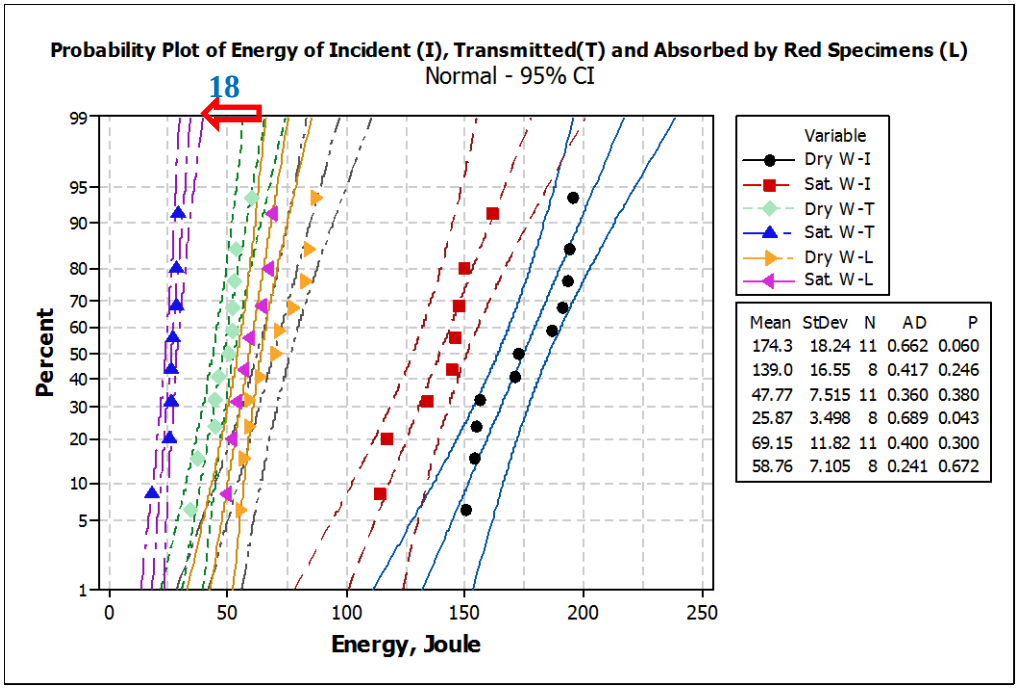

Figure 4.46 Energy absorption difference in dry and saturated red sandstone.

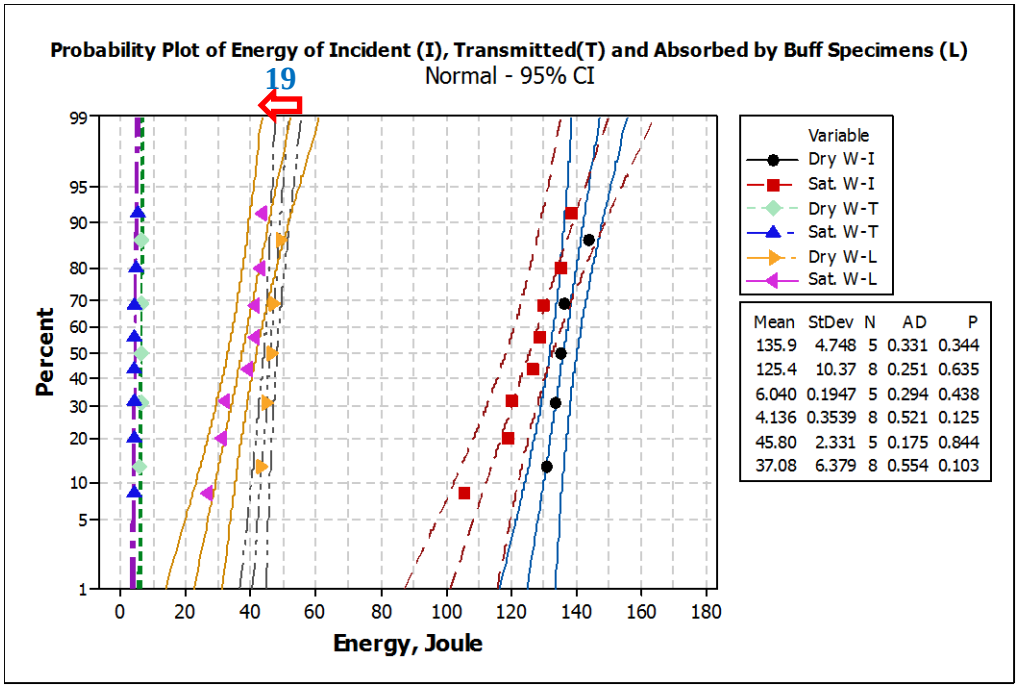

Figure 4.47 Energy absorption difference in dry and saturated buff sandstone.

CHAPTER 5

CONCLUSION

Various parameters characterize rock fracture and strength, and the measured rock strength differs depending on how the stress is applied. The compressive and tensile strength of red and buff sandstones under the static and dynamic conditions were two properties measured in this research. In addition, the porosity and moisture content effects on these parameters were investigated.

In this study, the rock samples that were selected were fairly homogeneous. All of the buff sandstone samples had a porosity near 22.5%, and the red sandstone samples had a porosity near 5.5%. Experiments on these two different sandstones showed that the buff sandstone had a lower compressive strength under both static and dynamic conditions than the red sandstone at each loading rate. The porosity of red sandstone is about one-fourth that of buff sandstone. However, the compressive strength of red sandstone is only about 2.5 times higher than the buff sandstone. Therefore, the contrast in strength is not directly related to the ratio of porosity for static and fast loading and in fully saturated and oven-dried conditions, as can be seen in Figures 5.1 and 5.2. Dynamic results show that a fourfold porosity increase reduced the compressive strength under high strain rate loading by about 1.8 times in both dry and saturated conditions.

Water content reduced the cohesion in red and buff sandstones by about 25% and

20%, respectively. The strength of dry samples in all of the static, fast loading, and dynamic tests was higher than the strength in saturated conditions; on average, saturation with water reduced the rock strength about 20% (Figures 5.3 and 5.4).

The ultrasonic velocity test method offers a nondestructive way to characterize geological core samples. These tests involve propagating ultrasonic compression and shear waves along the longitudinal axis of the sample, and then measuring the velocity of the waves as they travel through the specimen to calculate dynamic elastic properties. These properties include Young's modulus, bulk modulus, and Poisson's ratio (ASTM 2845). In this study, P and S wave velocity measurements were used to calculate the dynamic Young's modulus of oven-dried specimens. In addition, the dynamic Young's modulus was measured based on the experimental results of the SHPB on the same samples. As illustrated in Figures 5.5 and 5.6 the dynamic Young's modulus calculated from the SHPB results is 10-20 times higher than that calculated from the ultrasonic velocity test. Enhancement of strength for different engineering materials such as rock, ceramic and concrete has been investigated at high strain rates in different research projects, and there is no unique correlation between dynamic strength and strain rate. In the present study the effect of strain rate on the strength of two types of sandstone (Figure 5.7) was investigated, and based on the results given in Chapter 4, the dynamic increase factors (DIF) of red sandstone at a strain rate about of 300 s^{-1} are 1.36 and 1.41 for dry and saturated specimens, respectively. For buff sandstone, an average DIF of 2.0 was observed at a strain rate about of 350s^{-1} for both dry and fully saturated conditions.

Energy absorption in saturated rock specimens is about 15% and 19% lower than that in dry samples for red and buff sandstones, respectively. Nevertheless, the

percentages of fragments smaller than 2 cm in saturated rock specimens are twice as great as in dry samples. Based on these results, it can be concluded that to get the same fragment size distribution under saturated conditions, less energy is needed. In addition, buff sandstone, which is four times more porous, absorbed 30% less energy and produced finer particle size distributions than the red sandstone.

In oil and gas wells, fine materials created after the perforation process can move into the porous channels during hydrofracturing and reduce the reservoir rock permeability. In this research, the fine material in saturated rock specimens was higher than in dried samples. Based on these results, the saturation condition of reservoir rock should be taken into account when designing the blasting charge of the perforating gun to reduce fine material during perforation.

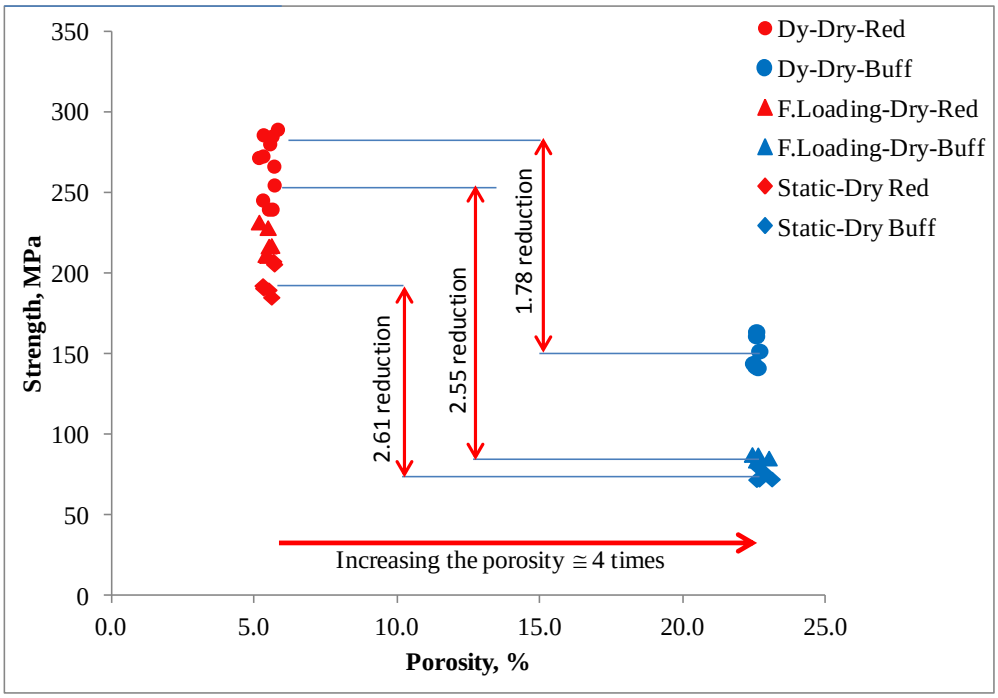

Figure 5.1 Porosity effects on rock compressive strength in dry conditions.

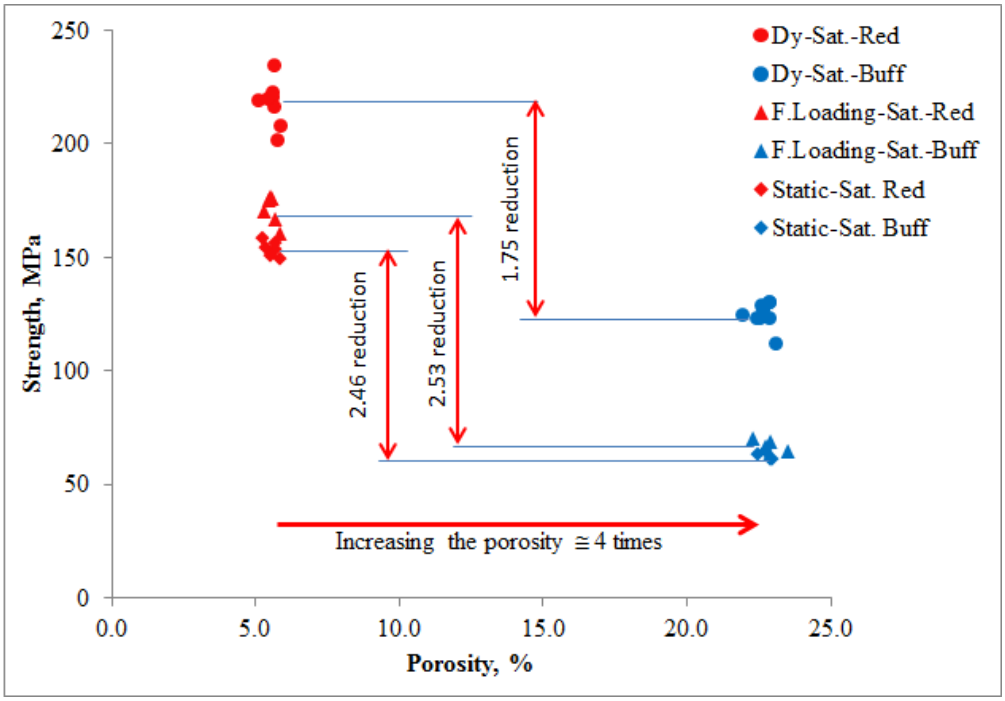

Figure 5.2 Porosity effects on rock compressive strength in saturated conditions.

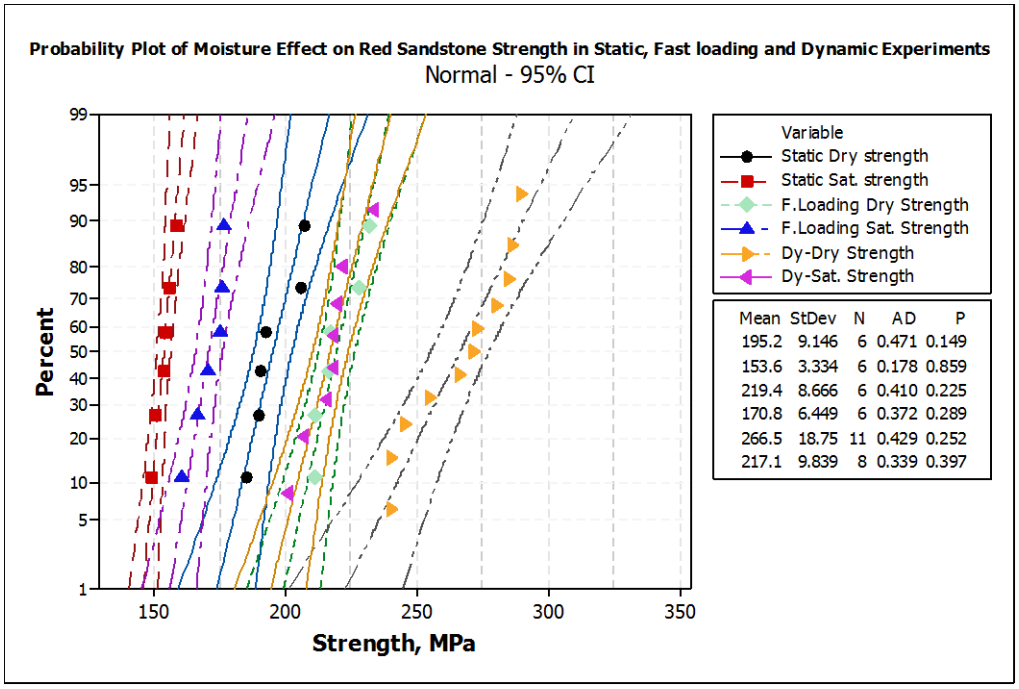

Figure 5.3 Water content effects on red sandstone compressive strength.

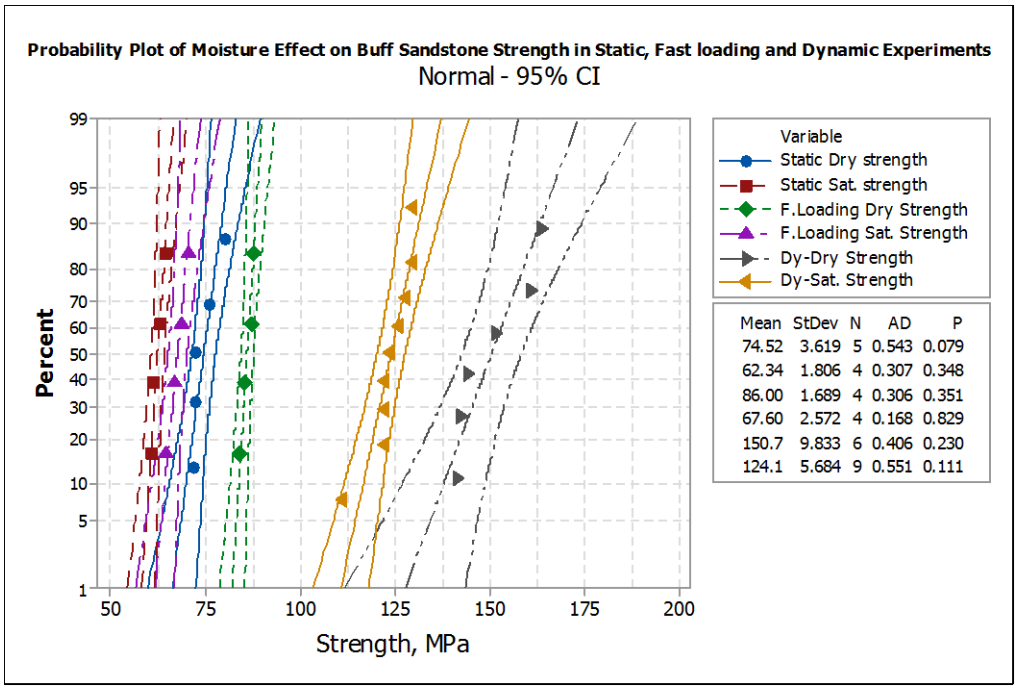

Figure 5.4 Water content effects on buff sandstone compressive strength.

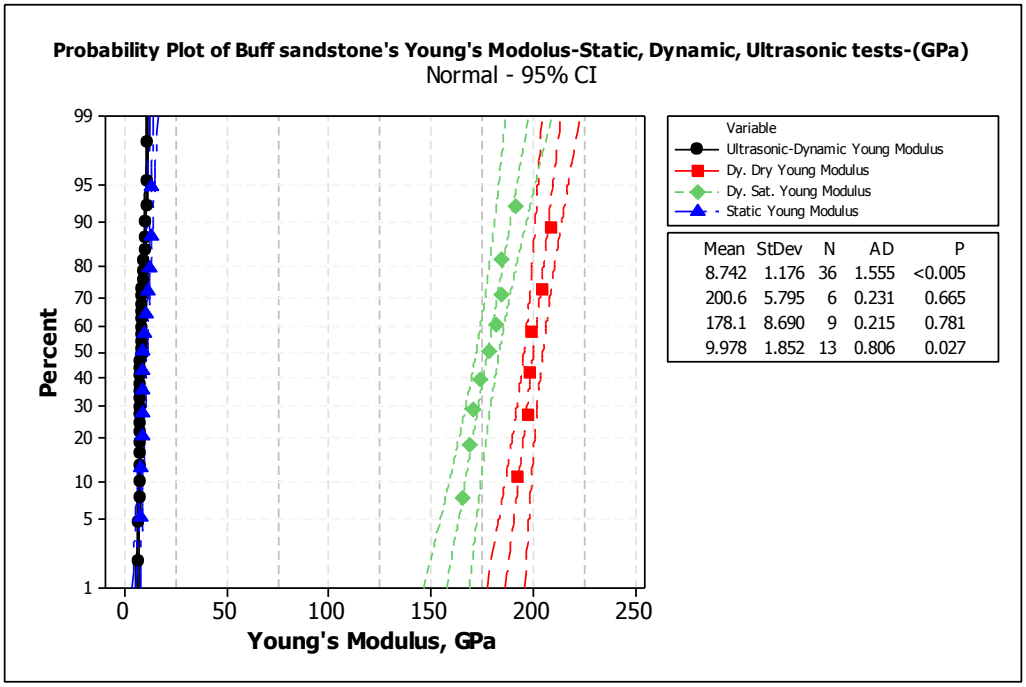

Figure 5.5 Differences between dynamic Young's modulus measured by ultrasonic wave velocity and SHPB results of buff sandstone.

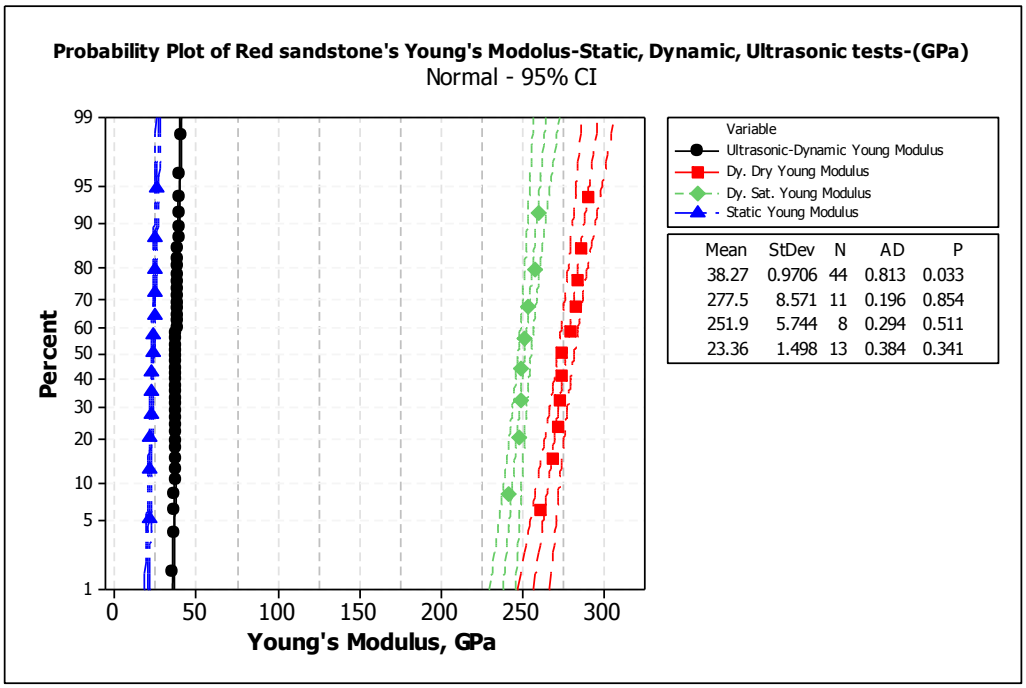

Figure 5.6 Differences between dynamic Young's modulus measured by ultrasonic wave velocity and SHPB results of red sandstone.

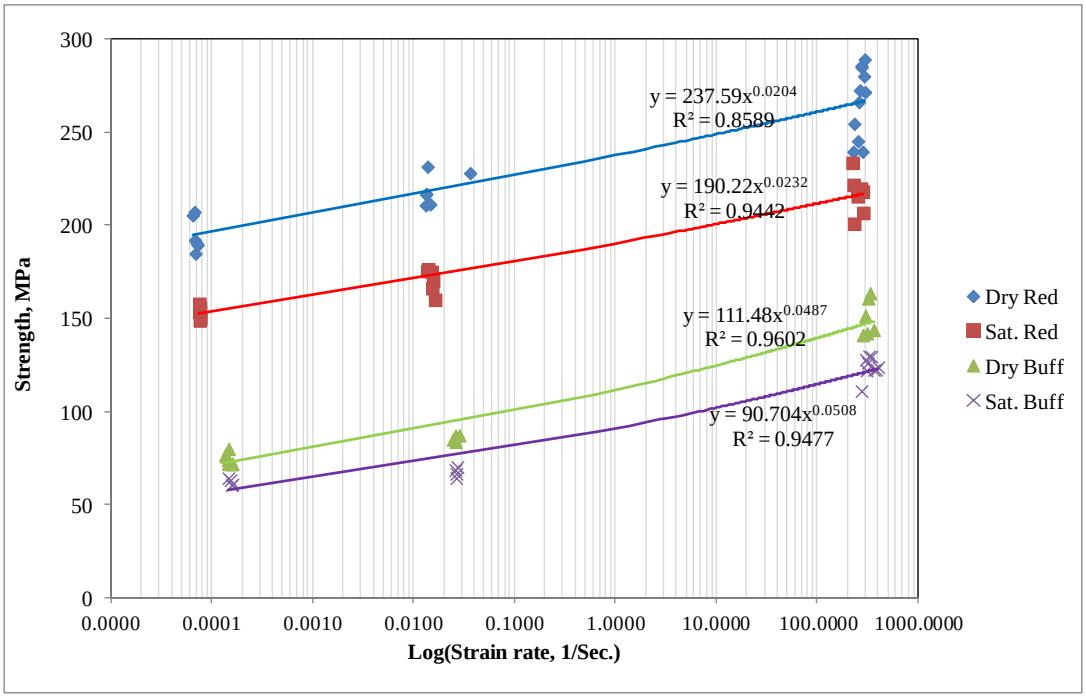

Figure 5.7 Strain rate effects on strength of dry and saturated red and buff sandstone.

CHAPTER 6

FUTURE WORK

This research showed interesting results on the effects of porosity and water content on static and dynamic strengths of red and buff sandstones with porosity contents of about 5.5 and 22.5%. Therefore, to get a more acceptable trend in porosity and water content effects on dynamic behavior sandstone in general, it is recommended that samples with other porosities be tested.

The maximum strain rate achieved in the present study was about 350 s^{-1}, and its effects on rock strength was investigated. The strain rate range encountered in a blasting and perforating gun operation is about 1000–2000/s, so the effects of higher strain rates should be investigated for practical applications. Such additional experiments would help better define trends in the strain rate effects on the dynamic compressive and tensile strength of these and similar rocks.

Compressive Split Hopkinson Pressure Bar (SHPB) tests should also include studies related to the effects of confining pressure on the dynamic strength of rock, because in all real cases such as blasting and perforating in oil and gas wells, the rock has substantial confining pressure. Confinement will affect the dynamic behavior of rocks.

An appropriate method of establishing UCS for deformable rock should be explored. At present, sample destruction is often required to establish failure under

unconfined conditions. For highly deformable materials, this criterion may not be appropriate when automated failure detection is established by testing machine protocol.

APPENDIX

A.1 Red Sandstone

The median grain size ~0.15 mm, by visual estimate. On the Wentworth scale, this rock would be classified as a fine grained sandstone. Visual estimate gives the following mineral contents expressed as a percentage:

- Quartz 67%
- Quartz overgrowths (cement) 4%
- Feldspar 12%
- Rock fragments (mostly phyllite) 9%
- Tourmaline (zircon also present) 1%
- Hematite (cement) 5%
- Kaolinite (cement) 2%

Parts of some quartz grains are rounded, parts are angular (broken); thus these grains are probably recycled from a rounded sedimentary source.

Neoform clay is mostly illite (recrystallized from a silicate precursor).

Opaque minerals include hematite as a cement, magnetite, leucoxene (rare), and possibly ilmenite.

Diagenesis (cements) sequence:

1. Hematite rims on quartz grain nuclei

2. Quartz overgrowths
3. Hematite pore filling (local)
4. Kaolinite (some enclosed in hematite rims.

A.2 Buff Sandstone

The median grain size is 0.08-0.09 mm. On the Wentworth scale this rock would be classified as a very fine grained sandstone. Visual estimate gives the following mineral contents expressed as a percentage:

- Quartz 33%
- Quartz overgrowths (rare) 1%
- Feldspar (K-spar> plagioclase) 24%
- Feldspar overgrowths 1%
- Rock Fragments (sedimentary) 27%
- Rock Fragments (metamorphic) 4%
- Zircon 1%
- Tourmaline 2%
- Hematite cement 6%
- Carbonate cement (both as
- Replacement and pore fill) 1%
- Muscovite Trace
- Biotite Trace
- Chlorite Trace
- Kaolinite Trace

This rock is cross-bedded with low angle climbing ripples. The sedimentary rock fragments are of shale and carbonate, with shale comprising most of them. The carbonate fragments are encased in hematite crusts (hence the survival of the carbonate). Some of the feldspar grains are fresh; others are altered (with patches of sericite). Some of the plagioclase is zoned.

Sheet silicates are present, but each makes up <1% of the rock. They include muscovite, biotite, and chlorite, and kaolinite is rare but occurs in a few pores.

There is considerable evidence for compaction. Some grains are bent and broken, some of the rock fragments have been flattened.

Feldspar overgrowths and rare pore fillings are diagenetic, as is the carbonate replacement and cement. There are some quartz overgrowths, but overgrowths on the feldspar are more common. The sequence of diagnetic events is not obvious.

Descriptions are by Dr. John Comer, made on 17 April, 2015.

REFERENCES

Albertini, C., Cadoni, E., and Labibes, K. 1996. Dynamic mechanical behavior of large concrete specimens by means of Hopkinson bar Bundle. *Proc. 2nd Int. Symp.Impact Eng.* –Chin. J. Mech. 214–219.

ASTM C136/C136M-14. 2014. *Standard Test Method for Sieve Analysis and Coarse Aggregates.* Philadelphia, PA: ASTM International

ASTM D2845. 2013. *Standard Test Method for Laboratory Determination of Pulse Velocities and Ultrasonic Elastic Constants of Rock.* Philadelphia, PA: ASTM International.

ASTM D3967. 2013. *Standard Test Method for Splitting Tensile Strength of Intact Rock Core Specimens.* Philadelphia, PA: ASTM International.

ASTM D7012. 2013. *Standard Test Method for Compressive Strength and Elastic Moduli of Intact Rock Core Specimens under Varying States of Stress and Temperatures.* Philadelphia, PA: ASTM International.

ASTM E9-09. 2013. *Standard Test Methods of Compression Testing of Metallic Materials at Room Temperature*. Philadelphia, PA: ASTM International.

Atchison, T.C., and Pugliese, J.M. 1964. *Comparative studies of explosives in limestone. Report of Investigation RI-6395.* Washington, DC: U.S. Bureau of Mines.

Bancroft, D. 1941. The velocity of longitudinal waves in cylindrical bars. *Phys. Rev.*, 59(59): 588–593.

Bieniawski, Z.T., Hawkes I. 1987. Suggested method for determining the tensile strength of rock materials. *Int. J. Rock Mech. Min. Sci*. 15: 99–103.

Bulson, P.S 2002. *Explosive Loading of Engineering Structures*. London: E & FN Spon.

Cai, M., Kaiser, P.K., Suorineni, F., and Su, K. 2007. A study on dynamic behavior of the Meuse/Haute-Marne argillite. *Phys. Chem. Earth.* 32: 907–916.

Davies, E.D.H., and Hunter, S.C. 1962. The dynamic compression testing of solids by the method of the split Hopkinson pressure bar. *J. Mech. Phys. Solids*. 11(3): 155–179.

Davies, R. M. 1948, A critical study of the Hopkinson pressure bar. *Philos. Trans. R. Soc. London, Ser. A.* 240: 375–457.

Dong, Y.X., Xia, C.J., Xiao, L.X., and Feng, S.S. 2011. Dynamic mechanical properties of porous rock under impact loading. In *Machinery, Materials Science and Engineering Applications*. Edited by Q. Gao. Beijing, China: Trans Tech Publications. pp. 5–9.

Duffy J., Campbell, J.D., and Hawley, R.H. 1971. On the use of a torsional Split Hopkinson Bar to study rate effects in 1100–0 aluminum. *J. Appl. Mech*. 38: 83–91.

Field, J.E., Walley, S.M., Proud, W.G., Goldrein, H.T., and Siviour, C.R. 2004. Review of experimental techniques for high rate deformation and shock studies. *Int. J. Impact Eng.* 30: 725–775.

Goldsmith, W. 1966. Pulse propagation in rocks. In *Failure and Breakage of Rock, Proceedings of the 8th Symposium on Rock Mechanics*, University of Minnesota, September 15-17. Littleton, CO: American Institute of Mining, Metallurgy & Petroleum Engineers. pp. 528–537.

Goldsmith, W., Sackman, J.L., and Ewert, C. 1976. Static and dynamic fracture strength of Barre granite. *Int. J. Rock Mech. Min. Sci.* 13: 303–309.

Gomez, J.T., Shukla, A., and Sharma, A. 2001. Static and dynamic behavior of damaged concrete and granite in compression. *J. Test. Eval.* 29(6): 563–569.

Gorham, D.A., Pope, P.H., and Cox, O. 1984. Source of error in very high strain rate compression tests. *Mechanical properties at high rates of strain, 1984: Proceedings of the Third Conference on the Mechanical Properties of Materials at High Rates of Strain held in Oxford, 9-12 April 1984.* Edited by J. Harding. Bristol: Institute of Physics. pp. 151–158.

Gray, G.T., III. 2000. Classical split Hopkinson Pressure Bar testing. In *ASM Handbook. Vol. 8, Mechanical Testing and Evaluation.* Edited by H. Kuhn and D. Medlin. Materials Park, OH: ASM International. pp. 462–476.

Harding, J., Wood, E.O., and Campbell, J.D. 1960. Tensile testing of materials at impact rates of strain. *J. Mech. Eng. Sci.* 2: 88–96.

Hauser, F.E., Simmons, J.A., and Dorn, J.E. 1960. Strain rate effects in plastic wave propagation. *Proc. Metall. Soc. Conf.* 9: 93–114.

Hauser, F.E., Simmons, J.A., and Dorn, J.E. 1961. Strain rate effects in plastic wave propagation. In *Response of Metals to High Velocity Deformation.* Edited by P.G. Shewmon and V.F. Zackay. New York: Interscience Publishers. pp. 93–114.

Hopkinson, B. 1914. A method of measuring the pressure produced in the detonation of high explosives or by the impact of bullets. *Philos. Trans. R. Soc. London, Ser. A.* 213: 437–456.

Igbal, N., Xue, P., Wang, B., and Li, Y.L. 2011. Material characterization of porous bronze at high strain rate. *Materials Science and Engineering: A.* 528 (13-14): 4408–4412.

Johnson, J.C. 2010. The Hustrulid Bar—A dynamic strength test and its application to cautious blasting of rock. Ph.D dissertation, University of Utah, UT.

Kim, D.S. 1993. The effect of shock-induce damage on comminution of rock materials. Ph.D dissertation, University of Utah, UT.

Kim, D.S., and McCarter, M.K. 1998. Quantitative assessment of extrinsic damage in rock material. *Rock Mech. Rock Eng*. 31(1): 43–62.

Kolsky, H. 1949. An investigation of the mechanical properties of materials at very high rates of strain. *Proc. Phys. Soc. London, Sect. B.* 62: 676–700.

Lu, H., Huang, B., Zhao, H., Meng, M., and Liang, M. 2013. Dynamic responses of red sandstone with fluid-solid coupling under impact loading. *Adv. Mater. Res*. 724–725: 1500–1505.

Lundberg, B. 1976. A Split Hopkinson Bar study of energy absorption in dynamic rock fragmentation. *Int. J. Rock Mech. Min. Sci.* 13: 187–197.

Maiden, C.J., and Green, S.J. 1966. Compressive strain rate tests on six selected materials at strain rates from 10^{-3} to 10^{4} in/in/sec. *J. Appl. Mech.* 33(3): 496–504.

McCarter, M. 1972. A correlation of strength and dynamic properties of some clastic sedimentary rocks. PhD dissertation, University of Utah, UT.

Meyers, M.A., 1994, *Dynamic Behavior of Materials.* New York: John Wiley and Sons.

Mohanty, B., and Prasad, U. 2001. Degree of rock fragmentation under high strain rates. In *Proceedings of the 27th Annual Conference on Explosive and Blasting Technique,* Orlando, FL, January 28-31. Cleveland, OH: International Society of Explosive Engineers. pp. 89–96.

Parker, J. 1969. Temperature and humidity affect strength of rock structure at White Pine. Paper presented at *Society of Mining Engineering, AIME Fall Meeting,* Salt Lake

City, Utah.

Prasad, U. 2000. Dynamic fracture characteristic of selected rocks. PhD dissertation, University of McGill, CA.

Rinehart, J.S. 1965. Dynamic fracture strength of rocks. *VII Symp. Rock Mech*. 1: 205–208.

Ulusay, R., and Hudson, J.A., eds. 2007. *The complete ISRM suggested methods for rock characterisation, testing and monitoring: 1974–2006*. Ankara, TR: International Society for Rock Mechanics, Commission on Testing Methods.

Zhao, J., Zhou, Y.X., Hefny, A.M., Cai, J.G., Chen, S.G., Li, H.B., Liu, J.F., Jain, M., Foo, S.T., and Seah, C.C. 1999. Rock dynamic research related to cavern development for ammunition storage. *Tunnelling Underground Space Technol.* 4(4): 515–526.

Zhou, Y., and Zhao, J. 2011. *Advances in Rock Dynamics and Applications*. London: Taylor & Francis Group.